Thermal Science and Engineering

EnPress

https://systems.enpress-publisher.com/index.php/TSE

2024 Volume 7 Issue 1
ISSN: 2578-1782 (Online)

Editorial Board

Editor-in-Chief

Associate Editors

Editorial Board Members

Volume 7 Issue 1 • 2024

Thermal Science and Engineering

EnPress Publisher

EnPress Publisher

2024 | Volume 7 | Issue 1

Thermal Science and Engineering

https://systems.enpress-publisher.com/index.php/TSE

Contents

Articles

Review

Thermal Science and Engineering 2024, 7(1), 6036.
https://doi.org/10.24294/tse.v7i1.6036

Article

Thermal radiation and MHD effect on the double-diffusive convective flow of second-grade fluid over a stretching sheet

K. G. Chandan, B. Patil Mallikarjun*

Department of Studies and Research in Mathematics, Tumkur University, Tumakuru 572103, India
*** Corresponding author:** B. Patil Mallikarjun, mbp1007@yahoo.com

CITATION

Chandan KG, Mallikarjun BP. Thermal radiation and MHD effect on the double-diffusive convective flow of second-grade fluid over a stretching sheet. Thermal Science and Engineering. 2024; 7(1): 6036. https://doi.org/10.24294/tse.v7i1.6036

ARTICLE INFO

Received: 17 December 2023
Accepted: 9 January 2024
Available online: 18 January 2024

Abstract: An investigation is conducted into how radiation affects the non-Newtonian second-grade fluid in double-diffusive convection over a stretching sheet. When fluid is flowing through a porous material, the Lorentz force and viscous dissipation are also taken into account. The flow equations are coupled partial differential equations that can be solved by MATLAB's built-in bvp4c algorithm after being transformed into ODEs using appropriate similarity transformations. Utilizing graphs and tables, the impact of a flow parameter on a fluid is displayed. On velocity, temperature, and concentration profiles, the effects of the magnetic field, Eckert number, and Schmidt number have been visually represented. Calculate their inaccuracy by comparing the Nusselt number and Sherwood number values to those from earlier investigations.

Keywords: magnetic field; double diffusion; porous medium; second-grade fluid; stretching sheet

1. Introduction

The models of Misra et al. [1] and Jacobson and Hamrock [2] are among those that have been developed to examine the behavior of non-Newtonian fluids. Due to its use in engineering and industrial purposes, fluid flow problems over a stretching/shrinking surface are attracting the interest of many researchers. Crane [3] later developed this work for flow past a stretching sheet after Sakiadis [4,5] had first studied the problem of a stretching sheet. Many famous scholars have been solving the majority of stretching sheet problems analytically for decades. In the papers of Hamad [6], Wang [7], Khan et al. [8], Hayat et al. [9], flow problems are solved analytically by taking into account the magnetic field in natural convection of nanofluid, surface slip and suction due to stretching sheet, three-dimensional flow over a non-linearly stretching sheet, and magnetohydrodynamics (MHD) in Oldroyd-B nanofluid, respectively. Stretching sheet problems can also be solved numerically using a variety of methods; current research has compared these numerical approaches to their analytical counterparts. When comparing the prominent Chebyshev pseudospectral and finite difference methods, Tzirtzilakis and Tanoudis [10] take into account the movement of biomagnetic fluid flow over a stretching sheet. In their contribution, Datti et al. [11] compare the analytical solution with the fourth-order Runge-Kutta method while accounting for MHD and heat radiation across a non-isothermal stretched sheet.

In recognition of its applications in oceanography [12], geology, and astrophysics, double-diffusive convection has recently attracted the attention of many academics. Turner [13,14] first used the term "double diffusion" to describe

the phenomenon of diffusion caused by two distinct density gradients in a fluid. Many non-Newtonian fluids, including Williamson and Casson fluids, are subject to double-diffusive convection; in this case, we are applying this convection phenomenon to a non-Newtonian second-grade fluid that has nonlinear properties. Second-grade fluid flowing through a porous channel in the presence of a uniform magnetic field that is applied in the transverse direction of flow is solved using the homotopy analysis method by Hayat et al. [15]. Vajravelu and Rollins [16] utilized a uniform magnetic field over a stretching sheet to solve the momentum problem analytically and quantitatively. Bafakeeh et al. [17] explored the unsteady condition of second-grade fluid by taking into account thermal radiation and chemical reactions along with analyzing the physical quantities. The papers of Massoudi and Vaidya [18], Gowda et al. [19], Awan et al. [20], and Khan et al. [21] list several works on second-grade fluid.

One of the three main mechanisms of heat transfer is thermal radiation; the other two mechanisms are convection and radiation. Due to the thermal motion of particles in fluid, electromagnetic radiation is generated, which is recurrently known as thermal radiation. The essence of different Newtonian/non-Newtonian fluids can be studied by applying the effect of thermal radiation. The effect of thermal radiation along with a magnetic field due to the double-diffusive peristaltic flow of a nanofluid in a porous medium was extensively studied by Kotnurkar and Giddaiah [22], Asha and Sunitha [23], and Asha and Sunitha [24]. In the study of Akbar et al. [25], entropy is taken into account by considering radiation and inclined MHD effects for two different fluids, such as Newtonian and Williamson fluids, as interpreted by Dadheech et al.

The primary development of our study is to apply thermal radiation to the double-diffusive convection of second-grade fluid flowing through a porous medium. The study of second-grade fluid flowing over a stretching sheet was recently published in papers by Dey and Borah [26], Ghadikolaei et al. [27], and Endalew and Sarkar [28]. The governing equations of flow are partial differential equations that can be transformed into ordinary differential equations using suitable similarity transformations and solved numerically using the MATLAB bvp4c technique. Results have been shown through graphs and compared with the values in tables with previous studies of second-grade fluid, and error will be calculated for the Nusselt number.

2. Formulation of the problem

The laminar flow of fluid is imprisoned in the region $x > 0$ and $y > 0$ when the incompressible flow of a nonlinear second-grade fluid via a stretched surface is taken into account. Because of the double-diffusion, the lower end is either heated or cooled, and two separate density gradients result from the additional substance. Temperature and concentration are symbolized by T and C, respectively, while wall temperature and concentration are represented by T_w and C_w. When heated, the fluid has a temperature of $T_w > T_\infty$ (ambient state), and when cooled, it has a temperature of $T_w < T_\infty$. The sheet behaves as an elastic surface with a velocity of $u_w(x) = cx$, and a uniform magnetic field B_0 applied perpendicular to the direction of fluid flow.

Constant $c > 0$ signifies surface stretch.

If T is the Cauchy stress tensor, then the equations constituting for non-Newtonian second-grade fluid model is given by [28]:

$$T = -pI + \sum_{j=1}^{2} S_j \tag{1}$$

where I is the identity tensor, p is the pressure and S_j is the extra stress tensor, such that

$$S_1 = \mu_u A_1, \tag{2}$$

$$S_2 = \alpha_1 A_2 + \alpha_2 A_1^2, \tag{3}$$

where α_j ($j = 1,2$) and μ_u are material constants and coefficient of viscosity respectively. $A_j (j = 1,2)$ are Rivlin-Ericksen tensors defined by

$$A_1 = (gradq) + (gradq)^t, \tag{4}$$

$$A_2 = \frac{d}{dt} A_1 + A_1 gradq + (gradq)^t A_1, \tag{5}$$

where the superscript t is the transpose of a matrix, q is the velocity field in two-dimensional flow which can be expressed as

$$q = (u(x, y, t), v(x, y, t), 0) \tag{6}$$

By examining the boundary layer, the steady state of a two-dimensional governing equations of fluid flow are [27]:

$$\frac{\partial u}{\partial x} + \frac{\partial v}{\partial y} = 0, \tag{7}$$

$$\begin{aligned} u\frac{\partial u}{\partial x} + v\frac{\partial u}{\partial y} = \nu\frac{\partial^2 u}{\partial y^2} + \frac{\alpha_1}{\rho}\left[\frac{\partial}{\partial x}\left(u\frac{\partial^2 u}{\partial y^2}\right) + v\frac{\partial^3 u}{\partial y^3} + \frac{\partial u}{\partial y}\frac{\partial^2 v}{\partial y^2}\right] \\ + [g\beta_T(T - T_\infty) + g\beta_C(C - C_\infty)] - \frac{\sigma B_0^2}{\rho}u - \frac{\nu}{K'}u \end{aligned} \tag{8}$$

$$u\frac{\partial T}{\partial x} + v\frac{\partial T}{\partial y} = \alpha\frac{\partial^2 T}{\partial y^2} + \frac{K}{\rho C_p}\left(\frac{\partial u}{\partial y}\right)^2 - \frac{1}{\rho C_p}\frac{\partial q_r}{\partial y} + \frac{\nu}{K'}u^2, \tag{9}$$

$$u\frac{\partial C}{\partial x} + v\frac{\partial C}{\partial y} = D\frac{\partial^2 C}{\partial y^2}, \tag{10}$$

with the associated boundary conditions:

$$\begin{aligned} v = 0, u = u_w = cx, T = T_w (= T_\infty + A_1 x^s), C = C_w (= C_\infty + B_1 x), \text{at } y = 0, \\ u \to 0, \frac{\partial u}{\partial y} \to 0, T \to T_\infty, C \to C_\infty, \text{as } y \to \infty. \end{aligned} \tag{11}$$

where u and v, respectively, account to the velocity components along the x and y directions. β_T, β_C, C_p, K, ν, ρ, g, σ, K', α and D represents the coefficient of thermal expansion, solutal expansion, the specific heat of a fluid at a steady pressure, thermal conductivity, kinematic viscosity, density of the fluid, acceleration due to gravity, electrical conductivity, permeability of porous medium, thermal diffusivity, and mass diffusivity respectively.

The following similarity transformations are utilized for transforming Equations (7)–(10) into an array of ordinary differential equations.

$$\psi(x, y) = \sqrt{c\nu}xF(\eta), \eta = \sqrt{\frac{c}{\nu}}y, \Theta(\eta) = \frac{T - T_\infty}{T_w - T_\infty}, \zeta(\eta) = \frac{C - C_\infty}{C_w - C_\infty} \tag{12}$$

The momentum, energy, and concentration equations are transformed into the

subsequent system of ODEs using the transformations described above:

$$F''' - (F')^2 + FF'' + k\left[2F'F''' - (F'')^2 - FF^{iv}\right] - MF' - \epsilon F' + \lambda[\Theta + N\zeta] = 0, \tag{13}$$

$$\Theta''\left(1 + \frac{4}{3}R\right) + Pr(F\Theta' - 2F'\Theta) + PrEc(F'')^2 + \epsilon F'^2 = 0, \tag{14}$$

$$\zeta'' + ScF\zeta' - ScF'\zeta = 0, \tag{15}$$

with the boundary conditions:

$$F(0) = 0, F'(0) = 1, \Theta(0) = 1, \zeta(0) = 1,$$
$$F'(\eta) \to 0, F''(\eta) \to 0, \Theta(\eta) \to 0, \zeta(\eta) \to 0 \; as \; \eta \to \infty \tag{16}$$

where, prime represents differentiation with respect to similarity variable η.

$k = \frac{\alpha_1 c}{\rho\nu}$, $M = \frac{\sigma B_0^2}{\rho c}$, $\epsilon = \frac{\nu}{K\prime c}$, $\lambda = \frac{g\beta_T(T_w - T_\infty)}{c^2 x}$, $N = \frac{\beta_C(C_w - C_\infty)}{\beta_T(T_w - T_\infty)}$, $Pr = \frac{\nu}{\alpha}$, $Ec = \frac{c^2}{AC_p}$, $Sc = \frac{\nu}{D}$ and $R = \frac{4\sigma^* T^3}{\alpha k^* \rho C_p}$ are the Visco-elastic parameter, Magnetic parameter, porosity parameter, mixed convection parameter, buoyancy ratio parameter, Prandtl number, Eckert number, Schmidt number, and radiation parameter respectively.

The skin friction coefficient C_f, local Nusselt number Nu_x, and local Sherwood number Sh_x are the physical quantities that are significant in our current topic since they have been used across engineering and industrial processes. These are described as

$$C_f = \frac{\tau_w}{\rho U_w^2}, Nu_x = \frac{x p_w}{K(T_w - T_\infty)}, Sh_x = \frac{p_m x}{D(C_w - C_\infty)}. \tag{17}$$

where τ_w, p_w and p_m are the shear stress or skin friction along the surface of the sheet defined, heat flux and mass flux respectively are given by:

$$\tau_w = \mu\left(\frac{\partial u}{\partial y}\right)_{y=0}, p_w = -k\left(\frac{\partial T}{\partial y}\right)_{y=0}, p_m = -D\left(\frac{\partial C}{\partial y}\right)_{y=0}. \tag{18}$$

Inputting Equation (20) into Equation (19), we obtain:

$$F''(0) = (Re_x)^{\frac{1}{2}} C_f, -\Theta'(0) = (Re_x)^{\frac{1}{2}} Nu_x, -\zeta'(0) = (Re_x)^{\frac{1}{2}} Sh_x. \tag{19}$$

where, $Re_x = \frac{u_w x}{\nu}$ is the local Reynolds number.

3. Numerical approach

The two primary finite difference codes for solving systems of ordinary differential equations in MATLAB are bvp4c and bvp5c. The bvp4c numerical approach is one of the most widely used approaches in MATLAB for solving coupled differential equations. The numerical approach of the bvp4c code, which we are applying in the present scenario, might be broken down into multiple steps. Using similarity transformations and dimensionless variables, Equations (7)–(10) and their boundary conditions are transformed into ODEs in the preliminary phases. In the subsequent stage, Equations (13)–(15) are transformed into a new system of first-order ordinary differential equations.

Beginning with initial key guesses, a system of equations with boundary conditions is solved. The result of this problem can be displayed on a graph. Tables will display the values for the Nusselt number and the Sherwood number, and comparative data will be interpreted.

4. Results and discussion

4.1. Magnetic effect on physical quantities

Due to the Lorentz force's influence on the flowing fluid in **Figure 1a**, velocity decreases at increasing amounts of magnetic field M = 0.0, 0.3, and 0.6. As shown in **Figure 1b** and **1c**, the opposite effect, i.e., a rise in temperature and fluid concentration, can be observed when the magnetic field is increased.

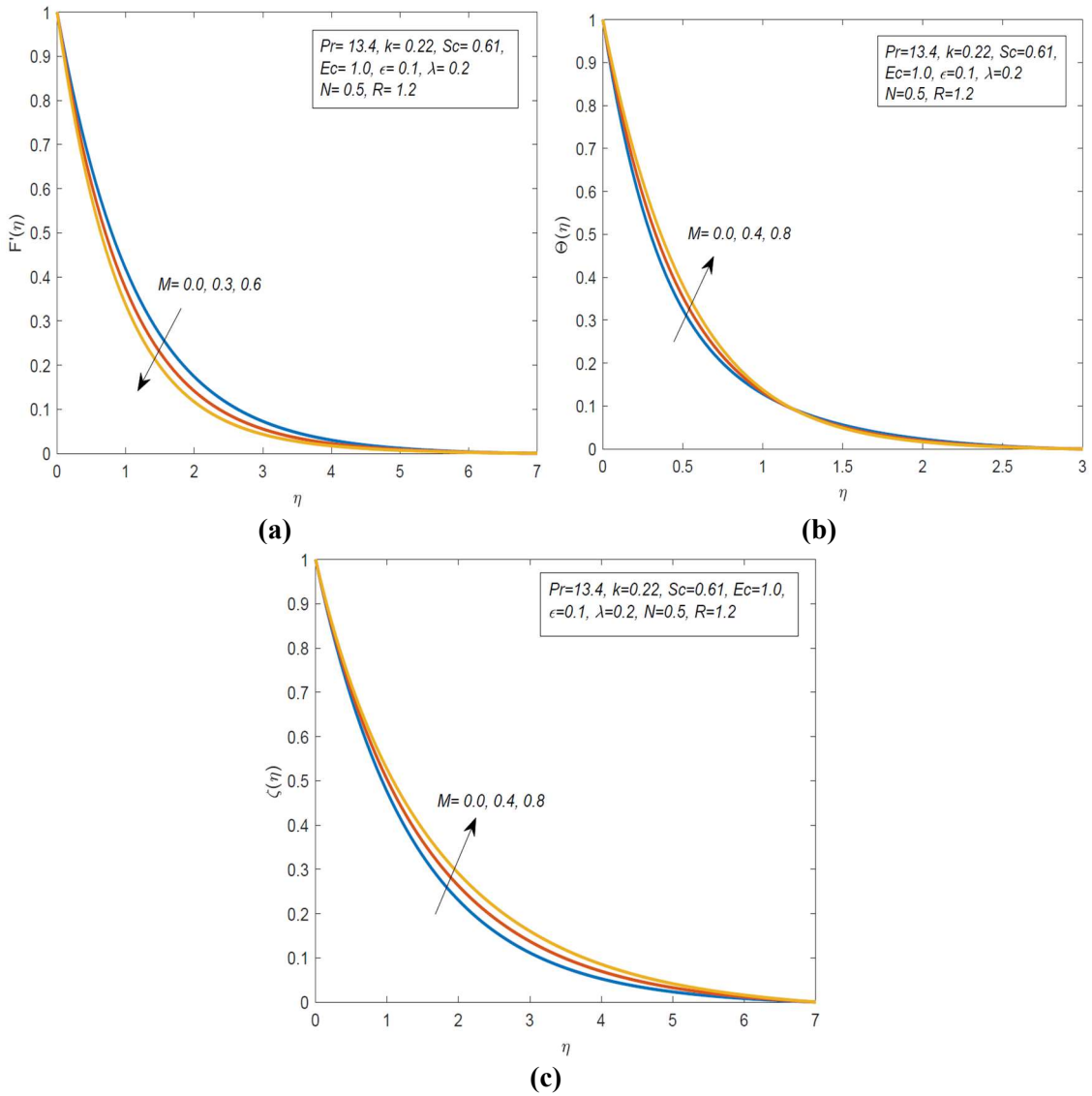

Figure 1. Effect of magnetic parameter on **(a)** velocity **(b)** temperature and **(c)** concentration.

4.2. Thermal radiation and viscoelastic effect on physical quantities

Because thermal radiation is brought on by the thermal motion of fluid particles, the temperature of the fluid rises with increasing thermal radiation parameters R = 0.0, 1.0, and 2.0, as illustrated in **Figure 2**. The interaction involving velocity and temperature is examined in **Figure 3a** and **3b**. The increasing values of k = 0.1, 0.3, and 0.5, which represent higher deformation rates, demonstrate that velocity climbs and reaches zero at about η = 2.5. Temperature decreases by growing

k in the range $0 \leq k \leq 0.7$ but increases in the range $0.8 \leq k \leq 1.8$ because it has both elastic and viscous properties.

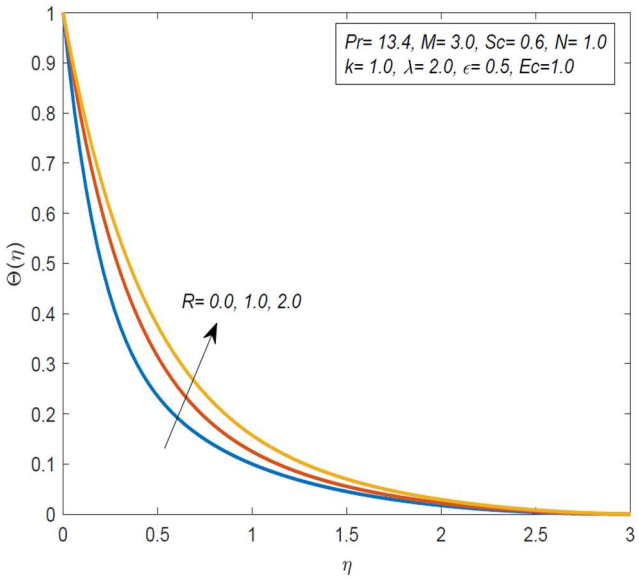

Figure 2. Effect of radiation parameter on temperature.

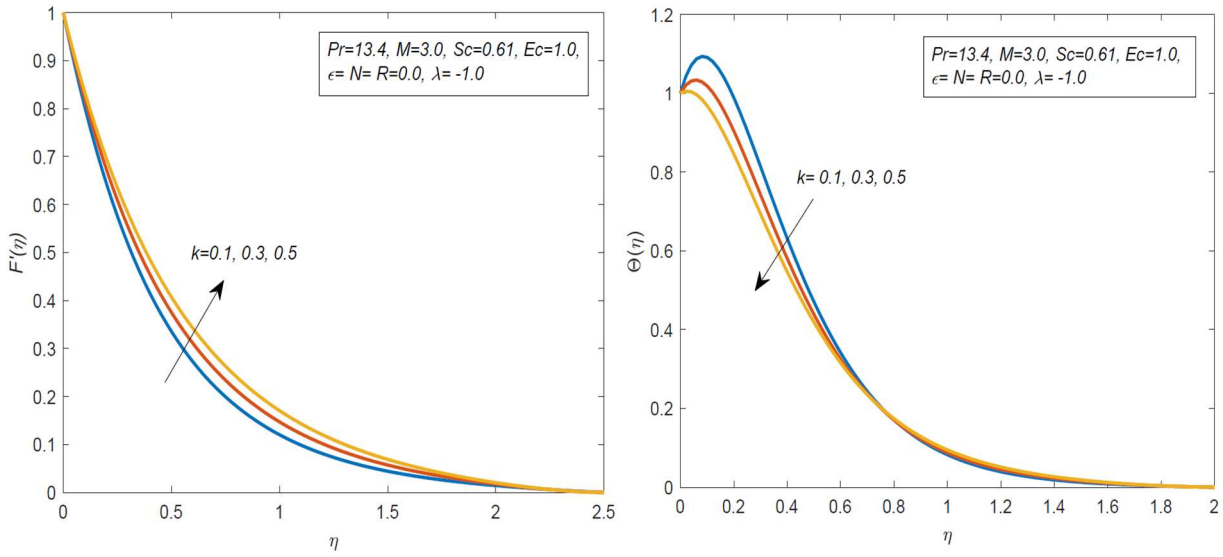

(a) **(b)**

Figure 3. Effect of viscoelastic parameter on **(a)** velocity and **(b)** temperature.

4.3. Porous and buoyancy ratio parameter on physical quantities

The porosity parameter ϵ is inversely proportional to the permeability of the porous medium K'. This leads to a reduction in the velocity profile and an inclination in the concentration profile, as depicted in **Figure 4a** and **4b**. The parameter buoyancy reflects the upward force present in the flowing fluid. By increasing the buoyancy ratio parameter N to values of 0.0, 1.0, and 2.0, fluid velocity increases, as shown in **Figure 5a**. However, the temperature profile exhibits a reverse tendency, as seen in **Figure 5b**.

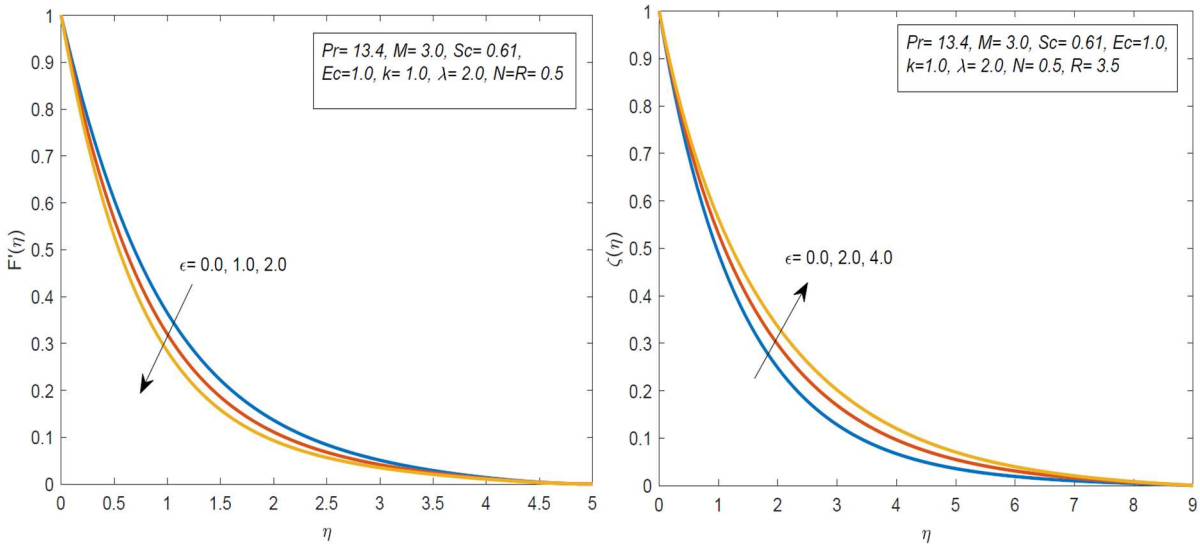

(a) **(b)**

Figure 4. Effect of porous parameter on **(a)** velocity and **(b)** concentration.

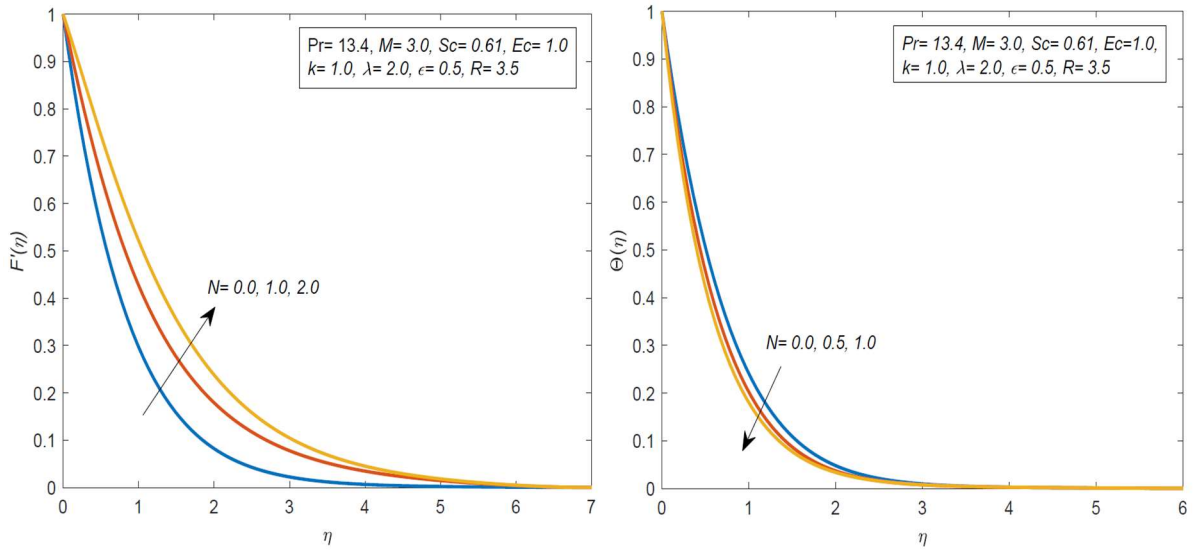

(a) **(b)**

Figure 5. Effect of buoyancy ratio parameter on **(a)** velocity and **(b)** temperature.

4.4. Schmidt number impact on physical quantities

The dimensionless Schmidt number *Sc*, stands for the ratio of momentum to mass diffusivity, and the same pattern can be seen for both velocity and concentration profiles as shown in **Figure 6a** and **6b**, i.e., decreasing when *Sc* = 0.5, 1.0, and 1.5 for velocity and *Sc* = 0.45, 0.55, and 0.65 for concentration.

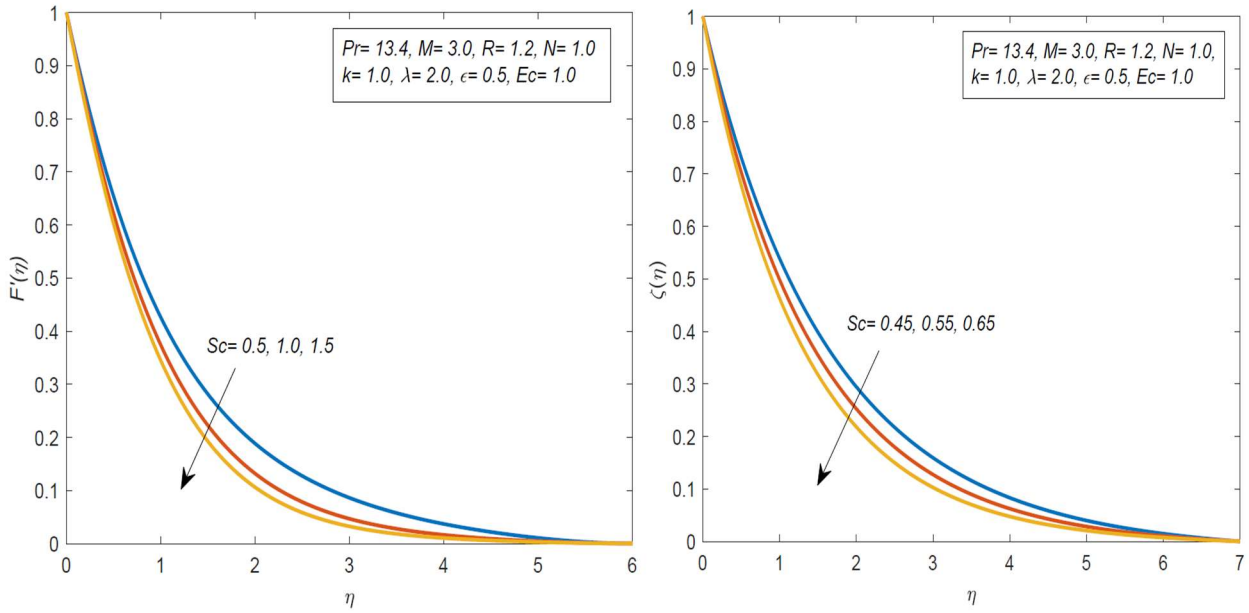

(a) **(b)**

Figure 6. Effect of Schmidt number on **(a)** velocity and **(b)** concentration.

4.5. Impact of physical parameters on Nusselt and Sherwood numbers

The Nusselt and Sherwood numbers, which depict heat and mass transport in a flowing fluid, respectively, are the other two physical measurements of relevance in this study. These studies will be shown in **Tables 1** and **2**, and their error is made noticeable when comparing them to the results of earlier investigations. **Table 1** shows the Nusselt number $-\Theta'(0)$ for various values of η and k when the Prandtl number is supposed to be one. For k = 0.01 and various η values, the Nusselt number increases, and a similar pattern has been observed for k = 0.05. The obtained results demonstrate good agreement with the analytical findings of Ghadikolaei et al. [27]. The obtained results of the Sherwood number $-\zeta'(0)$ using the shooting technique for various values of *Pr* and *Sc* in **Table 2** by setting k = 0.01, M = 2, Ec = 1 while leaving the other parameter values.

Table 1. Comparison of numerical results of Nusselt number $(-\Theta'(0))$ for different values of visco-elastic parameter (k) and similarity variable η when $R = 0$, $N = 0$, $Pr = 1$, $Sc = 0$, $\lambda = 0$, $\epsilon = 0$, $Ec = 0$ and $M = 0$.

Value of 'k'	η	Dey and Borah (first solution) [26]	Ghadikolaie et al. [27]	Present results
	0	1.3278	1.334722	1.3337
0.01	0.1	1.1627	1.150370	1.1477
	0.2	0.9963	0.993877	0.99001
	0	1.3393	1.340277	1.3388
0.05	0.1	1.1738	1.155672	1.1526
	0.2	0.9953	0.998583	0.9946

Table 2. Numerical results of Sherwood number ($-\zeta'(0)$) for different values of Prandtl number (Pr) and Schmidt number (Sc) when $R = 0$, $N = 0$, $k = 0.01$, $\lambda = 0$, $\epsilon = 0$, $Ec = 1$ and $M = 2$.

Pr	***Sc***	$-\boldsymbol{\zeta'(0)}$
0.015	0.22	0.3497
7	0.22	0.3510
13.4	0.30	0.4031
13.4	0.60	0.5962

5. Conclusions

We employed MHD and thermal radiation to study the flow of second-grade fluid across a stretching sheet. When compared to the analytical results, the error is estimated. An analogous correlation between temperature and concentration is revealed by the magnetic field variance. It is found that when the magnetic field increases (= 0, 0.3, 0.6), the flow's velocity gradually decreases and becomes zero when $\eta \geq 7$. While comparing the numerical results with the studies of Ghadikolaei et al. [27], one of the primary investigations in this research. **Table 2** clearly shows that by treating Prandtl number 13.4 and increasing Sc from 0.30 to 0.60, the mass transfer rate increases from 0.4 to 0.59. Graphical observations reveal that both velocity and concentration diminish with increasing values of the Schmidt number. It is crucial to remember that the results of future research using various effects and other numerical approaches may differ from those of the current study. The other numerical methods may give more approximate results compared to the bvp4c technique, which is one of the limitations of this study. Various numerical and analytical methods can be used to determine the errors of physical quantities of interest.

Author contributions: Conceptualization, KGC and BPM; methodology, KGC; software, KGC; validation, KGC, and BPM; formal analysis, BPM; investigation, KGC; resources, BPM; data curation, KGC; writing—original draft preparation, KGC; writing—review and editing, KGC; visualization, BPM; supervision, BPM; project administration, BPM. All authors have read and agreed to the published version of the manuscript.

Conflict of interest: The authors declare no conflict of interest.

References

1. Misra J, Patra M, Misra S. A non-Newtonian fluid model for blood flow through arteries under stenotic conditions. Journal of biomechanics. 1993; 26(9): 1129-1141. doi: 10.1016/S0021-9290(05)80011-9
2. Jacobson BO, Hamrock BJ. Non-Newtonian Fluid Model Incorporated into Elastohydrodynamic Lubrication of Rectangular Contacts. Journal of Tribology. 1984; 106(2): 275-282. doi: 10.1115/1.3260901
3. Crane LJ. Flow past a stretching plate. Zeitschrift für angewandte Mathematik und Physik ZAMP. 1970; 21(4): 645-647. doi: 10.1007/bf01587695
4. Sakiadis BC. Boundary-layer behavior on continuous solid surfaces: I. Boundary-layer equations for two-dimensional and axisymmetric flow. AIChE Journal. 1961; 7(1): 26-28. doi: 10.1002/aic.690070108
5. Sakiadis BC. Boundary-layer behavior on continuous solid surfaces: II. The boundary layer on a continuous flat surface.

AIChE Journal. 1961; 7(2): 221-225. doi: 10.1002/aic.690070211
6. Hamad MAA. Analytical solution of natural convection flow of a nanofluid over a linearly stretching sheet in the presence of magnetic field. International Communications in Heat and Mass Transfer. 2011; 38(4): 487-492. doi: 10.1016/j.icheatmasstransfer.2010.12.042
7. Wang CY. Analysis of viscous flow due to a stretching sheet with surface slip and suction. Nonlinear Analysis: Real World Applications. 2009; 10(1): 375-380. doi: 10.1016/j.nonrwa.2007.09.013
8. Khan JA, Mustafa M, Hayat T, et al. On Three-Dimensional Flow and Heat Transfer over a Non-Linearly Stretching Sheet: Analytical and Numerical Solutions. Rao Z, ed. PLoS ONE. 2014; 9(9): e107287. doi: 10.1371/journal.pone.0107287
9. Hayat T, Muhammad T, Shehzad SA, et al. An analytical solution for magnetohydrodynamic Oldroyd-B nanofluid flow induced by a stretching sheet with heat generation/absorption. International Journal of Thermal Sciences. 2017; 111: 274-288. doi: 10.1016/j.ijthermalsci.2016.08.009
10. Tzirtzilakis EE, Tanoudis GB. Numerical study of biomagnetic fluid flow over a stretching sheet with heat transfer. International Journal of Numerical Methods for Heat & Fluid Flow. 2003; 13(7): 830-848. doi: 10.1108/09615530310502055
11. Datti PS, Prasad KV, Subhas Abel M, et al. MHD visco-elastic fluid flow over a non-isothermal stretching sheet. International Journal of Engineering Science. 2004; 42(8-9): 935-946. doi: 10.1016/j.ijengsci.2003.09.008
12. Schmitt RW. Double Diffusion in Oceanography. Annual Review of Fluid Mechanics. 1994; 26(1): 255-285. doi: 10.1146/annurev.fl.26.010194.001351
13. Turner JS. Double-Diffusive Phenomena. Annual Review of Fluid Mechanics. 1974; 6(1): 37-54. doi: 10.1146/annurev.fl.06.010174.000345
14. Turner JS. Double-diffusive intrusions into a density gradient. Journal of Geophysical Research: Oceans. 1978; 83(C6): 2887-2901. doi: 10.1029/jc083ic06p02887
15. Hayat T, Ahmed N, Sajid M, et al. On the MHD flow of a second grade fluid in a porous channel. Computers & Mathematics with Applications. 2007; 54(3): 407-414. doi: 10.1016/j.camwa.2006.12.036
16. Vajravelu K, Rollins D. Hydromagnetic flow of a second grade fluid over a stretching sheet. Applied Mathematics and Computation. 2004; 148(3): 783-791. doi: 10.1016/S0096-3003(02)00942-6
17. Bafakeeh OT, Raghunath K, Ali F, et al. Hall Current and Soret Effects on Unsteady MHD Rotating Flow of Second-Grade Fluid through Porous Media under the Influences of Thermal Radiation and Chemical Reactions. Catalysts. 2022; 12(10): 1233. doi: 10.3390/catal12101233
18. Massoudi M, Vaidya A. On some generalizations of the second grade fluid model. Nonlinear Analysis: Real World Applications. 2008; 9(3): 1169-1183. doi: 10.1016/j.nonrwa.2007.02.008
19. Gowda RP, Baskonus HM, Naveen Kumar R, et al. Computational Investigation of Stefan Blowing Effect on Flow of Second-Grade Fluid Over a Curved Stretching Sheet. International Journal of Applied and Computational Mathematics. 2021; 7(3). doi: 10.1007/s40819-021-01041-2
20. Awan AU, Abid S, Ullah N, et al. Magnetohydrodynamic oblique stagnation point flow of second grade fluid over an oscillatory stretching surface. Results in Physics. 2020; 18: 103233. doi: 10.1016/j.rinp.2020.103233
21. Khan Y, Akram S, Razia A, et al. Effects of Double Diffusive Convection and Inclined Magnetic Field on the Peristaltic Flow of Fourth Grade Nanofluids in a Non-Uniform Channel. Nanomaterials. 2022; 12(17): 3037. doi: 10.3390/nano12173037
22. Kotnurkar AS, Giddaiah S. Double diffusion on peristaltic flow of nanofluid under the influences of magnetic field, porous medium, and thermal radiation. Engineering Reports. 2020; 2(2). doi: 10.1002/eng2.12111
23. Asha SK, Sunitha G. Influence of thermal radiation on peristaltic blood flow of a Jeffrey fluid with double diffusion in the presence of gold nanoparticles. Informatics in Medicine Unlocked. 2019; 17: 100272. doi: 10.1016/j.imu.2019.100272
24. Asha SK, Sunitha G. Thermal radiation and Hall effects on peristaltic blood flow with double diffusion in the presence of nanoparticles. Case Studies in Thermal Engineering. 2020; 17: 100560. doi: 10.1016/j.csite.2019.100560
25. Akbar N, Khan z, Nadeem S, et al. Double-diffusive natural convective boundary-layer flow of a nanofluid over a stretching sheet with magnetic field. International Journal of Numerical Methods for Heat & Fluid Flow. 2016; 26(1): 108-121. doi: 10.1108/hff-01-2015-0019
26. Dey D, Borah R. Stability analysis on dual solutions of second- grade fluid flow with heat and mass transfers over a stretching sheet. International Journal of Thermofluid Science and Technology. 2021; 8(2). doi: 10.36963/ijtst.2021080203

27. Ghadikolaei SS, Hosseinzadeh Kh, Yassari M, et al. Analytical and numerical solution of non-Newtonian second-grade fluid flow on a stretching sheet. Thermal Science and Engineering Progress. 2018; 5: 309-316. doi: 10.1016/j.tsep.2017.12.010
28. Endalew MF, Sarkar S. Capturing the Transient Features of Double Diffusive Thin Film Flow of a Second Grade Fluid Through a Porous Medium. International Journal of Applied and Computational Mathematics. 2019; 5(6). doi: 10.1007/s40819-019-0743-7.

Thermal Science and Engineering 2024, 7(1), 6137.
https://doi.org/10.24294/tse.v7i1.6137

Article

Temperature characteristics of a wood-insulated refrigeration system for chilling and preservation of agricultural products

Taiwo O. Oni[1,2,*], Bernard A. Adaramola[3], David Bamidele[1], Jerry Adaji[1], Isaac O. Akene[1], Oluwadunsin Osubu[1], Abraham Isiaka[1]

[1] Department of Mechanical Engineering, College of Engineering, Landmark University, Omu-Aran 251103, Nigeria
[2] Department of Mechanical Engineering, Faculty of Engineering, Ekiti State University, Ado-Ekiti 360001, Nigeria
[3] Department of Mechanical and Mechatronics Engineering, College of Engineering, Afe Babalola University, Ado-Ekiti 360001, Nigeria
*** Corresponding author:** Taiwo O. Oni, tooni1610@yahoo.com

CITATION

Oni TO, Adaramola BA, Bamidele D, et al. Temperature characteristics of a wood-insulated refrigeration system for chilling and preservation of agricultural products. Thermal Science and Engineering. 2024; 7(1): 6137.
https://doi.org/10.24294/tse.v7i1.6137

ARTICLE INFO

Received: 8 January 2024
Accepted: 28 February 2024
Available online: 7 March 2024

Abstract: The scarcity of the insulators that are required for refrigeration has made it necessary to use locally available materials that can achieve the desired refrigeration. This work presents the performance evaluation of a refrigerator utilizing a locally available material, which is wood particles that have been converted to particle board, as one of its insulators. A vapor compression refrigeration system was designed and fabricated to chill and preserve agricultural products, which are eggs, yogurt, and tomatoes. The various temperatures at which the agricultural products became chilled were compared with their theoretical preservation temperatures obtainable in literature, thereby evaluating the performance of the refrigerator. The temperature of 11 ℃, which was recorded for the egg in the present experiment, is lower than the theoretical preservation temperatures of 18 ℃ to 21 ℃ for an egg. The temperature of 7 ℃, which was recorded for the yogurt, is approximately equal to its theoretical preservation temperature of 5 ℃. The temperature of 8 ℃, which was recorded for the tomato, is lower than the theoretical preservation temperatures of 7 ℃ to 10 ℃ of tomato. This work has revealed that wood particles have the potential to achieve refrigeration, as well as chill and preserve agricultural products.

Keywords: temperature; refrigeration system; insulator; locally available material; chill; preservation

1. Introduction

In the current era of food scarcity, preservation of agricultural products cannot be set aside, as preservation, according to Jayaraman and Das-Gupta [1], allows better storage life and appreciable reduction of losses at a time of storage of agricultural products by delaying microbial, chemical, and physical processes that lead to food deterioration.

Refrigeration, which is the process of maintaining the temperature of a closed chamber to a value that is less than that of its environment, is one of the means of preservation of agricultural products [2]. During refrigeration, heat is removed from the closed chamber and agricultural products therein (which is at a lower temperature) to its surroundings (which is at a higher temperature). The removal of the heat makes the temperature of the chamber and agricultural products to be reduced and, therefore, cools the agricultural products [2,3]. A refrigerator, which is a device that can be used to carry out refrigeration, should be designed such that it will be able to cool agricultural products to a required temperature that will preserve the products.

The types of refrigerators are air refrigerators, vapor compression refrigerators,

vapor absorption refrigerators, thermoelectric refrigerators, and cascade refrigerators [2,4]. Air refrigerator is one of the earliest devices used for cooling. It became obsolete because of its low coefficient of performance and high operating cost. Absorption refrigeration is referred to as a heat-operated system because it is driven by thermal energy through a generator [3].

A vapor compression refrigerator utilizes a mechanical compressor with the aid of a working fluid to transfer the heat from a space of lower concentration of temperature to another space of a higher concentration of temperature. It depends on the evaporation of the working fluid for its operation. In addition to the compressor, it makes use of an evaporator, a condenser, and an expansion valve. The working fluid changes phases as it moves around the cycle [2]. **Figure 1** shows the removal of heat (Q_R) by a vapor compression refrigerator from a space of a lower concentration of temperature (T_1) to a space of a higher concentration of temperature (T_2), and the work (W) that is done by the compressor on a working fluid.

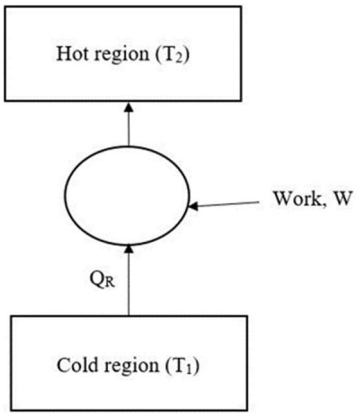

Figure 1. The removal of heat by a refrigerator from a lower to a higher temperature region [2].

The first step toward artificial means of refrigeration was discovered in the sixteenth century when sodium nitrate or potassium nitrate was added to water to cool the temperature to create a sort of refrigeration bath for chilling wine [5]. The first mechanical refrigeration machine, which was proved to be successful on an industrial scale, was developed by James Harrison in 1857. The machines were capable of producing ice or cooling brine [5,6].

Insulation plays a vital role in the effective operation of refrigeration systems, and there exist various advancements in insulators used in refrigerators. Some of them include aerogel [7], polystyrene foam [8], glass wool [9–11], thermocol [11], as well as vacuum insulation panels, polyurethane foam, polyethylene terephthalate foam, and natural fiber insulation [12]. Vacuum insulation panel is made up of a core material surrounded with a gas-tight barrier, minimizing heat transfer, and thereby leading to good insulation. Polyurethane foam insulation has high thermal resistance. Its thin insulation layers without sacrificing performance are a result of its recent improvements in its formulation. Natural fiber insulation, such as hemp or cotton, offers alternatives to conventional synthetic insulation materials, contributing to good performance efforts in refrigeration industries. Aerogel is lightweight materials with extremely low thermal conductivity, and offer the potential for superior insulation

performance in a compact form factor. Polyethylene terephthalate foam is a lightweight and environmentally friendly insulation material that has good potential application as thermal insulation in refrigeration systems [12–14].

As a result of the importance of refrigeration in residences, industries, and offices, the use of refrigeration to maintain a chamber to a temperature that is less than that of its immediate environment has received much attention, and several works have, because of this reason, been done on it.

Brito et al. [15] studied the performance of cold chambers by observing the operating parameters, such as enclosure insulation, external temperature, door opening time, etc. It was discovered that thermal insulation of the enclosures was the operating parameter that had the highest impact on the refrigeration that was obtained.

IIis [7] discovered aerogel insulator as one of the thermal insulators that can show great promise in its applications in refrigerators. Aerogel insulation sheets were put to use on the evaporators as well as the different surfaces of the refrigerator as an additional insulator. The results indicated that the application of the aerogel insulation increased the performance of refrigeration.

The performance of a foam-insulated refrigerator, which made use of a liner made from renewable feedstock, was compared with the one that has a liner made from polystyrene [8]. The results obtained in both cases indicated that the performance of a refrigerator can be improved by insulators.

Gökek and Sahim [16] designed a small thermoelectric refrigeration machine, used it to chill water, and examined the performance evaluation of the machine. It was carefully noticed that the refrigerator effectively chilled the water.

A refrigeration system in which glass wool was used as an insulating material was developed by Patil and Pasare [9]. The glass wool was coated with polymethyl methacrylate. The findings from the work indicated that the insulating material coated with polymethyl methacrylate was better than the one without coating.

Maiorino et al. [17] introduced a phase change material in the cabinet of a refrigerator for the change of temperature in the cabinet of the refrigeration system. The outcome of various control settings on the performance of the refrigeration system was investigated, and it was observed that the inclusion of the phase change material improved the refrigeration of the system.

The evaluation of the performance of a refrigeration system for the preservation of fresh maize was developed by Caleb et al. [10]. The materials used for insulation of the refrigerator are mild steel, glass wool, and stainless steel. The refrigerator preserved the fresh maize above the temperature at which maize freezes. It was observed that there were no noticeable changes in the physical appearance and taste of the maize after the refrigerator had preserved it.

The design, fabrication, and test of a solar refrigerator were carried out by Aich and Nayak [11]. Glass wool was used as the insulator in the position that separated the evaporator's wall and the outer chamber of the refrigerator, but the thermocol was used as the insulator in the position that separated the two layers of stainless steel which has been galvanized. The lowest obtainable temperature inside the refrigerator cabinet showed the refrigerator has a reliable operation with the use of glass wool insulation.

Thermoacoustic refrigeration was designed, and its performance was analyzed by

Prashantha et al. [18]. Helium and hydrogen were considered suitable materials or media that can carry away heat to achieve refrigeration. The report of the analysis on the refrigerator showed that the refrigerator has a reliable performance.

Solanki et al. [19] investigated the analysis of a subcooled vapor compression refrigerator to know its performance for commercial chilling of water. The outcome of the performance test inferred that cooling effect could be obtained from the vapor compression refrigerator.

Kamil et al. [20] designed a refrigerating machine that can create a cooling effect by converting acoustic energy to heat energy. The methodology that was adopted to design the machine involved the use of a loudspeaker utilizing a simulation program. The test that was carried out on the machine indicated that it was able to serve the purpose for which it was designed.

Wang et al. [21] investigated the effect that the suction arrangements have on the performance of the compressor that was used on a refrigerator for cooling. The results revealed that the volumetric efficiency of the compressor of the refrigerator could be increased to a ratio of 1.03:1 by a suction delay of 18 degrees. Also, it was discovered that the volumetric efficiency could be increased further by reducing the distance of the suction bearing.

The utilization of the magnetocaloric effect of a magnetic material to achieve refrigeration was examined by Lee [22] on a refrigerator. Concentric Halbach cylinders, which were made up of magnet segments, were used to build the refrigerator. The thermodynamic analysis that was presented on the refrigerator confirmed that refrigeration can be achieved through the magnetic effect.

From the literature presented above, it can be seen that insulation plays a vital role in the effective operation of refrigeration systems. Moreover, the literature review shows that different researchers have carried out various works on refrigeration systems which make use of different insulation materials, such as glass wool, styrofoam, thermocol, polystyrene, polymethyl methacrylate, and aerogel. In the submission of Kirkpatrick [23], there may be a scarcity of these insulators for the production of refrigeration systems. No doubt, this present research has identified a gap in the literature presented above, which is the absence of usage of locally available materials (for example, wood particles) as insulators for refrigeration machines. Therefore, the present work considers it necessary to fill the gap by taking proactive measures to prevent future problems regarding the scarcity of insulators.

In this research, wood particles (a locally available material), which have been converted to particle board, were used as insulation to design and fabricate a refrigeration system. It is important to note that the use of a locally available insulator promotes local content. The refrigerator was used to chill and preserve agricultural products, namely eggs, yohurt, and tomatoes, and the temperatures of the chilled products were compared with their theoretical storage temperatures obtained from the literature.

2. Methodology

This section presents the details of the methodology that was used in the present work. The section is divided into three, namely, the materials used for the work, the

fabrication of the refrigerator, and the description of the refrigerator. The flow chart that briefly shows the process of the methodology is shown in **Figure 2**.

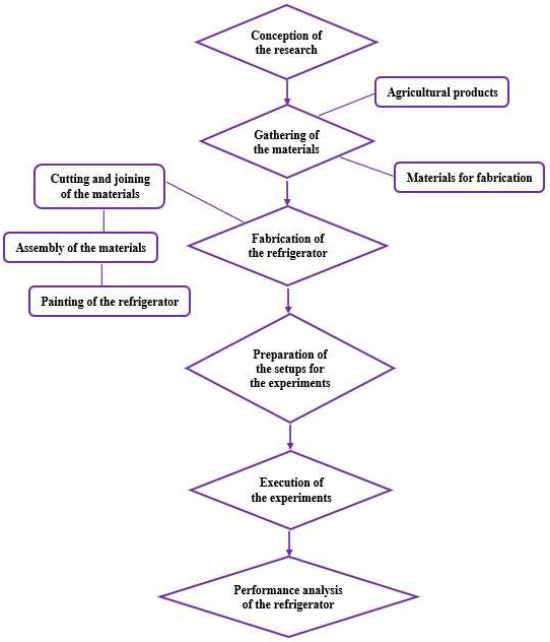

Figure 2. The flow chart of the process of the methodology.

2.1. Materials used for the work

The materials used for the work are agricultural products to be chilled and preserved by the refrigerator, and the materials used for the fabrication of the refrigerator. The agricultural products are eggs, yogurt, and tomato. The products were placed in the interior of the refrigerator. The materials that were used for the fabrication of the refrigerator and their descriptions are shown in **Table 1**.

Table 1. The materials that were used for the fabrication of the refrigerator and their descriptions.

Materials	Descriptions
Mild steel sheet (1 mm thick)	Used for the outer casing of the refrigerator
Particle board (50 mm thick)	A product of wood particles (a locally available material) used as outer insulation of the refrigerator
Polyvinyl chloride PVC (7 mm thick)	Used as the middle insulator of the refrigerator
Aluminum foil (0.5 mm thick)	Used as the inner insulator of the refrigerator
Angle bar (25.4 mm × 25.4 mm, 2 mm thick)	Used to form the framework for the refrigerator
Compressor	A device that moves the refrigerant through the refrigerator
Condenser	A device that takes away heat from the hot refrigerant vapor and condenses into a liquid in saturated state
Evaporator	A device in which the refrigerant circulating inside the refrigerator absorbs the heat energy from the products inside the refrigerator which are then cooled
Expansion valve	A device that lowers the refrigerant's pressure before it enters the evaporator; the pressure drop cools the refrigerant, and then the refrigerant is sprayed into the evaporator
Thermostat	It controls the cooling process by monitoring the temperature and then switching the compressor on and off
Electrical connection	It supplies electric current to the refrigeration system

2.2. Fabrication of the refrigerator

The mild steel sheet and angle bar were cut into the required sizes by a shearing machine. The particle board and the polyvinyl chloride were cut to the required sizes by a circular saw and a hacksaw, respectively. The pieces of the angle bar were joined together by an electric arc welding to form a framework for the refrigerator. The mild steel sheet was fastened to the framework (made from the angle bar) by a power screw machine. The mild steel sheet forms a casing for the refrigerator and the framework makes the casing to be rigid. The particle board was fastened to the framework by a power screw machine. The polyvinyl chloride was installed by laying it on the internal surface of the particle board and then using a hammer tacker to fasten it. The aluminum foil was laid on the polyvinyl chloride with glue and a hammer tacker. **Figure 3** depicts the laying of the walls of the refrigerator.

Figure 3. The laying of the walls of the refrigerator.

The following components were installed on the refrigerator after the insulators had been laid: a compressor, an evaporator, a condenser, an expansion valve, a thermostat, refrigerant lines, and electrical connections (wire and plug). **Figure 4** portrays the installation of these components. After the refrigerator had been fabricated, it was painted white color, as shown in **Figure 5**.

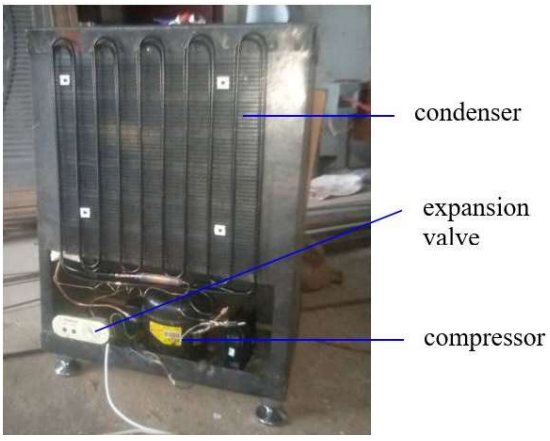

Figure 4. The installation of other components of the refrigerator.

Figure 5. The refrigerator painted white colour.

2.3. Experimental setups

The experimental setups for the egg, yogurt, tomato, and the combined egg, yogurt and tomato are presented in **Figure 6a–d**, respectively. The temperature of the agricultural products was taken using the Type-K digital thermometer before they were put inside the refrigerator. At an interval of half an hour, the temperatures of each of the agricultural products inside the refrigerator were taken and recorded. Thus, the various temperatures at which the egg, yogurt, tomato, and the combined egg, yogurt and tomato were chilled were recorded.

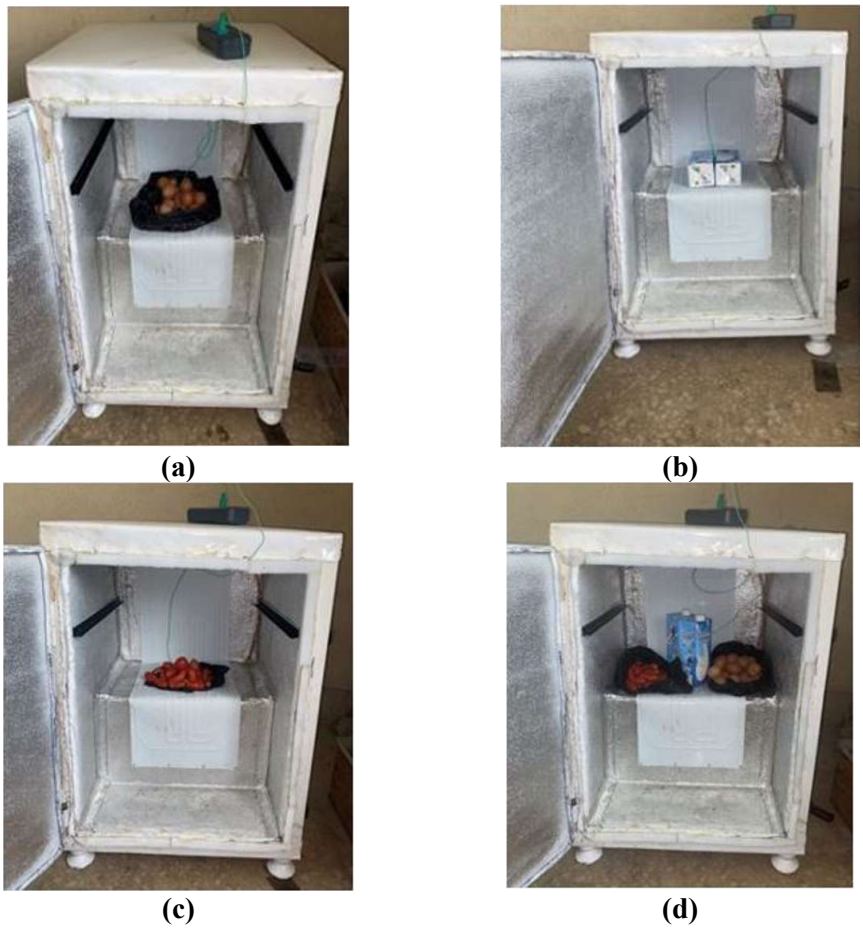

(a) **(b)**

(c) **(d)**

Figure 6. The experimental setups for the temperature drops. **(a)** egg; **(b)** yogurt; **(c)** tomato; **(d)** combined egg, yogurt and tomato.

2.4. Relations for passive and active loads

The two major contributors to refrigeration load are passive and active loads [6].

2.4.1. Passive load

To calculate the heat load from the refrigerator's walls, it is necessary to know the materials chosen for the walls. In addition, the area of the refrigeration chamber should be known. The materials from which the refrigerator's walls were designed are aluminum sheet (internal insulator), polyvinyl chloride (middle insulator), particle board, which is a product of wood particles (outer insulator), and mild steel sheet (outer casing), as presented in **Table 2**.

Table 2. The materials of the walls of the refrigerator.

Material	Thermal conductivity (W/m.K) [24]	Thickness (m)
Aluminum foil	0.00016	0.0005
Polyvinyl chloride	0.15	0.007
Particle board	0.065	0.050
Mild steel sheet	41	0.001

The refrigeration chamber has two compartments. The first one has the inside dimensions of 0.48 m length, 0.32 m breadth, 0.39 m height. The second compartment has the dimensions of 0.48 m length, 0.20 m breadth, 0.27 m height. From **Table 2**, the total thickness of the wall of the refrigerator is 0.117 m (that is, 0.0585 m × 2). Therefore, the outside dimensions of the refrigerator are 0.60 m, 0.56 m, and 0.78 m, respectively. The inside dimensions of the refrigerator are shown in **Figure 7**.

Figure 7. The inside dimensions of the refrigerator.

The inside surface area (A) of the refrigerator is:

[Area of top of the refrigerator] + [Area of one side of the refrigerator] + [Area of top of other side of the refrigerator] + [Area of the front of the refrigerator]. This gives:

$$A = [0.48\ \text{m} \times 0.32\ \text{m}] + [(0.32\ \text{m} \times 0.39\ \text{m}) + (0.20\ \text{m} \times 0.27\ \text{m})] + [(0.32\ \text{m} \times 0.39\ \text{m}) + (0.20\ \text{m} \times 0.27\ \text{m})] + [0.48\ \text{m} \times (0.39\ \text{m} + 0.27\ \text{m})]$$

$$A = 0.1536\ \text{m}^2 + 0.1788\ \text{m}^2 + 0.1788\ \text{m}^2 + 0.3168\ \text{m}^2$$

$$A = 0.828\ \text{m}^2$$

The passive load, which is the heat conveyed into the refrigeration chamber through the refrigerator's walls, can be represented mathematically in Equation (1), as given by Dincer and Kanoglu [2]:

$$Q_P = UA(\Delta T) \tag{1}$$

$$Q_P = \left(\frac{k_s}{t_s} + \frac{k_b}{t_b} + \frac{k_p}{t_p} + \frac{k_l}{t_l}\right) \times A \times (T_a - T_i) \tag{2}$$

where k_s, k_b, k_s, k_p, and k_l are the thermal conductivity of the mild steel, particle board, polyvinyl chloride and, aluminum foil; t_s, t_b, t_s, t_p, t_l are the thickness of the mild steel, particle board, polyvinyl chloride and aluminum sheet; T_o is ambient temperature (27 ℃); T_i is average preservation temperature for the combination of the agricultural products used in this work.

2.4.2. Active load

The heat load from the agricultural products inside the refrigerator is given in Equation (3), published by Dincer and Kanoglu [2]:

$$Q_m = mc_p\Delta T = mc_p(T_o - T_i) \tag{3}$$

where Q_m is the heat load from the agricultural products, m is the mass of the products, c_p is the specific heat capacity of the products T_o is the temperature of the products inside the refrigerator at the start of the experiment (27 ℃), and T_i is average preservation temperature for the combination of the three products considered in this work.

3. Results and discussions

3.1. Temperature drop of egg

The temperature of the eggs before they were put inside the refrigerator was 27 ℃. As can be seen in the outcomes of the experiment shown in **Figure 8**, the temperature of the eggs on the inside of the refrigerator at the start of the experiment is 27 ℃. At 30, 60, and 90 min thereafter, the temperature of the eggs drops to 25 ℃, 21 ℃, and 18 ℃, respectively. The temperature is 16 ℃, 14 ℃, 12 ℃, and 11 ℃ at intervals of 120, 150, 180, and 210 min, respectively. The preservation temperature of the egg, according to the report of the Department of Plant Sciences at the University of California [25], is 18 ℃ to 21 ℃. This is higher than the temperature of 11 ℃ which was recorded in the present experiment after 210 min. It, therefore, indicates that the refrigerator can chill and preserve eggs. The minimum theoretical preservation temperature, the maximum theoretical preservation temperature, and the experimental preservation temperature (obtained in the present work) of the egg are portrayed in **Figure 9**.

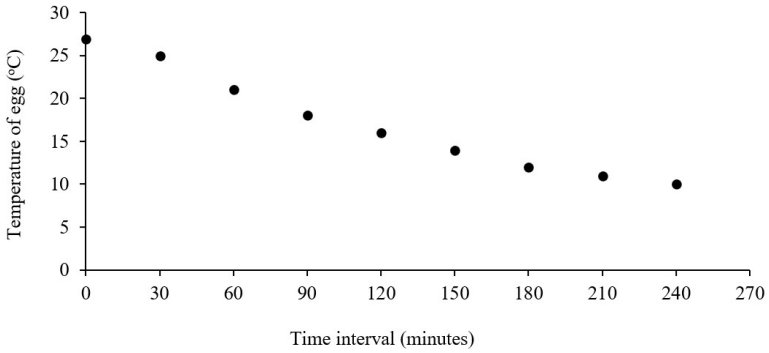

Figure 8. The temperature of the egg.

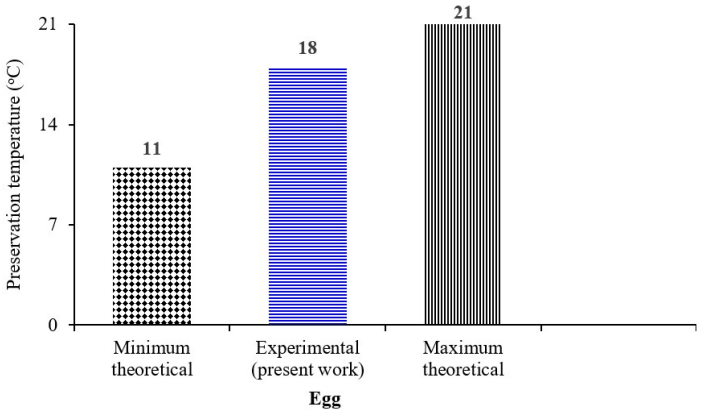

Figure 9. The theoretical and experimental temperatures of the egg.

3.2. Temperature drop of yogurt

The results for the temperature of the yogurt, as shown in **Figure 10**, reveal that a temperature of 27 ℃ was recorded for the yogurt before they were put inside the refrigerator, which was the temperature of the yogurt inside the refrigerator at the start of the experiment. The temperature drops at intervals of 30, 60, 90, and 120 min to 25 ℃, 22 ℃, 20 ℃, and 18 ℃, respectively. The temperature is 17 ℃, 15 ℃, and 13 ℃ at intervals of 150, 180, and 210 min, respectively. The temperature drops at intervals of 240 min and 270 min to 10 ℃ and 7 ℃, respectively. The temperature of 7 ℃ is approximately equal to 5 ℃, which is the theoretical preservation temperature of yogurt [25]. This is an indication that the refrigerator can chill and preserve yogurt. The theoretical preservation temperature and the experimental preservation temperature (obtained in the present work) of the yogurt are depicted in **Figure 11**.

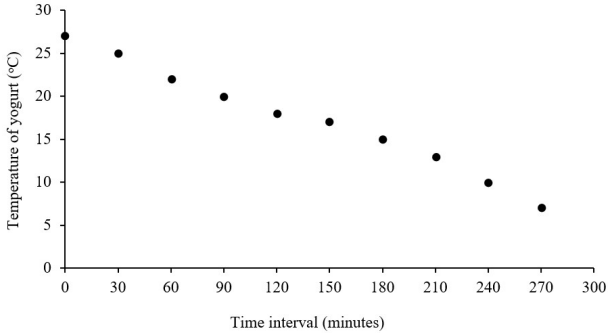

Figure 10. The temperature of the yogurt.

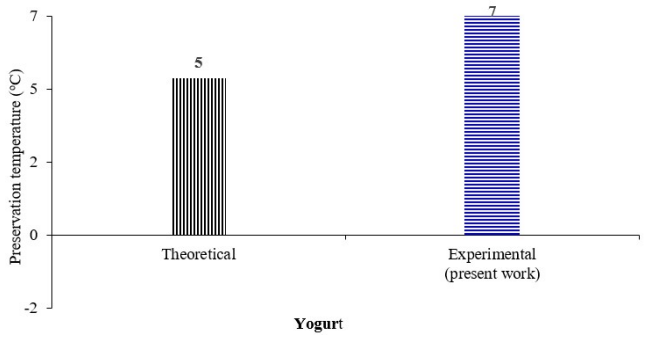

Figure 11. The theoretical and experimental temperatures of the yoghurt.

3.3. Temperature drop of tomato

As can be in the results of the experiment shown in **Figure 12**, the temperature of the tomato inside the refrigerator at the start of the experiment is 27 ℃. At 30 min and 60 min after that, the temperature of the tomato drops to 21 ℃ and 16 ℃, respectively. The temperature is 13 ℃, 10 ℃, and 8 ℃ at intervals of 90, 120, and 150 min, respectively. The theoretical preservation temperature of tomato is 7 ℃ to 10 ℃ [25], whereas the experimental preservation temperature is 8 ℃. Therefore, tomato can be chilled and preserved by the refrigerator. The minimum theoretical preservation temperature, the maximum theoretical preservation temperature, and the experimental preservation temperature (obtained in the present work) of the tomato are displayed in **Figure 13**.

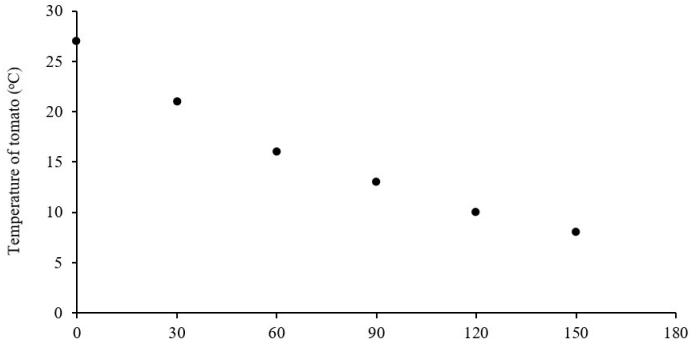

Figure 12. The temperature of the tomato.

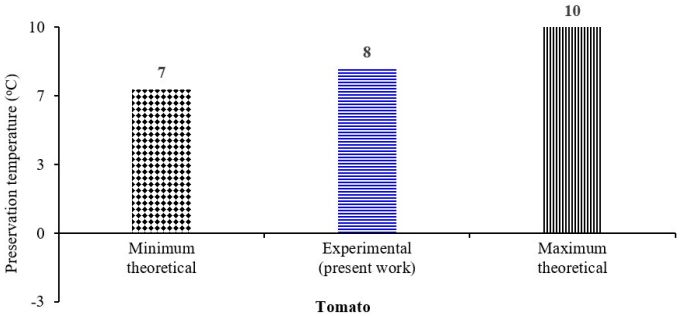

Figure 13. The theoretical and experimental temperatures of the tomato.

3.4. Temperature of the combined egg, yogurt and tomato

The temperature of the combined agricultural product before they were placed inside the refrigerator was 27 ℃. The results of the experiment for the temperature of

the combined agricultural product are shown in **Figure 14**. A temperature of 27 ℃ was recorded for the combined product before they were put inside the refrigerator. The temperature of the combined product inside the refrigerator at the start of the experiment is 27 ℃. The temperature drops at intervals of 30, 60, 90, 120, and 150 min to 23 ℃, 18 ℃, 17 ℃, 16 ℃, and 15 ℃, respectively. The temperature is 14 ℃, 12 ℃, 11 ℃, and 10 ℃ at intervals of 180, 210, 240, and 270 min, respectively. This minimum temperature of 10 ℃, which was recorded for the combined egg, yogurt and tomato at the interval of 270 min, is 1 ℃, 3 ℃, and 2 ℃ deviated from the temperature at which the refrigerator can chill and preserve the egg, yogurt and tomato, respectively. It, therefore, means that the refrigerator can chill and preserve the combined eggs, yogurt and tomatoes at the temperature of 10 ℃.

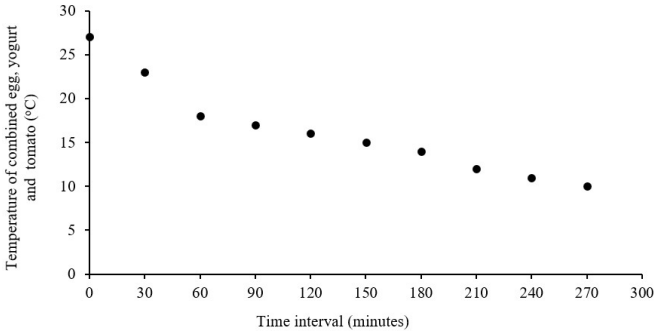

Figure 14. The temperature of the combined egg, yogurt and tomato.

3.5. Passive and active loads

It is necessary to consider the passive and active loads, which are the major contributor loads on the refrigerator. The passive load is the heat load from the refrigerator's walls, whereas the heat load from the agricultural products inside the refrigerator is the active load.

From the previous section, the preservation temperature for the combined egg, yogurt, and tomato is 10 ℃. Substituting the appropriate values into Equation (2) gives the passive load (Q_P):

$$Q_P = \left(\frac{41}{0.001} + \frac{0.065}{0.050} + \frac{0.15}{0.007} + \frac{0.00016}{0.0005}\right)\frac{W/m.K}{m} \times 0.828\, m^2 \times (27 - 10)K$$

$$Q_P = 577.44\, kW.$$

As given in Equation (3) above, the expression for the active load (Q_m) is:

$$Q_m = mc_p\Delta T = mc_p(T_o - T_i)$$

The specific heat capacity of the combined egg, yogurt, and tomato ($C_{p,c}$) [26] is

$$c_{p,c} = x_1c_{p,1} + x_2c_{p,2} + \cdots + x_nc_{p,n} \quad (4)$$

where x is the mass fraction of the components in the combined product, and subscripts 1, 2, …, *n* are the components.

The mass and specific heat capacity of the agricultural products are provided in **Table 3**.

Table 3. The mass and specific heat capacity of the agricultural products.

Agricultural products	Mass (kg)	Specific heat capacity (J/kg.K) [25]
Egg	1.53	888
Yogurt	2.2	3520
Tomato	0.68	3517.4

Applying Equation (4) in conjunction with the mass and specific heat capacity in **Table 3** gives the specific heat capacity of the combined product to be

$$c_{p,c} = \frac{[(1.53 \times 888) + (2.21 \times 3{,}520) + (0.68 \times 3{,}517.4)]\ kg.\frac{J}{kg.K}}{4.42\ kg}$$

$$c_{p,c} = 2{,}608.52\ J/kg.K$$

Substituting the appropriate values into Equation (3) gives the active load (Q_m):

$$Q_m = 4.42\ kg \times 2608.52\ J/kg.K \times (27-10)K = 196.00\ kJ$$

The average time for the combination of the combined product to reach the preservation temperature is 270 min, as can be seen in the above calculations. That is, the active load is $196\ \text{kJ}/270\ \text{mins} = 0.0121\ \text{kW}$.

4. Conclusions

As refrigeration is one of the means of preservation of agricultural products, and in order to explore the potential of locally available materials to achieve the refrigeration, a vapor compression refrigeration system was designed and fabricated to chill and preserve agricultural products, namely eggs, yogurt, and tomatoes.

The refrigerator makes use of wood particles (a locally available material), which have been converted to particle board, as one of its insulators. Different experiments were carried out on the refrigerator to find out the various temperatures at which the agricultural products became chilled and preserve the products.

In the cases of egg and tomato, the experimental preservation temperatures of 11 ℃ and 8 ℃, respectively, obtained in the present work are lower than the theoretical preservation temperature of 18 ℃ to 21 ℃ and 7 ℃ to 10 ℃, respectively, obtainable in the literature. In the case of yogurt, the experimental preservation temperature of 7 ℃ obtained in the present work is approximately the same as the theoretical preservation temperature of 5 ℃ obtainable in the literature. The results give strong indications that the refrigerator can effectively chill and preserve agricultural products.

The performance of the refrigerator further indicated that a locally available material, which is wood particles that have been converted to particle board, can be reliably used as an insulator for the achievement of refrigeration by a refrigerator, making the wood particles an attractive alternative to insulation materials. This will promote local content, and make it easy to take a proactive measure in preventing future problems regarding scarcity of insulators that are required for refrigeration.

Author contributions: Conceptualization, TOO, DB, JA, IOA, OO and AI; methodology, TOO, BAA, DB, JA, IOA, OO and AI; formal analysis, TOO, BAA, DB, JA, IOA, OO, and AI; investigation, TOO, DB, JA, IOA, OO and AI; resources,

TOO, BAA, DB, JA, IOA, OO and AI; data curation, TOO; writing—original draft preparation, TOO, DB, JA, IOA, OO and AI; writing—review and editing, TOO and BAA; supervision, TOO; project administration, TOO. All authors have read and agreed to the published version of the manuscript.

Conflict of interest: The authors declare no conflict of interest.

References

1. Jayaraman KS, Das-Gupta DK. Drying of fruits and vegetables. In: Mujumdar AS (editor). Handbook of Industrial Drying, 2nd ed. CRC Press; 2019. pp. 643–690.
2. Dincer I, Kanoglu M. Refrigeration Systems and Applications, 2nd ed. John Wiley & Sons Ltd; 2010.
3. Andrew DA, Carl HT, Alfred FB. Modern Refrigeration and Air Conditioning, 9th ed. The Goodheart-Willcox Company Inc.; 2004.
4. Wank SK, Lavan Z. Air-conditioning and refrigeration. In: Kreth F (editor). Mechanical Engineering Handbook. CRC Press LLC; 1999.
5. Bhatt MS. Domestic refrigerator: Field studies and energy efficiency improvement. Journal of Science and Industry Research. 2001; 60: 591–600.
6. Arora CP. Refrigeration and Air Conditioning, 3rd ed. Tata Mc Graw-Hill; 2009.
7. Iliş GG. Experimental insulation performance evaluation of aerogel for household refrigerators. In: Dincer I, Midilli A, Kucuk H (editors). Progress in Exergy, Energy, and the Environment. Springer International Publishing; 2014. pp. 495–506.
8. Hossieny N, Shrestha SS, Owusu OA, et al. Improving the energy efficiency of a refrigerator-freezer through the use of a novel cabinet/door liner based on polylactide biopolymer. Applied Energy. 2019; 235: 1–9. doi: 10.1016/j.apenergy.2018.10.093
9. Patil U, Pasare V. Evaluating the performance of insulation material (glass wool) by applying coating on it. International Journal of Engineering Research and Technology. 2017; 10(1): 748–751.
10. Caleb OO, Olaiya NG, Akintunde MA. Performance evaluation of a refrigeration system for fresh maize storage. Journal of Engineering Research and Reports. 2020; 9(4): 1–9. doi: 10.9734/JERR/2019/v9i417025
11. Aich S, Nayak J. Design and fabrication of a solar portable refrigerator. Materials Today: Proceedings. 2021; 39: 1955-1958. doi: 10.1016/j.matpr.2020.08.442
12. Verma S, Singh H. Why and which insulation materials for refrigerators! In: Proceedings of the 25th IIR International Congress of Refrigeration; 24–30 August 2019; Montréal, Canada.
13. Insulation for refrigeration systems. Available online: https://berg-group.com/blog/insulation-for-refrigeration-systems/ (accessed on 13 February 2024).
14. Refrigeration insulation materials market. Available online: https://www.marketsandmarkets.com/Market-Reports/refrigeration-insulation-materials-market-150806980.html (accessed on 13 February 2024).
15. Brito P, Lopes P, Reis P, et al. Simulation and optimization of energy consumption in cold storage chambers from the horticultural industry. International Journal of Energy and Environmental Engineering. 2014; 5: 1–15. doi: 10.1007/s40095-014-0088-2
16. Gökçek M, Sahin F. Experimental performance investigation of mini channel water cooled-thermoelectric refrigerator. Case Studies in Thermal Engineering. 2017; 10: 54–62. doi: 10.1016/j.csite.2017.03.004
17. Maiorino A, Duca MGD, Mota-Babiloni A, et al. The thermal performances of a refrigerator incorporating a phase change material. International Journal of Refrigeration. 2019; 100: 255-264. doi: 10.1016/j.ijrefrig.2019.02.005
18. Prashantha BG, Narasimham GSVL, Seetharamu S, et al. Hydrogen, helium and thermo-acoustic refrigerators. International Journal of Air-Conditioning and Refrigeration. 2023; 31(22). doi: 10.1007/s44189-023-00038-4
19. Solanki N, Arora A, Singh RK. Performance enhancement and environmental analysis of vapor compression refrigeration system with dedicated mechanical subcooling. International Journal of Air-Conditioning and Refrigeration. 2023; 31(26). doi: 10.1007/s44189-023-00042-8
20. Kamil MQ, Yahya SG, Azzawi IDJ. Design methodology of standing-wave thermoacoustic refrigerator: Theoretical analysis. International Journal of Air-Conditioning and Refrigeration. 2023; 31(7). doi: 10.1007/s44189-023-00023-x
21. Wang B, Wu X, Wang C, et al. Performance improvement of twin screw refrigeration compressors for chillers by modifying

the suction arrangement. International Journal of Refrigeration. 2023. doi: 10.1016/j.ijrefrig.2023.11.007
22. Lee JS. Thermodynamic analysis on a magnetic refrigeration system. International Journal of Air-Conditioning and Refrigeration. 2023; 31(23). doi: 10.1007/s44189-023-00040-w
23. Kirkpatrick A. Introduction to Refrigeration and Air Conditioning. Springer; 2017.
24. Bergman TL, Lavine AS, Incropera FP, et al. Fundamentals of Heat and Mass Transfer, 7th ed. John Wiley & Sons, Inc.; 2011.
25. Storage temperature. Available online: https://www.plantsciences.ucdavis.edu/undergraduate-programs (accessed on 11 February 2024).
26. Priya S. What is the specific heat of the mixture when two liquids of masses m1 and m2 and specific heats s1 and s2 respectively are mixed? Available online: https://www.quora.com/What-is-the-specific-heat-of-the-mixture-when-two-liquids-of-masses-m1-and-m2-and-specific-heats-s1-and-s2-respectively-are-mixed (accessed on 15 February 2024).

Thermal Science and Engineering 2024, 7(1), 6126.
https://doi.org/10.24294/tse.v7i1.6126

Article

Data mining model to prediction thermal efficiency in ORC

Erkan Dikmen, Arzu Şencan Şahin*

Mechanical Engineering Department, Technology Faculty, Isparta University of Applied Sciences, Isparta 32260, Turkey
*** Corresponding author:** Arzu Şencan Şahin, arzusencan@isparta.edu.tr

CITATION

Dikmen E, Şencan Şahin A. Data mining model to prediction thermal efficiency in ORC. Thermal Science and Engineering. 2024; 7(1): 6126. https://doi.org/10.24294/tse.v7i1.6126

ARTICLE INFO

Received: 6 January 2024
Accepted: 17 February 2024
Available online: 24 February 2024

Abstract: The Organic Rankine Cycle (ORC) is an electricity generation system that uses organic fluid instead of water in the low temperature range. The Organic Rankine cycle using zeotropic working fluids has wide application potential. In this study, data mining (DM) model is used for performance analysis of organic Rankine cycle (ORC) using zeotropik working fluids R417A and R422D. Various DM models, including Linear Regression (LR), Multi-Layer Perceptron (MLP), M5 Rules, M5 Model Tree, Random Committee (RC), and Decision Tree (DT) models are used. The MLP model emerged as the most effective approach for predicting the thermal efficiency of both R417A and R422D. The MLP's predicted results closely matched the actual results obtained from the thermodynamic model using Genetron software. The Root Mean Square Error (RMSE) for the thermal efficiency was exceptionally low, at 0.0002 for R417A and 0.0003 for R422D. Additionally, the *R*-squared (R^2) values for thermal efficiency were very high, reaching 0.9999 for R417A and R422D. The findings demonstrate the effectiveness of the DM model for complex tasks like estimating ORC thermal efficiency. This approach empowers engineers with the ability to predict thermal efficiency in organic Rankine systems with high accuracy, speed, and ease.

Keywords: ORC; data mining; machine learning; zeotropik working fluids

1. Introduction

It clearly states the critical issue of climate change caused by carbon dioxide emissions from burning fossil fuels. It even cites the International Energy Agency (IEA) statistic of a staggering 36.3 gigatons of CO_2 released into the atmosphere in 2021 [1]. The transition to a more sustainable energy system hinges on two crucial elements: developing renewable energy sources to replace fossil fuels and utilizing waste heat to enhance overall energy conversion efficiency. Notably, within renewable and waste heat resources, there exists a vast potential for development, particularly in the area of medium and low-grade thermal energy. As the use of renewable energy grows and waste heat generation increases, the organic Rankine cycle (ORC) emerges as a highly suitable technology for heat conversion. This is due to its ability to efficiently utilize low-grade thermal energy. The ORC operates on a similar principle to the traditional steam Rankine cycle, but employs organic fluids with lower boiling points as the working fluid [2].

Machine learning, a type of artificial intelligence algorithm, has gained significant interest in recent years. This is due to its ability to effectively handle complex data, with multiple dimensions and variations, even in situations with dynamic or uncertain conditions [3]. In the field of Organic Rankine Cycles (ORCs), some promising research has begun to explore how machine learning can be applied. Several studies documented in academic literature have employed machine learning techniques to estimate and optimize ORC power system performance. **Table 1**

summarizes prior research that investigated ORC systems using various machine learning approaches.

Table 1. Summary of related studies on optimization and performance prediction of ORC systems.

Author (Years)	Working fluid	Estimated property	Method
Arslan and Yetik (2011) [4]	R744	Optimization	Artificial Neural Network (ANN)
Yilmaz et al. (2016) [5]	R410a and R407c	System performance	ANN
Rashidi et al. (2011) [6]	R717	Optimization	ANNs and Artificial Bees Colony (ABC)
Kovacı et al. (2017) [7]	R365-mfc and SES32	Thermal efficiency	Neuro-fuzzy (ANFIS) and ANN
Massimiani et al. (2017) [8]	R1234yf	Optimization	ANN
Yang et al. (2018) [9]	R123	System performance	ANN
Bilgiç et al. (2016) [10]	R245fa, tolüen, siklo-hekzan and solkaterm	Power production	ANN
Dong et al. (2018) [11]	Unspecified	System performance	Support Vector Machine (SVM) and ANN
Kılıç and Arabacı (2019) [12]	R123, R125, R227, R365mfc, and SES36	System performance	ANN and ANFIS
Luo et al. (2019) [13]	Different working fluids	System performance	ANN
Palagi et al. (2019) [14]	Unspecified	System performance	Feed-forward, recurrent (RNN) and long short-term memory (LSTM) networks
Huster et al. (2020) [15]	Different working fluids	Working fuid selection and optimization	ANN
Wang et al. (2020) [16]	R141b, R236ea, R245fa, R245ca, R123, R114 and R11	Thermal and exergy efficiency	SVM and ANN
Peng et al. (2021) [17]	Different working fluids	System performance	ANN

In this paper, unlike the studies in the literature, data mining method is used for the thermal efficiency estimation of the ORC system using R417A and R422D as working fluid. The thermodynamic modeling of the ORC system was performed using the Genetron software (Genetron Properties 1.4.2). The results obtained from the data mining method were compared with the thermodynamic model results (actual results) obtained using the Genetron software. The data mining method will help to predict the thermal efficiency of the ORC system very accurately and quickly.

2. ORC system and thermodynamic modeling

The corresponding system flowchart for the ORC system is presented in **Figure 1**. The basic ORC configuration consists of four essential components [18]:

- Evaporator: This component transfers heat from an external source to the system, vaporizing the high-pressure organic working fluid.
- Turbine: The high-temperature, high-pressure organic working fluid expands in the turbine, generating electricity.
- Condenser: Here, heat is extracted from the low-pressure working fluid exiting the turbine, condensing it back into a liquid state.
- Pump: The pump increases the pressure of the liquid working fluid to match the evaporator pressure, allowing the cycle to repeat.

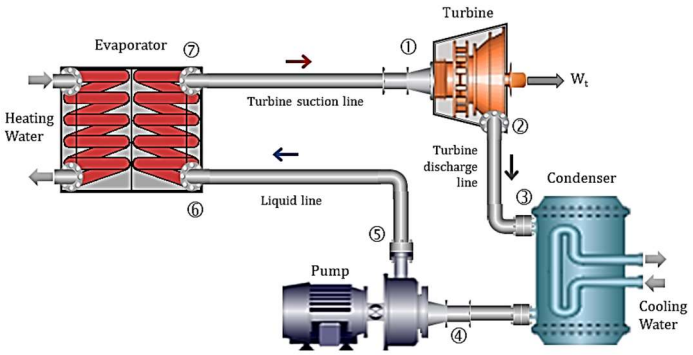

Figure 1. Schematic diagram of ORC.

The four components associated with the ORC (pump, evaporator, turbine and condenser) are steady-state flow devices, and thus the four processes that make up the ORC can be analyzed as a steady flow process which can be expressed as [19,20]:

$$\left(\dot{Q}_{in} - \dot{Q}_{out}\right) + \left(\dot{W}_p - \dot{W}_t\right) = \dot{m}_r(h_{out} - h_{in}) \tag{1}$$

The energy conservation relationship for each component can be expressed as follows:

Pump: The power required to pump the condensed liquid working fluid to the inlet side of the boiler is calculated by the equation:

$$\dot{W}_p = \frac{\dot{m}_r(h_5 - h_4)}{\eta_p} \tag{2}$$

Evaporator: In the evaporator, heat is added to the liquid working fluid so that it changes its phase to gas. The calorific value required by the boiler is calculated by the equation:

$$\dot{Q}_{in} = \dot{m}_r(h_7 - h_6) \tag{3}$$

Turbine: The process of expansion of the working fluid in gaseous form from high pressure to condensing pressure produces turbine power, the output power is calculated by the equation:

$$\dot{W}_t = \dot{m}_r \eta_t(h_1 - h_2) \tag{4}$$

Condenser: In the condenser a certain amount of heat is discharged into the environmental air, and the value of the heat released is calculated by the equation:

$$\dot{Q}_{out} = \dot{m}_r(h_3 - h_4) \tag{5}$$

The performance of ORC systems is usually expressed by thermal efficiency, and is calculated by the equation:

$$\eta = \frac{\dot{W}_{out}}{\dot{Q}_{in}} = \frac{\left(\dot{W}_t - \dot{W}_p\right)}{\dot{Q}_{in}} \tag{6}$$

The thermodynamic modeling of the ORC system was performed using the Genetron software.

Some of parameters and assumptions in this study presented in **Table 2** were selected based on the working range of ORC systems that have been used as small-scale power plants.

Table 2. Research parameters and assumptions.

Parameters	Unit	Value
Turbine output power $(\dot{W}_t)$	kW	70
Evaporator temperature (T_E)	°C	61–77
Condenser temperature (T_C)	°C	26–42
Superheating temperature (ΔT_{SH})	°C	3, 5, 7
Subcooling temperature (ΔT_{SC})	°C	3, 5, 7
Turbine isentropic efficiency (η_t)	-	0.84
Pump isentropic efficiency (η_P)	-	0.72

3. Data mining model and application

Data mining is an interdisciplinary field that integrates elements from databases, statistics, machine learning, signal processing, and high-performance computing. Its primary objective is to uncover meaningful correlations and patterns within existing data that are potentially valuable and understandable. It serves as a potent tool for extracting predictive insights from vast datasets. Data mining tasks can generally be categorized as either predictive or descriptive in nature. Predictive modeling involves the construction of predictive models based on the outcomes of disparate datasets. In contrast, descriptive modeling aims to identify underlying patterns or relationships within the data. Unlike predictive modeling, which focuses on making predictions, descriptive modeling seeks to uncover inherent characteristics of the data being studied rather than predicting new features. Common predictive modeling tasks in data mining include classification, prediction, regression, and time series analysis. Descriptive tasks encompass techniques such as clustering, summarization, association rules, and ranking. **Figure 2** illustrates the various tasks and models in data mining [21].

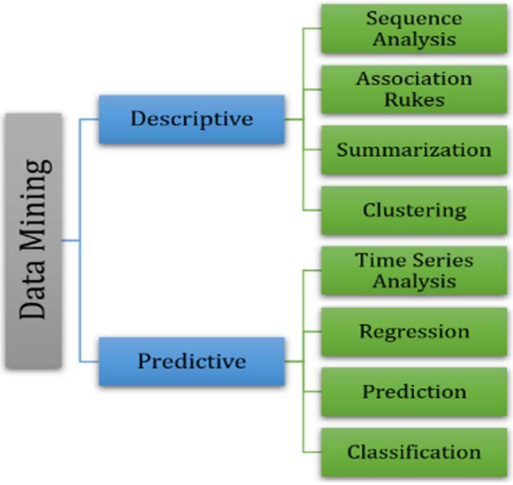

Figure 2. Data mining tasks and models.

Among predictive models, Classification is arguably the most comprehensively understood approach in data mining. Three key characteristics of classification tasks are [22]:

- Supervised learning,
- Categorical dependent variable,
- Ability to assign new data to distinct predefined classes.

In contrast to classification, Prediction modeling aims to forecast future outcomes rather than describing current behavior. Its output can be either categorical or numerical.

Another type of forecasting model, known as Statistical Regression, is a supervised learning technique that involves analyzing the relationship between attributes within the same dataset and building a model capable of predicting attribute values for new instances. Forecasting scenarios involving one or more time-dependent attributes are commonly referred to as time series problems.

CRISP-DM (Cross-Industry Standard Process for Data Mining) is a process model management and implementation of data mining projects. It is the most widely-used analytics model. This methodology consists of six phases [23]: Business Understanding, Data Preparation, Modelling, Evaluation and Deployment, as shown in **Figure 3**.

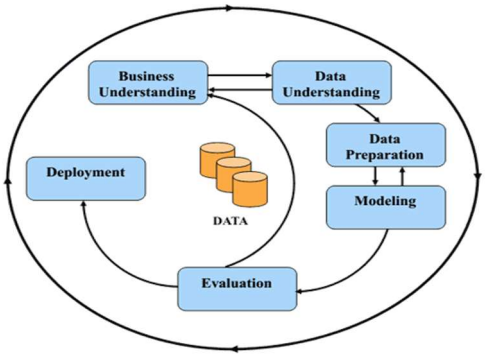

Figure 3. Steps of CRISP-DM Methodology [24].

Business Understanding: It includes business understanding and is the stage where the objectives and requirements are determined. The purpose and business requirements of the data mining are determined. At this stage, objectives and requirements are understood.

Data Understanding: In the data understanding phase, the existing data set is analyzed and understood. Data quality, missing data and data relationships are analyzed at this stage. In this phase,important information about the data is obtained and analyzed. The influence of evaporator, condenser, subcooling, and superheating temperatures on the thermal efficiency of an ORC system is well known. Consequently, these temperatures were selected as the input data in the study. Thermal efficiency is the output data of the data mining model.

Data Preparation: In the data preparation phase, the data is made suitable for data mining operations.The data is cleaned, transformed and brought into a suitable format. At this stage, the data set is madeready to be used in the modelling phase. In this study, the thermodynamic modeling of the ORC system was made using the Genetron software. The data set used to train the network was obtained from the results of the thermodynamic modeling

Modelling: Data mining models are created and tested. At this stage, learning from the data set is performed using different algorithms and techniques. In this study; The Linear Regression (LR), Multi-Layer Perceptron (MLP), Decision Table (DT), M5 rules (M5R), M5P model tree (M5P) and Random Committee (RC) models are applied for the thermal efficiency estimating of the ORC system working with R417A and R422D. Information on these models is given below.

- Linear Regression: Regression analysis is a statistical method utilized to investigate the numerical relationship between two or more variables. Its primary objective is to elucidate the functional relationship between variables and to articulate this relationship through a model. Within regression analysis, when there exists one dependent variable and one independent variable, it is termed as Simple Linear Regression; whereas, if there are multiple independent variables, it is referred to as Multiple Linear Regression. Multivariate Regression analysis represents a generalized form of Multiple Linear Regression analysis, wherein there are multiple dependent variables involved [25].
- Multilayer Perceptron: A multilayer perceptron (MLP) serves as a classifier employing backpropagation for sample classification and learning. These networks, known as feed-forward neural networks, are trained utilizing the standard backpropagation algorithm. Being supervised networks, MLPs necessitate a desired response for training purposes. They learn the process of transforming input data into the desired response, making them extensively employed for pattern classification tasks. Equipped with one or two hidden layers, MLPs demonstrate the capability to approximate nearly any input-output mapping. Moreover, they have demonstrated the ability to approach the performance levels of optimal statistical classifiers even in challenging conditions [26,27].
- M5 Rules: The M5 Rules algorithm is a method that employs the divide-and-conquer approach to construct decision lists for regression tasks. Utilizing the divide-and-conquer technique, the M5 Rules algorithm constructs a model tree, generates rules from the optimal leaf, and subsequently processes the remaining instances in the dataset based on the generated rule. In contrast to PART (Partial Decision Trees), which employs a similar strategy for categorical prediction, M5 Rules constructs complete trees rather than partially explored trees. The generation of partial trees offers enhanced computational efficiency without compromising the size and accuracy of the resultant rules [26].
- M5P: M5P represents a modification of the M5 algorithm tailored for constructing a regression tree model based on experimental data. Within an M5P model, each branch of the tree encapsulates a linear regression model that predicts the class values for the corresponding segment of the dataset reaching the leaf. The dataset undergoes partitioning based on specific data characteristics, allowing for the creation of model trees that extend beyond the traditional fixed-value branches of regression trees. Consequently, model trees resemble piecewise linear functions, thus exhibiting non-linear behavior. Model trees offer enhanced learning efficiency and are adept at handling tasks involving high dimensionality, even up to hundreds of attributes. Noteworthy advantages of

model trees over regression trees include their comparatively smaller size, transparent decision-making processes, and the tendency for regression functions to involve a manageable number of variables [26].

- Random Committee: The Random Committee classifier functions by assembling an ensemble of base classifiers that are randomized in nature. Each base classifier is generated utilizing a distinct random number kernel, albeit based on the same dataset. The ultimate prediction is derived by computing a simple average of the predictions generated by each individual base classifier [28].
- Decision Table: The Decision Table classifier is employed to construct a majority classifier using a straightforward decision table. Through an induction algorithm applied to a labeled training set, this classifier is generated. Two distinct variants of decision table classifiers have been delineated. The first variant, known as DTMaj (Decision Table Majority), returns the majority class of the training set if the corresponding cell in the decision table, corresponding to the new example, is empty, signifying the absence of any training examples. The second variant, termed DTLoc (Decision Table Local), introduces a novel approach by seeking a decision table entry with fewer matching attributes (larger cells) in the event that the matching cell is devoid of examples. Consequently, this variant furnishes a response from the local vicinity, where minor alterations in a pertinent attribute do not induce changes in the label [29,30].

Evaluation: The effectiveness and performance of the models created are evaluated. At this stage, theperformance of the models is evaluated by looking at how well they meet the set objectives. Different statistical criteria can be used to determine the model's performance, such as mean absolute error (MAE), Root Mean Square Error (RMSE), and coefficient of determination (R2), as given below [22].

$$MAE = \frac{1}{n}\sum_{i=0}^{n}\left|y_{e,1} - t_{a,i}\right| \tag{7}$$

$$RMSE = \sqrt{\frac{\sum_{i=1}^{n}\left(y_{e,i} - t_{a,i}\right)^2}{n}} \tag{8}$$

$$R^2 = 1 - \frac{\sum_{i=1}^{n}\left(y_{e,i} - t_{a,i}\right)^2}{\sum_{i=1}^{n}\left(t_{a,m} - \overline{t}_{a,m}\right)^2} \tag{9}$$

In these equations, $y_{e,i}$ refers to the prediction value, $t_{a.i}$ to the true value, $\overline{t}_{a.m}$ to the mean of the true value, and n to the number of data.

Deployment: Successful models are integrated into the business. It is planned how the models will beused and maintained in real conditions.

4. Result and discussion

Different Data mining models (LR, MLP, DT, M5 rules, M5 model tree, and Random Committee) were used to determine the thermal efficiency of the ORC system operating with R417A and R422D working fluids. Data mining analyses were conducted using WEKA 3.9 software (Waikato Environment for Knowledge Analysis). The performance of various models was evaluated using metrics like *R*-squared (R^2), Mean Absolute Error (MAE), and Root Mean Squared Error (RMSE).

The formulas for these metrics are provided earlier in the text. The ideal estimating model is highly accurate, meaning the Mean Absolute Error (MAE) and Root Mean Squared Error (RMSE) approach zero, while the *R*-squared (R^2) value gets as close to 1 as possible. Accordingly, **Tables 3** and **4** show that the best results for the thermal efficiency of the ORC system with R417A and R422D working fluids are obtained using the MLP model.

Table 3. Thermal efficiency values for R417A.

Model	R^2	MAE	RMSE
Linear Regression	0.9983	0.0006	0.0008
Multi Layer Perceptron	0.9999	0.0001	0.0002
Random Committee	0.9874	0.0019	0.0022
Decision Table	0.9062	0.0041	0.0059
M5Rules	0.9992	0.0004	0.0006
M5P	0.9992	0.0004	0.0006

Table 4. Thermal efficiency values for R422D.

Model	R^2	MAE	RMSE
Linear Regression	0.9979	0.0007	0.0009
Multi Layer Perceptron	0.9999	0.0002	0.0003
Random Committee	0.9872	0.0018	0.0022
Decision Table	0.9092	0.0039	0.0057
M5Rules	0.9736	0.0016	0.0032
M5P	0.9996	0.0003	0.0004

For the test data set, the comparison of actual and predicted thermal efficiency of R417A and R422D is shown in **Figure 4**. The correlation coefficient values for R417A and R422D are 0.9961 and 0.9936, respectively.

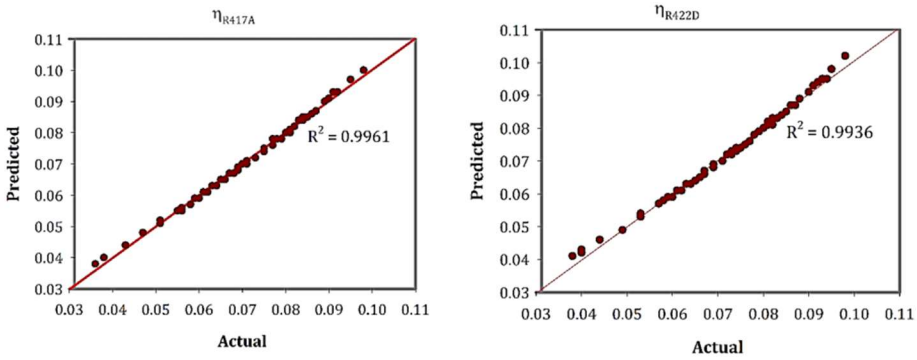

Figure 4. Actual and predicted thermal efficiency for R417A and R422D.

Figure 5 compares the actual thermal efficiency of the ORC system with the efficiencies estimated by the MLP model, for both R417A and R422D working fluids. As the figure shows, thermal efficiency increases with higher evaporator temperatures. The MLP model's estimates closely match the actual efficiency values.

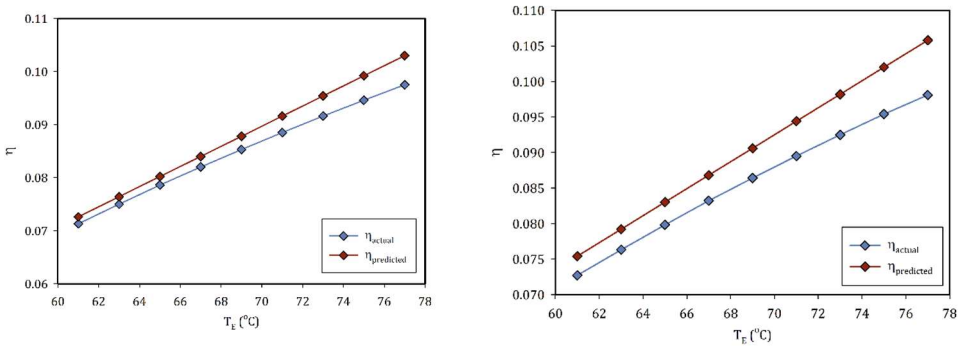

(a) **(b)**

Figure 5. Results comparison of actual thermal efficiency with MLP model results depending on evaporator temperature for R417A and R422D. **(a)** R417A (T_C = 26 °C; ΔT_{SH} = 3 °C; ΔT_{SC} = 3 °C); **(b)** R422D (T_C = 26 °C; ΔT_{SH} = 3 °C; ΔT_{SC} = 3 °C).

Comparison of actual and MLP estimated thermal efficiency of the ORC system for the R417A and R422D working fluids is given in **Figure 6**. As seen in **Figure 6**, if the condenser temperature is increased, the thermal efficiency value decreases. The thermal efficiency values estimated by the MLP model are close to the actual values.

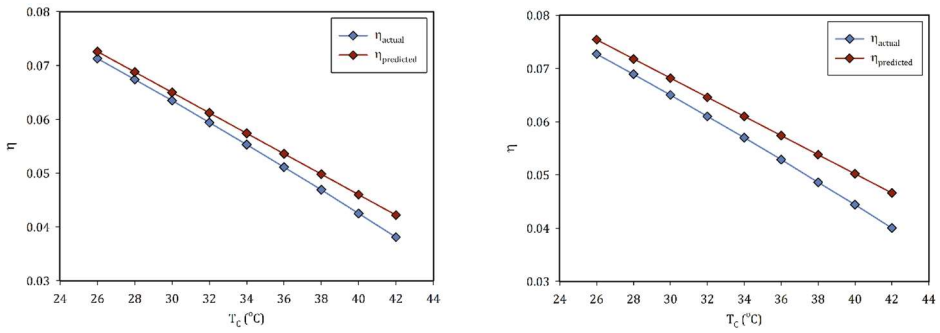

(a) **(b)**

Figure 6. Results comparison of actual thermal efficiency with MLP model results depending on condenser temperature for R417A and R422D. **(a)** R417A (T_E = 61 °C; ΔT_{SH} = 3 °C; ΔT_{SC} = 3 °C); **(b)** R422D (T_E = 61 °C; ΔT_{SH} = 3 °C; ΔT_{SC} = 3 °C).

Tables 5 and **6** compare the actual thermal efficiency of the ORC system using R417A and R422D working fluids with the estimates from the MLP model. The comparison considers the evaporator temperature, condenser temperature, subcooling temperature, and superheating temperature. The maximum percentage errors in thermal efficiency were 2.51% for R417A and 2.37% for R422D.

Table 5. Comparison of actual and model results for R417A.

T_E (°C)	T_C (°C)	ΔT_{SH} (°C)	ΔT_{SC} (°C)	Actual η	Predicted η	Percentage error
61	42	5	5	0.0359	0.0368	–2.51
61	40	7	7	0.0382	0.0388	–1.57
63	30	5	5	0.0655	0.0655	0.00
65	40	3	3	0.0512	0.0512	0.00

Table 5. (*Continued*).

T_E (°C)	T_C (°C)	ΔT_{SH} (°C)	ΔT_{SC} (°C)	Actual η	Predicted η	Percentage error
65	32	5	5	0.0654	0.0654	0.00
67	34	7	7	0.0636	0.0636	0.00
69	34	5	5	0.0691	0.0692	–0.14
69	32	5	5	0.0729	0.0730	–0.14
71	42	7	7	0.0559	0.0556	0.54
73	40	5	5	0.0654	0.0652	0.31
75	34	5	5	0.0797	0.0798	–0.13
75	26	7	7	0.0923	0.0919	0.43
77	28	7	7	0.0920	0.0917	0.33
77	26	3	3	0.0975	0.0968	0.72

Table 6. Comparison of actual and model results for R422D.

T_E (°C)	T_C (°C)	ΔT_{SH} (°C)	ΔT_{SC} (°C)	Actual η	Predicted η	Percentage error
61	42	5	5	0.0379	0.0388	–2.37
61	40	7	7	0.0402	0.0408	–1.49
63	36	7	7	0.0533	0.0534	–0.19
65	40	3	3	0.0531	0.0533	–0.38
67	38	3	3	0.0611	0.0612	–0.16
67	34	7	7	0.0655	0.0657	–0.31
69	38	3	3	0.0650	0.0651	–0.15
69	40	3	3	0.0612	0.0613	–0.16
71	40	3	3	0.0651	0.0652	–0.15
71	30	7	7	0.0802	0.0806	–0.50
75	34	7	7	0.0803	0.0804	–0.12
75	32	3	3	0.0857	0.0860	–0.35
77	34	3	3	0.0856	0.0859	–0.35
77	28	7	7	0.0935	0.0932	0.32

5. Conclusion

This study combined thermodynamic and data mining methods to predict the thermal efficiency of an Organic Rankine Cycle (ORC) system. We evaluated various data mining models, including Linear Regression (LR), Multi-Layer Perceptron (MLP), M5 Rules, M5 Model Tree, Random Committee (RC), and Decision Tree (DT) models. Analyses were conducted for R417A and R422D zeotropic working fluids.

The MLP model emerged as the most effective approach for predicting the thermal efficiency of both R417A and R422D. The MLP's predicted results closely matched the actual results obtained from the thermodynamic model using Genetron software. The Root Mean Square Error (RMSE) for the thermal efficiency was exceptionally low, at 0.0002 for R417A and 0.0003 for R422D. Additionally, the R-squared (R^2) values for thermal efficiency were very high, reaching 0.9999 for R417A

and R422D. While the model exhibited high accuracy, the maximum percentage errors in thermal efficiency were 2.51% for R417A and 2.37% for R422D.

It describes the successful use of data mining for complex engineering tasks, like modeling ORC systems. The newly created model allows for predicting ORC system performance in a simpler, faster, and more accurate way compared to traditional models. As is proved by the results presented in this research, the data mining method can be used to solve many engineering problems. The authors believe this machine learning approach has the potential to be applied to a wide variety of engineering problems in future studies.

Author contributions: Conceptualization, ED and AŞŞ; methodology, ED; software, AŞŞ; validation, ED and AŞŞ; formal analysis, ED; investigation, AŞŞ; data curation, AŞŞ; writing—original draft preparation, ED; writing—review and editing, AŞŞ. All authors have read and agreed to the published version of the manuscript.

Conflict of interest: The authors declare no conflict of interest.

Abbreviations

h	Enthalpy (kJ/kg)
$\dot{m}$	Mass flow rate (kg/s)
$\dot{Q}$	Heat transfer (kW)
T	Temperature (°C)
$\dot{W}$	Power (kW)
η	Efficiency
Δ	Difference
C	Condenser
E	Evaporator
in	Inlet
out	Outlet
p	Pump
r	Working fluid
SC	Subcooling
SH	Superheating
t	Turbine

References

1. Paris IEA. Global Energy Review: CO2 Emissions in 2021. International Energy Agency; 2022.
2. Xu W, Zhao R, Deng S, et al. Is zeotropic working fluid a promising option for organic Rankine cycle: A quantitative evaluation based on literature data. Renewable and Sustainable Energy Reviews. 2021; 148: 111267. doi: 10.1016/j.rser.2021.111267
3. Donti PL, Kolter JZ. Machine Learning for Sustainable Energy Systems. Annual Review of Environment and Resources. 2021; 46(1): 719-747. doi: 10.1146/annurev-environ-020220-061831
4. Arslan O, Yetik O. ANN based optimization of supercritical ORC-Binary geothermal power plant: Simav case study. Applied Thermal Engineering. 2011; 31(17-18): 3922-3928. doi: 10.1016/j.applthermaleng.2011.07.041
5. Yılmaz F, Selbaş R, Şahin AŞ. Efficiency analysis of organic Rankine cycle with internal heat exchanger using neural network. Heat and Mass Transfer. 2015; 52(2): 351-359. doi: 10.1007/s00231-015-1564-9

6. Rashidi MM, Galanis N, Nazari F, et al. Parametric analysis and optimization of regenerative Clausius and organic Rankine cycles with two feedwater heaters using artificial bees colony and artificial neural network. Energy. 2011; 36(9): 5728-5740. doi: 10.1016/j.energy.2011.06.036
7. Kovacı T, Şencan Şahin A, Dikmen E, et al. Performance Estimation of Organic Rankine Cycle by Using Soft Computing Technics. International Journal Of Engineering & Applied Sciences. 2017; 9(3): 1-10. doi: 10.24107/ijeas.297737
8. Massimiani A, Palagi L, Sciubba E, et al. Neural networks for small scale ORC optimization. Energy Procedia. 2017; 129: 34-41. doi: 10.1016/j.egypro.2017.09.174
9. Yang F, Cho H, Zhang H, et al. Artificial neural network (ANN) based prediction and optimization of an organic Rankine cycle (ORC) for diesel engine waste heat recovery. Energy Conversion and Management. 2018; 164: 15-26. doi: 10.1016/j.enconman.2018.02.062
10. Bilgiç HH, Yağlı H, Koç A, et al. Power estimation using artificial neural networks (ANN) in an experimental organic rankine cycle (Turkish). Selcuk University Journal of Engineering, Science and Technology. 2016; 4(1): 7-7. doi: 10.15317/scitech.2016116091
11. Dong S, Zhang Y, He Z, et al. Investigation of Support Vector Machine and Back Propagation Artificial Neural Network for performance prediction of the organic Rankine cycle system. Energy. 2018; 144: 851-864. doi: 10.1016/j.energy.2017.12.094
12. Kılıç B, Arabacı E. Alternative approach in performance analysis of organic rankine cycle (ORC). Environmental Progress & Sustainable Energy. 2018; 38(1): 254-259. doi: 10.1002/ep.12901
13. Luo X, Wang Y, Liang J, et al. Improved correlations for working fluid properties prediction and their application in performance evaluation of sub-critical Organic Rankine Cycle. Energy. 2019; 174: 122-137. doi: 10.1016/j.energy.2019.02.124
14. Palagi L, Pesyridis A, Sciubba E, et al. Machine Learning for the prediction of the dynamic behavior of a small scale ORC system. Energy. 2019; 166: 72-82. doi: 10.1016/j.energy.2018.10.059
15. Huster WR, Schweidtmann AM, Mitsos A. Working fluid selection for organic rankine cycles via deterministic global optimization of design and operation. Optimization and Engineering. 2019; 21(2): 517-536. doi: 10.1007/s11081-019-09454-1
16. Wang W, Deng S, Zhao D, et al. Application of machine learning into organic Rankine cycle for prediction and optimization of thermal and exergy efficiency. Energy Conversion and Management. 2020; 210: 112700. doi: 10.1016/j.enconman.2020.112700
17. Peng Y, Lin X, Liu J, et al. Machine learning prediction of ORC performance based on properties of working fluid. Applied Thermal Engineering. 2021; 195: 117184. doi: 10.1016/j.applthermaleng.2021.117184
18. Tartière T, Astolfi M. A World Overview of the Organic Rankine Cycle Market. Energy Procedia. 2017; 129: 2-9. doi: 10.1016/j.egypro.2017.09.159
19. Cengel YA, Boles MA, Kanoğlu M. Thermodynamics: an engineering approach. McGraw-hill New York; 2011.
20. Kong R, Deethayat T, Asanakham A, et al. Thermodynamic performance analysis of a R245fa organic Rankine cycle (ORC) with different kinds of heat sources at evaporator. Case Studies in Thermal Engineering. 2019; 13: 100385. doi: 10.1016/j.csite.2018.100385
21. Siraj F, Ali M. Mining Enrollment Data Using Descriptive and Predictive Approaches. Knowledge-Oriented Applications in Data Mining. Published online January 21, 2011. doi: 10.5772/14210
22. Becerra-Fernandez I, Zanakis SH, Walczak S. Knowledge discovery techniques for predicting country investment risk. Comput Ind Eng. 2002; 43: 787-800. doi: 10.1016/S0360-8352(02)00140-7
23. Kaluža B. Machine Learning in Java. UK Packt Publ Ltd; 2016.
24. Chapman P, Clinton J, Kerber R, et al. CRISP-DM 1.0: Step-by-step data mining guide. SPSS inc. 2000; 9: 1-73.
25. Şencan A. Modeling of thermodynamic properties of refrigerant/absorbent couples using data mining process. Energy Conversion and Management. 2007; 48(2): 470-480. doi: 10.1016/j.enconman.2006.06.018
26. Witten IH, Frank E, Hall MA. Implementations. Data Mining: Practical Machine Learning Tools and Techniques. Published online 2011: 191-304. doi: 10.1016/b978-0-12-374856-0.00006-7
27. Shaghaghi A, Omidifar R, Zahedi R, et al. Proposing a new optimized forecasting model for the failure rate of power distribution network thermal equipment for educational centers. Thermal Science and Engineering. 2023; 6(2): 2087. doi: 10.24294/tse.v6i2.2087

28. Niranjan A, Prakash A, Veena N, et al. EBJRV: An Ensemble of Bagging, J48 and Random Committee by Voting for Efficient Classification of Intrusions. 2017 IEEE International WIE Conference on Electrical and Computer Engineering (WIECON-ECE). Published online December 2017. doi: 10.1109/wiecon-ece.2017.8468876
29. Şencan A, Kızılkan Ö, Bezir NÇ, et al. Different methods for modeling absorption heat transformer powered by solar pond. Energy Conversion and Management. 2007; 48(3): 724-735. doi: 10.1016/j.enconman.2006.09.013
30. Kaboli SHrA, Fallahpour A, Selvaraj J, et al. Long-term electrical energy consumption formulating and forecasting via optimized gene expression programming. Energy. 2017; 126: 144-164. doi: 10.1016/j.energy.2017.03.009

Thermal Science and Engineering 2024, 7(1), 6054.
https://doi.org/10.24294/tse.v7i1.6054

Article

A study on fire risk and its mitigation in gravure printing press

Madhab Chandra Jena*, Sarat Kumar Mishra, Himanshu Sekhar Moharana

Department of Mechanical Engineering, BPUT, Rourkela, Odisha 769004, India
*** Corresponding author:** Madhab Chandra Jena, madhab_jena@rediffmail.com

CITATION

Jena MC, Mishra SK, Moharana HS. A study on fire risk and its mitigation in gravure printing press. Thermal Science and Engineering. 2024; 7(1): 6054.
https://doi.org/10.24294/tse.v7i1.6054

ARTICLE INFO

Received: 20 December 2023
Accepted: 6 February 2024
Available online: 13 February 2024

Abstract: The gravure printing process is widely utilized for large-scale, high-quality, multi-colored printing tasks executed at high press speeds. This includes a diverse range of products such as art books, greeting cards, currency, stamps, wallpaper, magazines, and more. This thesis addresses the fire risks associated with gravure printing, acknowledging the use of highly flammable materials and the potential for static charge-related incidents. Despite its prevalence, there is limited research on fire prevention and control in gravure printing. The study employs field observations, stakeholder interviews, and an extensive review of literature on fire risk and control in printing press operations in India. It analyzes the causes of fires using the fire triangle model, emphasizing the role of heat, combustible materials, and oxygen in fire incidents within the printing press environment. The thesis categorizes preventive measures into fire prevention and fire suppression actions, focusing on reducing fire load, static charge mitigation, and implementing firefighting systems. It observes that poor housekeeping, lack of awareness, and inadequate emergency control plans contribute significantly to fire hazards in press facilities. Additionally, the research identifies key factors such as high press temperatures, low humidity, improper storage, and inadequacies in firefighting systems as potential causes of fires. It emphasizes the need for optimal environmental conditions, proper storage practices, and effective firefighting infrastructure within press facilities. The study concludes with comprehensive guidelines for loss prevention and control, including management programs, housekeeping, operator training, pre-emergency planning, preventive maintenance, and plant security. It also addresses safety measures specific to gravure printing presses, such as automatic sprinkler systems, fire hydrant system, carbon dioxide flooding systems, and portable fire extinguishers. In summary, this thesis provides valuable insights into the multifaceted nature of fire risks in gravure printing presses and recommends a holistic approach for effective fire prevention and control.

Keywords: gravure printing; fire risk; risk mitigation and control; corrective and preventive actions

1. Introduction

The gravure printing process is employed for large-scale, high-quality, and multi-colored printing tasks conducted at elevated press speeds, encompassing a diverse array of products such as art books, greeting cards, advertising materials, currency, stamps, wallpaper, wrapping paper, magazines, wood laminates, and rubber or plastic substrates. In gravure printing, a rotating printing plate or cylinder immersed in an ink bath features recessed cells that are etched or engraved to varying depths and sizes. A doctor blade removes excess ink, and the remaining ink in the recessed cells transfers the image to the paper [1]. Capillary action of the substrate, along with pressure from impression rollers, draws the ink out of the cell cavity and onto the substrate as shown in **Figure 1**.

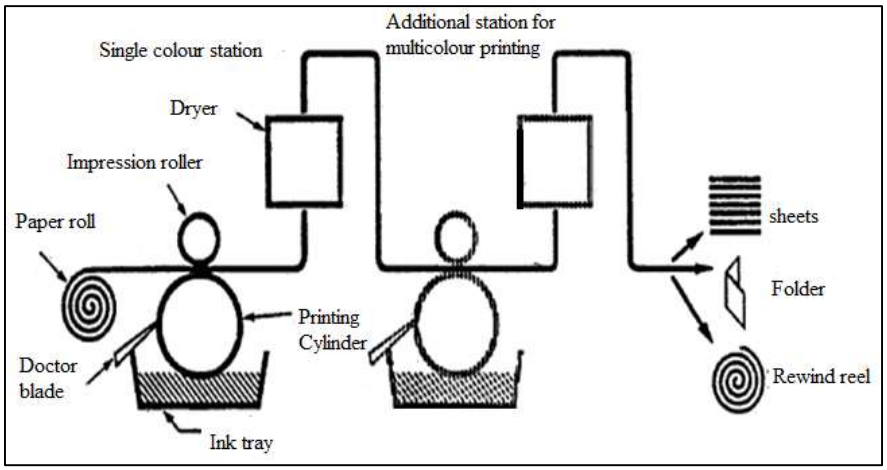

Figure 1. Gravure printing process.

Typically, cylinders for gravure printing are constructed from steel and plated with copper, featuring a light-sensitive coating. While most cylinders are now engraved using laser technology, some are still engraved using a diamond stylus or a chemical etch. Before etching, a resist in the form of a negative image is applied to the cylinder to protect non-image areas from the etching chemical. Following etching, the resist is stripped off, a process akin to manufacturing printed circuit boards. The engraved cylinder undergoes proofing, testing, potential reworking, and is finally chrome plated. Corrections and touch-ups may still be performed using traditional methods [2].

Gravure presses come in flat and rotary types, with rotogravure presses operating at speeds up to 610 m/min and webs as wide as 3.1 m used in publication plants. Larger webs, up to 3.8 m wide, are employed for floor covering, while presses for packaging materials usually have smaller webs (1–1.5 m wide) with up to eight printing units.

Solvent-based inks are commonly used in gravure printing as processes using solvent inks can run faster as these inks dry more quickly.

The gravure printing press poses an increased risk of fire due to the use of highly flammable materials such as solvents and inks with very low flash points. The substrates used for printing, such as paper or polymer film, are also combustible. The press area is filled with volatile organic compounds (VOCs), specifically solvent vapor, which is highly prone to ignition [3–6].

The friction between the substrate and printing or guiding rollers generates a substantial amount of static charge. The accumulation of high static charge can lead to sparks, becoming a potential cause of fire in the press area. Even a small spark, arising from static charge or friction between surface contacts of moving press parts, can trigger an instantaneous and devastating fire, particularly in an environment conducive [6].

Fires in gravure printing presses are a recurrent and widespread occurrence, leading to significant property damage and, tragically, human casualties worldwide. Despite the prevalence of these incidents, there has been a noticeable lack of prior research focused on fire prevention and control specific to gravure printing presses some papers cited on environmentally friendly printing processes [7]. This research endeavors to fill this gap by conducting a comprehensive field study and survey

involving printing presses and relevant stakeholders. The aim is to amalgamate valuable insights and knowledge to enhance the control and prevention of fire risks associated with gravure printing presses.

2. Materials and method

This research is conducted through a combination of field observations, interviews with key stakeholders involved in the operation and control of gravure printing presses in India, and a comprehensive review of literature, including case studies on fire incidents and control in printing press environments.

3. Cause of fire in printing press through fire triangle analysis

In the intricate dynamics of the fire triangle, the confluence of three pivotal elements—heat, combustible material, and oxygen—serves as the catalyst for the ignition of a fire. This phenomenon unfolds as a natural consequence when these elemental forces come together in harmonious synergy. In the specialized realm of a gravure printing press, the perpetual presence of two fundamental elements, namely oxygen and combustible material, forms the foundational backdrop. Oxygen is omnipresent in the atmosphere inside the printing press and combustible materials like paper used as printing substrate, inks, solvents etc. are used for printing process. Only the third element that is heat is not present all the time, it is generated from the abnormal operation in the press and once it is generated it is difficult to prevent the occurrence of fire in the printing press, hence it is the focus of debate in this thesis.

Fires within the press are frequently instigated by the introduction of the third elemental player, heat, which emanates from a spectrum of diverse processes. The genesis of this heat can be traced back to the frictional interplay between moving parts or the generation of sparks arising from a static charge—a phenomenon that manifests with notable frequency. This static charge materializes due to the friction between metallic rollers and a swiftly moving substrate during the press operation, creating an environment ripe for the occurrence of fires [8].

Adding to the intricate tapestry of potential ignition sources, the incorporation of solvents in the printing ink amplifies the risk. These solvents introduce volatile organic compounds into the normal atmospheric conditions, establishing an environment that is remarkably conducive to the initiation and swift progression of fires. The volatile nature of these compounds, combined with the inherent conditions of high-speed press operations, elevates the vulnerability of the printing press to fire incidents, underscoring the critical importance of vigilant safety measures in this complex industrial setting. The aim should be always to reduce the fire load, reduce the static charge as much as possible, drive out the solvent vapors from the press area, reduce the friction between moving parts etc.

4. Observation of fire risks during field study

The field study on fire risks during press visits across various regions in the country revealed several critical observations that contribute to the causes of fires in press facilities. Among these observations, poor housekeeping practices were

identified as a significant factor, emphasizing the importance of maintaining a clean and organized workspace to prevent fire hazards. The lack of awareness among personnel was also noted as a contributing factor, highlighting the need for comprehensive training programs to educate individuals on fire safety protocols.

Additionally, the study identified inadequacies in emergency control plans, emphasizing the importance of having robust and well-defined procedures to handle fire incidents promptly. Improper preventive maintenance practices, such as neglecting equipment upkeep, were identified as another potential cause, stressing the need for regular maintenance schedules to mitigate fire risks. The inadequacy of vapor extraction systems and static charge neutralizers were recognized as potential contributors, underscoring the importance of implementing effective ventilation and static control measures. Other notable factors included high press temperatures, low relative humidity in press areas, improper segregation of fire loads, absence of fire doors, and inadequacies in firefighting systems [9]. These findings emphasize the necessity of maintaining optimal environmental conditions, proper storage practices, and ensuring the presence of effective firefighting infrastructure within press facilities [10].

The study also highlighted the risks associated with the use of sparking tools in the press area for cleaning and maintenance activities. This emphasizes the need for implementing safer alternatives and ensuring that personnel are trained to use tools that do not pose a fire hazard. Finally, the improper monitoring of critical parameters like temperature inside the press room, humidity inside the press room, level of static charge generated from the printing operation, level of volatile organic compounds (VOC), etc. related to fire in the press area was identified as a potential issue, indicating the importance of implementing robust monitoring systems to detect and address fire risks promptly. Overall, the field study provided valuable insights into the multifaceted nature of fire risks in press facilities, calling for a comprehensive approach to mitigate these risks effectively.

5. Prevention and control measures

The guidelines for loss prevention and control provided here are not exhaustive and were crafted with an average hazard level in mind. Elevated hazard levels necessitate additional loss prevention and control measures.

5.1. Management programs

Implementing robust management programs is essential for effective fire prevention and control. These programs should include:

Housekeeping: Poor housekeeping leads to mixing of material and accumulation of combustible material in unwanted places which may be a biggest reason of fire spread once it is initiated for any reason. Vigilantly manage the accumulation of paper, plastic waste, ink residue, and starch dust within the facility. For instances of excessive dust generation, consider installing automatic and properly protected dust collection equipment to mitigate potential fire hazards.

Operator training program: Ensure that all operators are thoroughly educated on the hazards inherent in their tasks and are well-versed in the operation of safety control

equipment. Strictly prohibit any deviations from established written procedures to maintain a consistent and safe working environment.

Pre-emergency planning: Develop and consistently update a comprehensive pre-emergency plan that clearly defines all aspects of emergency response and business continuity. This plan should serve as an indispensable tool to guide the facility's response in the event of a fire or other emergencies. Regular overviews of the plan can aid in customizing emergency response strategies based on the specific characteristics of the facility.

Preventive maintenance and inspection program: Establish a proactive preventive maintenance and inspection program, ensuring the availability of spare parts for key equipment with high attrition rates. This approach facilitates seamless repairs and maintenance, allowing the plant to operate at full capacity. Incorporate modern inspection techniques, such as nondestructive testing, infrared scanning, and vibration analysis, to assess and maintain process equipment. Keep an inventory of spare parts on-site for components like gears, rolls, and bearings that may wear and require replacement.

Plant security and surveillance: Safeguard the facility by restricting access through secure fencing, complemented by guards stationed at all points of entry. Implement recorded watchman services in areas that are not under constant supervision to enhance overall security. Additionally, manage other management programs, including those related to welding, cutting, and “hot work” permits, as well as smoking regulations, to maintain a safe working environment.

5.2. Other miscellaneous safety measures

In the realm of web-fed rotary press machines, many utilize automatic paper splicing for feeding successive rolls. However, caution is advised as less number of rolls of paper may be present near the machine.

Printing presses, especially high-speed multicolor machines, pose a substantial mechanical risk. The electric power-supply equipment for these presses may be unique, and specific attention must be given to solvent recovery equipment, which involves exposures to pressure vessels.

For water-cooled presses, implement water flow supervision configured to alarm and shut down operations during cooling water failure. Recommendations may be tailored based on the types of inks and solvents handled, the nature of the occupancy near the press, and the level of protection provided.

Limiting the number of presses in one area, considering both value and production exposure, is advised. The press room should be safeguarded with an approved automatic wet-pipe sprinkler system. Install sprinklers not only in the press area but also in the control room, ink storage room, ink mixing room, and any concealed spaces shielded from ceiling sprinkler discharge. Design the sprinkler system in accordance with NFPA (national fire protection association) 13 and PRC.12.1.1.0, classifying it as Extra Hazard Group 1 for inks with a flash point less than or equal to 37.8 ℃ [11–13]. In congested press areas, consider enhancing protection with a foam-water sprinkler system.

For presses using inks with a flash point less than or equal to 37.8 ℃, implement

an automatic fixed-pipe carbon dioxide extinguishing system with a connected reserve, following NFPA 12 and PRC.13.3.1 [13]. Design the system to cover all parts of the press, including ink reservoirs. Use rate-of-rise, rate-compensated detectors for automatic operation, and provide a connected-reserve carbon dioxide supply with a remote manual release. Wherever possible water-based inks should be used.

In cases where local application carbon dioxide protection systems are installed on large press assemblies, arrange them to operate independently based on printing press spacing so that the local fire can be put off by partial CO_2 flooding without hampering the whole press operation. Upon system activation, an alarm should sound, initiating a complete shutdown of the press. This shutdown should include ventilation fans, drive motors, ink pumps, dryers, and damper closure. Extend the carbon dioxide system to include exhaust ductwork, dryers, connecting ductwork, ink mixing and storage rooms, and the control room. Strategically place carbon dioxide hose reels for additional coverage.

Certain newer press configurations, accommodating double-width sheets or featuring vertical stacking of multicolor units, present challenges for conventional protection piping. Address these challenges by adapting protection measures accordingly.

For presses using inks with a flash point greater than 37.8 ℃, deploy automatic sprinklers for areas shielded from overhead sprinkler protection. Additionally, install sprinklers below platforms and in roll paper reel-transfer areas beneath the presses.

Ensure the press room is equipped with adequate portable class B and C fire extinguishers following NFPA 10, strategically placed throughout the area [13].

To maintain a safe working environment, take proactive measures to minimize ink mist and dust accumulation in the press area and exhaust ducts. Prevent the accumulation of paper scraps, flammable liquids, and cleaning rags. Regularly lubricate all rotating equipment to reduce heat buildup caused by excess friction.

5.3. Fire prevention through electrical installation and control

Ensure the proper installation of equipment in compliance with NFPA 70 standards [13]. Manage large concentrations of cables by placing them in conduit or protecting them with an approved fire-retardant coating.

For operations involving flammable inks, take the following protective measures:

Given that printing presses are potential generators of static electricity, it is crucial to eliminate static charges that may accumulate and reach levels capable of igniting flammable vapor [14,15].

Ground the entire press framework electrically. Outfit the full width of the web, especially at the delivery side of each impression roller, and select points on the press with high-voltage static eliminators or neutralizers to eliminate nuisance static. Note that some static eliminators use radioactive materials that ionize the air. Electrostatic assist must be avoided in metallic colors.

Humidification proves to be an effective method for controlling static electricity, especially in high-speed printing environments. If employed, maintain a relative humidity level between 45% and 60%.

For drying inks, prefer indirect heating methods. Locate heat sources, such as

electrical elements or direct/indirect gas or oil-fired heat exchangers, at least 6.1 m horizontally and 2.4 m vertically from the ink troughs where practical. To minimize the intake of flammable vapor into the combustion chamber, consider placing the dryer burner in the air intake.

Implement a system of combustion safeguard controls and ventilation for dryers, following NFPA 86 guidelines [16,17]. The ventilation system and associated ductwork should prevent vapor accumulation above 25% of their lower explosive limit.

Include safety interlocks to automatically shut down the ink pumping system in case of press ventilation system failure. When a vapor detection system using listed equipment is installed, ventilation requirements may be reduced. Set the system to sound an alarm at approximately 25% and shut down the press at around 50% of the lower explosive limit of the solvent.

In cases where flammable inks are used, there is a potential for explosions. Address the fume issue through one of three methods: direct exhaust, a solvent recovery system, or catalytic fume incineration. The use of direct exhaust is diminishing due to material costs and stricter environmental guidelines, with catalytic fume incinerators gaining popularity. Refer to NFPA 86 for protection guidelines related to these incinerators [17].

Improper handling of fumes poses an explosion risk, which could lead to severe secondary dust explosions. These explosions may result from accumulations of starch and paper dust on structural members and improperly cleaned equipment.

5.4. Preventive measures during press room construction

When constructing press rooms, take preventive measures to enhance safety:

1) Press location: Place presses that use highly flammable inks in a separate building or an aboveground room with a 0.14–0.21 bar explosion-resistant wall, having a minimum fire-resistance rating of two hours. Situate this room on at least one outside wall to facilitate explosion relief. Implement explosion venting as per NFPA 68 guidelines [17].
2) Floor construction: Construct the press room floor using non-sparking, conductive concrete, with sufficient pitch for effective drainage of flammable liquids. If there is a floor above the pressroom, ensure it is liquid-tight.
3) Ventilation: Provide continuous ventilation, not less than 0.305 $m^3/min/m^2$ of floor, to remove solvent vapor directly from solvent-wetted surfaces of presses, even when they are not in operation to reduce VOC level inside the press area which leads to lowering the fire risk. Install a separate room ventilation system along the floor, particularly under ink fountains and color pans, to eliminate flammable vapor-air mixtures. Locate suction pickups within 152 mm of the floor. Avoid concealed spaces, but, if necessary, ensure continuous venting to prevent solvent vapor accumulation. Install noncombustible draft curtains, at least 1.2 m deep, between presses to limit the number of operating sprinkler heads.
4) Storage and transfer of flammable inks and solvents: In any printing operation, select inks based on paper stock and printing process. All inks consist of pigment,

resin, solvent, and additives. Gravure inks, resembling paint, contain resin, coloring agent, and solvent with flash point temperatures of 6.7–49 °C, making them class I flammable liquids.

Storage: Store, mix, and dispense flammable inks and solvents in a suitably protected flammable-liquid storage room or a detached building following NFPA 30 standards [17].

Quantity limitations: Limit ink supply in the press area to no more than a workday's worth. Retain one shift's supply in the press area stored in an approved vented cabinet. Position cabinets at least 3.0 m away from presses.

Tank systems: Design piping systems for tanks with appropriate materials, routing, and valving. Evaluate ink transfer methods. Install automatic ink supply systems with safety shutoff valves or positive displacement pumps that activate upon automatic sprinkler, special extinguishing system, or vapor detection operation.

5) Cleaning practices: Use safety solvents for cleaning presses. When cleaning hot surfaces, employ a liquid with a flash point at least 14 °C above the surface temperature. Always use non-sparking tools for cleaning and maintenance activities.

6. Conclusion

This thesis addresses the pressing issue of fire risks in gravure printing processes. Despite the widespread occurrence of fire incidents and the inherent dangers of highly flammable materials, there has been a noticeable lack of dedicated research in this area. The research, conducted through field studies and stakeholder interviews in India, employs the fire triangle model to identify critical factors contributing to fires in printing presses. Preventive measures, categorized into fire prevention and suppression actions, are highlighted, focusing on reducing fire load, mitigating static charge, and implementing firefighting systems. The field study emphasizes poor housekeeping, lack of awareness, and inadequate emergency control plans as significant contributors to fire hazards. Key risk factors, including high press temperatures, low humidity, and deficiencies in firefighting systems, are identified. The thesis concludes with comprehensive guidelines for loss prevention, encompassing management programs, operator training, pre-emergency planning, preventive maintenance, and safety measures specific to gravure printing presses.

In essence, this research provides valuable insights into the multifaceted nature of fire risks in gravure printing presses and advocates a holistic approach to effective fire prevention and control. The recommendations aim to enhance safety protocols and practices, contributing to the mitigation of fire risks in these critical manufacturing environments. Future scope of study would be a details analysis of the factors which are the root cause of fire and preventive actions derived from the root cause to protect the gravure printing press from fire risk.

Author contributions: Conceptualization, methodology, software, validation, formal analysis, investigation, resources, writing—original draft preparation, writing—review and editing, MCJ; data curation, visualization, supervision, SKM; project

administration; funding acquisition, HSM. All authors have read and agreed to the published version of the manuscript.

Conflict of interest: The authors declare no conflict of interest.

References

1. Available online: https://axaxl.com/-/media/axaxl/files/pdfs/prc-guidelines/prc-17/prc17181printingpressoperationsv1.pdf (accessed on 7 December 2023).
2. Sharma B, Singh S, Pandey A, et al. Sustainable and green manufacturing of gravure printing cylinder for flexible packaging printing application. Scientific Reports. 2022; 12(1). doi: 10.1038/s41598-022-15893-1
3. Aydemir C, Özsoy SA. Environmental impact of printing inks and printing process. Journal of Graphic Engineering and Design. 2020; 11(2): 11-17. doi: 10.24867/jged-2020-2-011
4. Guo X, Shen Y, Liu W, et al. Estimation and Prediction of Industrial VOC Emissions in Hebei Province, China. Atmosphere. 2021; 12(5): 530. doi: 10.3390/atmos12050530
5. Hamer IAH. Technological development of water-based packaging inks for gravure printing. Pigment & Resin Technology. 1998; 27(2): 99-101. doi: 10.1108/03699429810693489
6. Hansuebsai A, Kaosod A, Kanchanasing T. A new environmental performance index based on the carbon footprint, VOC emissions, and waste in a printing house. Engineering Reports. 2020; 2(5). doi: 10.1002/eng2.12165
7. Ma X, Yang L, Wu H. Removal of volatile organic compounds from the coal-fired flue gas by adsorption on activated carbon. Journal of Cleaner Production. 2021; 302: 126925. doi: 10.1016/j.jclepro.2021.126925
8. Sharma B, Singh S, Pandey A, et al. Studies on Mitigation of Printing Cost, Volatile Organic Compounds Emission and Sustainability in Printing Industries by Using Water-based Inks. Published online November 30, 2021. doi: 10.21203/rs.3.rs-1063982/v1
9. Available online: https://www.kirinoikeuchi.co.jp/eng/technology/ct60.php (accessed on 7 December 2023).
10. Available online: https://www.hse.gov.uk/printing/fire-explosion.htm (accessed on 7 December 2023).
11. Available online: https://www.shippai.org/fkd/en/cfen/CC1000199.html- (accessed on 7 December 2023).
12. Ramirez JCC, Tumolva TP. Analysis and optimization of water-based printing ink formulations for polyethylene films. Applied Adhesion Science. 2018; 6(1). doi: 10.1186/s40563-017-0102-z
13. Fire risk during gravure printing. Available online: https://meech.com/application/fire-risk-during-gravure-printing/#:~:text=The%20use%20of%20combustible%20solvents,source%2C%20igniting%20the%20solvent%20gases. (accessed on 7 December 2023).
14. Available online: https://risklogic.com/fire-protection-at-printing-plants/ (accessed on 7 December 2023).
15. Available online: https://www.rycobel.com/optimization/solutions-for-static-electricity/static-electricity-applications/static-electricity-in-rotogravure-printing (accessed on 7 December 2023).
16. Sharma B, Sauraj S, Kumar B, et al. Synthesis of waterborne acrylic copolymer resin as a binding agent for the development of water-based inks in the printing application. Polymer Engineering & Science. 2021; 61(5): 1569-1580. doi: 10.1002/pen.25681
17. Available online: https://www.nfpa.org/about-nfpa (accessed on 7 December 2023).

Thermal Science and Engineering 2024, 7(1), 7906.
https://doi.org/10.24294/tse.v7i1.7906

Article

Enhancement of solar panel power generation performance with a passive sun tracking system

Guoyang Song[1], Defa Han[2], Yingge Li[1,2], Zhaoming He[3], Dongxing Du[1,*]

[1] Geo-Energy Research Institute, College of Electromechanical Engineering, Qingdao University of Science and Technology, Qingdao 266100, China
[2] College of Automation and Electronic Engineering, Qingdao University of Science and Technology, Qingdao 266100, China
[3] Department of Mechanical Engineering, Texas Tech University, Lubbock TX 79409, USA
*** Corresponding author:** Dongxing Du, du-dongxing@qust.edu.cn

CITATION

Song G, Han D, Li Y, et al. Enhancement of solar panel power generation performance with a passive sun tracking system. Thermal Science and Engineering. 2024; 7(1): 7906. https://doi.org/10.24294/tse.v7i1.7906

ARTICLE INFO

Received: 12 February 2024
Accepted: 9 March 2024
Available online: 20 March 2024

Abstract: In this paper, we design and fabricate a solar tracking device that can continuously track the sun by adjusting the direction and angle of the solar panel in real time, thereby improving the power generation efficiency of the solar panel. The mechanical parts as well as the automatic control part of the passive sun-tracking system are described, and the efficiency enhancement with the sun-tracking solar panel is characterized in comparison with the fixed panel system. The test results show that in the spring season in Qingdao city of eastern China, the sun-tracking system can improve the solar cell power generation efficiency by 28.5%–42.9% when compared to the direction and elevation angle fixed system in sunny days. Even on partly cloudy days, the PV power output can increase by 37% with the passive sun-tracking system. Economic analysis results show the cost-benefit period is about 10 years, which indicates that the passive sun tracking device can substantially contribute to the solar energy harvest practices.

Keywords: solar cell panel; passive sun-tracking system; design; fabrication; power generation efficiency

1. Introduction

Global population growth and economic development have led to a continuous increase in energy demand. Accompanying the rapid growth of energy consumption, the CO_2 concentration in the atmosphere has increased from 300 ppm before the industrial revolution to the current 410 ppm [1], and climate change has arisen as a major concern of the human society. The technologies on reducing and controlling the greenhouse gas emissions, therefore, have become one of the most attractive research aspects in recent years [2–11]. Many countries are accelerating the development and utilization of clean energy to reduce their dependence on fossil fuels to achieve the lower greenhouse gas emission goals. Under such circumstances, solar photovoltaic (PV) energy, which stands as one of the most prominent alternatives in emerging clean energies, has been quickly developed. Abundantly and widely distributed in almost all the world regions, clean and renewable solar power is expected to become an economically viable energy choice when compared to the traditional fossil fuel-based electricity generation industry [12–22].

With the development of solar energy technology and the realization of economies of scale, the cost of solar power generation continues to decrease. At present most solar panel systems are fixed installations on home roofs and other locations [23–25]. Due to the fixed orientation, these solar panels have a power

generation efficiency as low as 7% [26]. To enhance the efficiency of solar panels, solar tracking concept was proposed to keep the solar panels always aligned with the sun, therefore to achieve maximal efficiency and power generation [27]. In general, solar tracking can be accomplished through two methods: 1) single-axis solar tracking systems, and 2) dual-axis solar tracking systems [28,29]. The dual-axis solar tracking systems has shown obvious superiors to the single-axis systems on energy collection efficiency as well as on the system adaptability to various geographical and climatic conditions.

Dual-axis systems allow solar panels to adjust in two directions (horizontal and vertical), thus enabling precise tracking of the sun's position to maintain optimal perpendicular alignment with sunlight throughout the day, and maximizing electricity generation efficiency. Mpodi et al. [30] reviewed studies concerning the dual-axis photovoltaic tracking systems and reported the dual-axis system can increase electricity generation by 30%–40% and by adjusting angles, dual-axis systems mitigate shading effects from nearby buildings or obstacles. Josely Jose et al. [31] produced a small scale automated solar ray tracking device, and studied solar radiation and PV parameters using spectral, PV panel and LDR (Light Dependent Resistor) sensors characterization techniques. Their results indicated the maximum energy can be achieved with the solar tracking system. Zaghba et al. [32] conducted simulation and experimental assessment works concerning the outdoor performance of the PV systems in a 11.28 kWp grid, and reported that the dual-axis solar tracking system could achieve the greatest performance improvement of 20.89%. They further compared the mitigation amount of CO_2 among three installation managements of the stationary PV system, one axis PV system, and the dual-axis tracking PV systems, and reported the largest value of 5.85 tons in dual-axis system against 4.84 tons and 5.46 tons in other two systems. Mamodiya and Tiwari [28] constructed a closed-loop real-life solar tracking system consisting of a mechanical and electrical system based on the Simulink and Solidworks platform, and reported the sufficient strength as well as the enhanced effectiveness of the solar PV system. Muthukumar et al. [33] proposed a dual-axis solar track system and monitored the energy output data in 24 h at the interval of 0.2 s to validate the robustness of the system. They concluded the dual-axis system is an effective but inexpensive way to improve the solar energy output efficiency.

On the other hand, although solar tracking systems can improve the power generation efficiency, the power consumption associated with the solar tracking motion will increase by at least 20% to 30% compared to fixed solar panel arrangements [34]. Awasthi et al. [35] discussed various types of solar photovoltaic systems and solar tracking systems, focusing on recent advancements in dual-axis tracking system design and performance. They pointed out the drawbacks of dual-axis solar systems, such as expensive sensor costs and structural complexity. To address these negative issues, Boukdir and EL Omari [36] designed a novel dual-axis system with three LDR sensors, two LDRs for the azimuthal tracking while the other one for the elevation tracking, to achieve the high precision tracking operation. They tried to balance between sun tracking precision and cost, however their system still require improvements to cope with the adverse weather conditions. Palomino-Resendiz et al. [37] introduced a Model Predictive Controller (MPC) to the two-axis

solar tracing system, and performed numerical and experimental validation works on the improved performance on energy consumption during the solar tracker operation. Their results showed the MPC could reduce the energy consumption of 90% average however at higher tracking error. Lu and Ajay [38] proposed a novel solar sensor based sun tracking system to balance the precise tracking movements and the PV energy production. They developed a Proportional-Integral-Derivative (PID) controller and employed Algorithm Optimization (AO) to minimize the energy cost in panel movement and thus increase the system capacity on the solar energy harvesting. Anshory et al. [39] utilized ESP8266 microcontroller to control the PV panel movement following the sunlight information from a LDR sensor. Based on the measurement data of current, voltage and temperature, they concluded their new design could increase the system response sensitivity, panel movement accuracy, and the energy harvest efficiency in comparison to the manual control system. Based on above literature review works, it is found there is still a current need for the dual-axis sun tracking systems to achieve high efficiency on sun power harvest practices at the base of low power consumption and simple structure.

In this paper, we designed and fabricated a passive dual-axis solar tracking system based on the LDR sensor. The LDR receives and transits the sun light signals to guide the low power motor to drive the solar panel in two ways, rotating and tilting, to accurately track the position of the sun. The two-way movement ensures that the solar panel could always be oriented toward the direction of maximum light intensity and therefore maximize its power generation efficiency. With the fabricated passive sun tracking system, we tested the power generation characteristics of sun-tracking solar panels under different weather conditions in the spring season in eastern China based on daily power generation records. To show the advantage of the passive sun-tracking system, we measured in comparison the power output of the fixed panel system and carried out economic analysis.

Accordingly, the paper is organized in the following sequences. In Chapter 2, the detailed descriptions on the mechanical parts as well as the control and measurement parts of the passive sun-tracking system were provided. In chapter 3, the sensitivity of the constructed apparatus was validated at the first place, then the measurements were performed in both sunny days and partly cloudy days to show the advantages of the sun tracking system over the fixed panel system in terms of the instantaneous power output and the cumulative daily power generation, furthermore economic advantages of the passive sun-tracking system were discussed by comparing with other reported systems with the similar functions. At last, the conclusions were presented in Chapter 4.

2. Passive sun tracking solar panel system

2.1. Mechanical parts

The solar cell panel employed in this study is a monocrystalline silicon panel with a specification size of 1500 × 640 mm and a maximum output power of 110 W.

The physical installation diagram of the sun tracking device is shown in **Figure 1**. In accordance with the mechanical design requirements [40–42], the passive sun tracking system consists of the following mechanical structures: rotary support,

rotary bearing, solar panel support, base support, and screw rod slider module. The support parts of the tracking system are made of European standard 30 × 30 aluminum alloy, with high strength and hardness but a relatively small density, which reduces the load on movement of the device. The threaded rod support plate uses a Q235-A steel plate with a thickness of 5 mm to improve the process scheme, ensuring its mechanical properties and assembly accuracy. The bearing part, on the other hand, employs slewing bearings that enable extensive rotation within confined spaces thus ensuring stability throughout the rotational process. Most importantly, these bearings exhibit lower energy requirements for rotational motion, thus could achieve overall energy savings on the mechanical movement of the sun-tracking system.

The detailed force analysis on the mechanical part of the dual-axis sun tracking system, which validates the strength as well as the stability of the system, is provided in section 3.1.

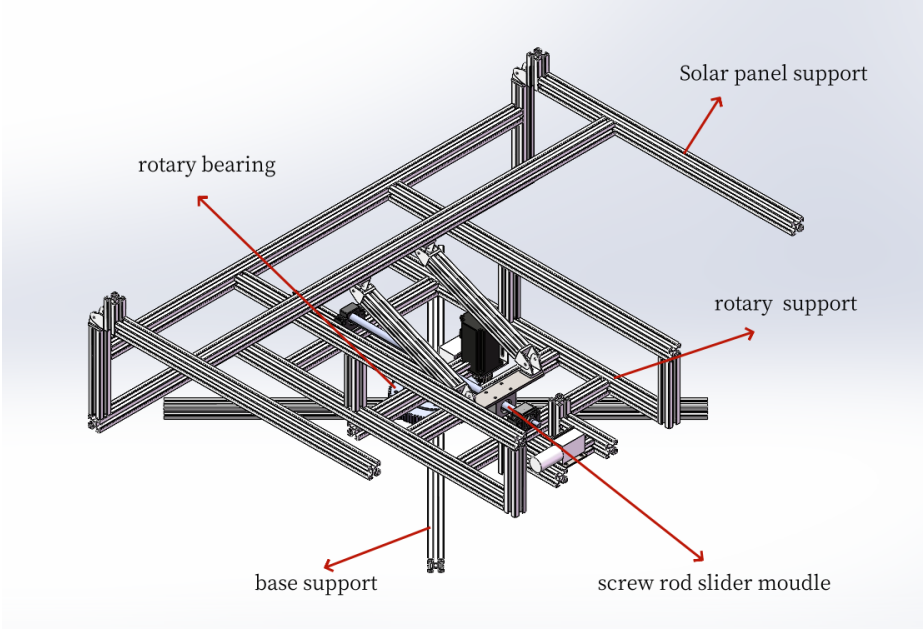

Figure 1. The mechanical parts installation diagram of the sun tracking system.

2.2. Control and measurement parts

The control and power output data collection parts incorporated in the physical system are depicted in **Figure 2**. As shown in the figure, the key parts of the automatic sun tracking system consist of an LDR sensor and a controller. The LDR sensor, which consists of two layer eight micro light sensors, converts the intensity of light into voltage and transmits the position information of the sun to the controller. The controller processes and analyzes the signals from the LDR sensor to determine the intensity and direction of sunlight. Then, the controller drives the worm gear reducer motor to turn the sun power panel until the panel aims exactly at the sun. The power consumption of the controller system is less than 5 W and can be well covered by the power generated by the sun panel, which means that as long as the system is set in sunlight circumstances, the controller would have enough power supply to operate automatically without an external power supply. The worm gear reducer motor functions at the rated voltage of 12 V and the maximum current of 3

A with a reduction ratio of 634 and is powered by the solar panel through the current regulator module. Under an unloaded speed of 3 r/min, the motor has an unloaded current of 0.1 A, while under a loaded speed of 2 r/min, the motor has a current of 0.9 A at a rated power of 10.8 W and a rated torque of 1.47 N · m.

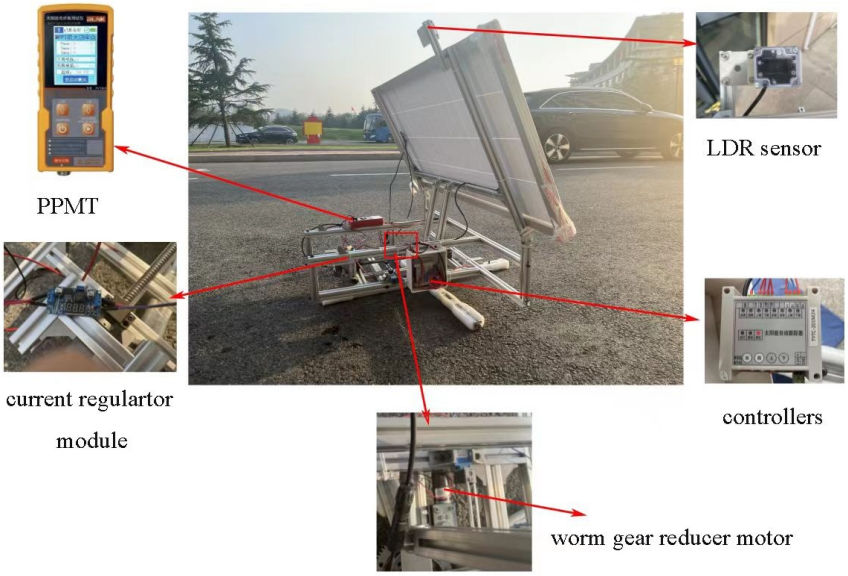

Figure 2. Physical diagram of solar panel tracking device with light.

(a) **(b)** **(c)**

Figure 3. Operation state of the device in the **(a)** morning (7:30 am); **(b)** noon (12:00 am); **(c)** afternoon (5:00 pm) of the day.

Figure 3a–c show the operation status of the passive sun-tracking power panel system in the morning, noon and afternoon of a sunny day. It is observed the sun panel tracking system works automatically and precisely with a deviation angle of ≤ 1°.

To measure the instantaneous sun panel output, the Photovoltaic Panel Multimeter Tester (PPMT), a PVT801 model tester with a testing power range of 0–800 W, is integrated into the passive sun tracking system. Connected to the solar panel's poles, the PPMT could monitor the instantaneous current and voltage output of the solar cell panel, thus measures the real-time maximum power generation capacity of the panel. By plotting the measured maximum power output at various times in the day, the power generation variation curve of the sun panel system could be obtained.

3. Results and analysis

3.1. Stress analysis on the dual-axis sun tracking system

The strength and stability of the dual-axis sun tracking device is crucial for the safe and efficient performance of the system. In this section, force analysis was perform on the mechanical part of the system with help of the state-of-the-art ANSYS software. The finite element method is used to discretize the structure into a finite number of small element, and based on the force balance between the material internal forces and external loads, the stress distribution in the structure can be numerically obtained.

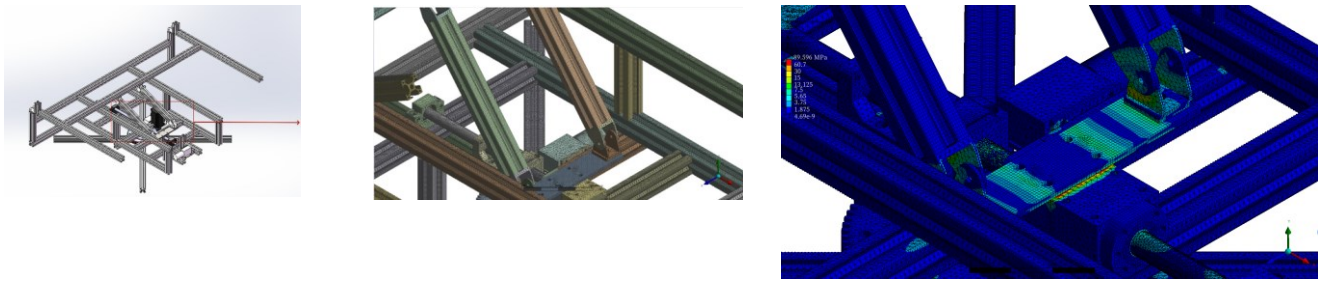

(a) **(b)** **(c)**

Figure 4. Force analysis of the mechanical part of the dual-axis sun-tracking system: **(a)** physical model; **(b)** meshing details; **(c)** stress distribution results.

Figure 4a–c displays the physical model of the mechanical part of the system, the mesh system as well as the stress distribution in the joint part of the apparatus after the force analysis study. In the stress analysis, a 200 N equivalent gravity force is applied above the solar panel support rod, and the device is subjected to a 2000 N wind load (about level 8 wind) in corresponding to the extreme weather conditions. As shown in **Figure 4c**, the simulation results indicate that the maximum stress occurs at the junction of the solar panel support bracket, with a maximum stress of 89.569 MPa, which is well below the yield strength 270 MPa and the tensile strength 310 MPa of the aluminum alloy material. The results indicate that the device's performance could meet the design requirements exceptionally well. It is observed the fabricated dual-axis sun tracking system exhibit high stability and load-bearing capacity under the harsh operational conditions and stress environments, thus ensuring the safe and reliable operation of the device in the practical applications.

3.2. Test conditions for PV power output measurement

Table 1 lists the dates when the measurements were performed. It is clearly observed that most days are sunny days, and 13th May and 21st, 22nd, 24th May, when it is slightly cloudy, cloudy, cloudy then sunny and cloudy then sunny, were employed to test the sensitivity of the measurement system.

Table 1. List of test dates and the weather conditions.

Date	weather conditions	temperature	wind force scale	wind direction
26 April 2023	sunny	11 ℃–15 ℃	4–5	southwest wind
1 May 2023	sunny	13 ℃–18 ℃	3–4	south wind
13 May 2023	slightly cloudy	14 ℃–20 ℃	3–4	south wind
16 May 2023	sunny	18 ℃–23 ℃	3–4	south wind
21 May 2023	cloudy	15 ℃–25 ℃	3–4	northwest wind
22 May 2023	cloudy then sunny	15 ℃–23 ℃	3–4	north wind
23 May 2023	sunny	18 ℃–27 ℃	3–4	northwest wind
24 May 2023	cloudy then sunny	16 ℃–18 ℃	3	southeast wind

To reveal the enhancement of the power output with the passive sun-tracking system, tests were performed at the fixed solar panel position as the control group. In the fixed sun panel system, the sun panel always faces south at a certain lift angle to the ground. The optimal tilting angle varies with the region, with a larger optimal tilt angle for the larger latitude regions. Even in the same latitude region, the optimal tilt angle would be affected by local meteorological conditions and other factors, such as the radiation intensity differences in the proportion of scattered and direct radiation of the sun. Specifically, the optimal azimuth angle and tilt angle in Qingdao, where this experiment is performed, are azimuth angles 2°–3° west of due south and a tilt angle of 34° in the spring season. Therefore, as the control group of this experiment, an azimuth angle of 2° west of due south and a tilt angle of 34° were set for the fixed system tests.

In the measurement procedure, we firstly measure the power output of the solar panel in the sun-tracking position, then disconnect the control unit and manually adjust the panel support system to the fixed position to perform the controlled measurement. The data acquisition position and moment for two set of measurements are therefore deemed to be the same. In this manner, we could ensure the accurate comparisons on energy output results between the sun-tracking and the fixed solar panel system.

3.3. Sensitivity analysis of the sun panel power output

Sensitivity studies of the sun panel power output in the passive sun-tracking system were performed on the 13th and 16th of May, as well as on the 21st–23rd of May, when the daily weather covers the slightly cloudy, cloudy & sunny to the all-day sunny conditions.

Figure 5a depicts the sun panel output on the slightly cloudy day of the 13th vs. on the sunny day of the 16th of May, whereas **Figure 5b** compares the sun panel output on three consecutive days, including the 21st a cloudy day, 22nd a cloudy then sunny day and 23rd a sunny day. It can be clearly observed from both subfigures that the sun panel shows satisfactory sensitivity to the sun radiation intensity, providing the highest power output on sunny days and giving the lowest power output on cloudy days. Its power generation varies sensitively with the different weather conditions as well. For instance, at 8:00–8:30 am in May 22nd, as shown in **Figure 5b**, the solar power output peak corresponds to the emerging sun from behind

the clouds, whereas the sharp increasing on power curves around 10:00 am corresponds accurately to the weather change from cloudy to sunny in that day. Based on the results in **Figure 5**, the sensitivity of the passive solar energy system can be satisfactorily demonstrated.

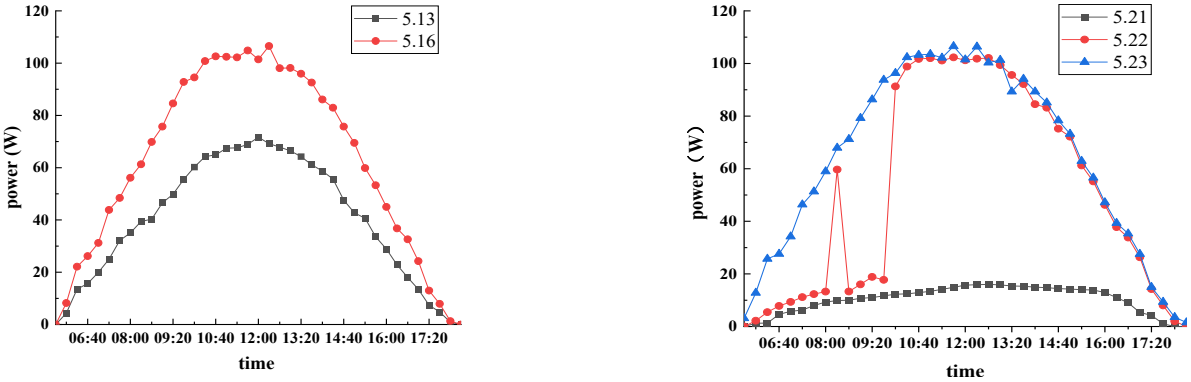

Figure 5. Sensitivity studies based on the solar panel power output comparisons under different weather conditions at **(a)** May 13th and 16th; **(b)** May 21st–23rd.

3.4. Power generation enhancement of the passive sun-tracking system

Based on power output comparisons between the passive sun-tracking system and the fixed panel system at a tilting angle of 34° on various days with different weather conditions, the advantages of the power generation performance of the passive sun-tracking system could be clarified. **Figure 6a–d** compare the power output data in the four sunny days of April 26th, May 1st, 16th and 23rd, to reveal the significant difference in power generation efficiency between the passive sun tracking system and the fixed solar panel system under favorable weather conditions.

Based on the four subfigures of **Figure 6**, it is clearly observed that the power output data in the passive sun-tracking system are all remarkably higher than those of the fixed panel system, which indicates that the sun-tracking system can perform more efficiently than the always south-facing fixed panel system. In particular, a remarkable deviation in the power output curves appears in the morning and afternoon because the sun inclines toward the east and west in that period of the day, when the fixed panel system cannot face to the direct sunlight radiation, whereas the passive sun-tracking device can orient towards the sun thereby ensures the solar panel continuously receiving the high intensity sun radiation.

By integrating the instantaneous power output line over the time period of the day in **Figure 6a–d**, **Figure 7** plots the accumulative power output for the sun-tracking system and the fixed panel system at the aforementioned four sunny days. It is clearly observed the passive sun-tracking system can significantly elevate the daily power generation efficiency in comparison with the fixed panel system at a lift angle of 34°. Specifically, as listed in **Table 2** in later part of the section, the exact extent of power output increase are in the range 29%–43%. In comparison with Alomar et al. [43], who reported the dual tracking system could yield extra energy up to 26% annually, the fabricated passive sun tracking system in this study has

shown an even higher solar power generation efficiency.

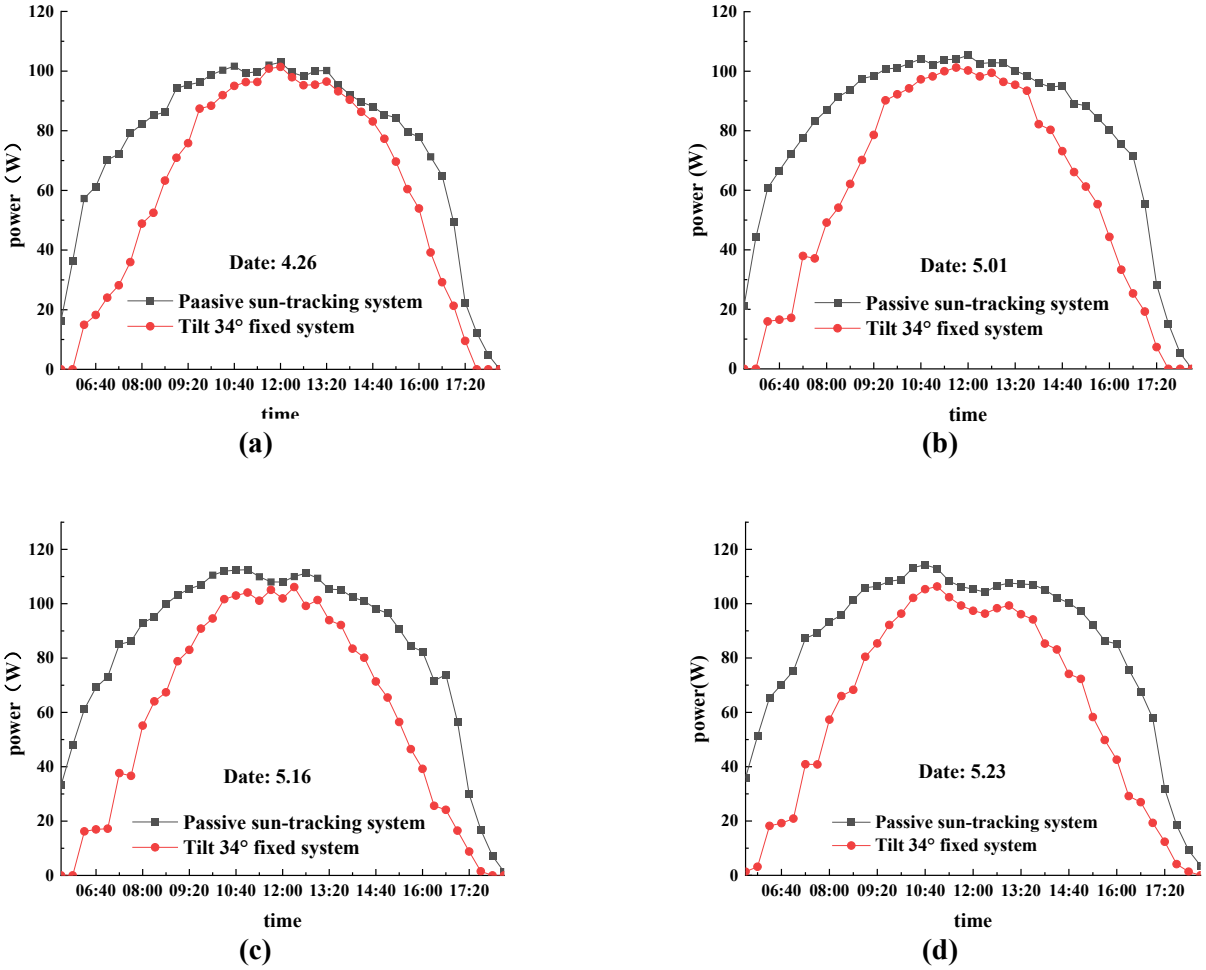

Figure 6. The daily power output results for both passive sun-tracking system and the fixed panel system at the sunny days of **(a)** April 26th; **(b)** May 1st; **(c)** May 16th; **(d)** May 23rd.

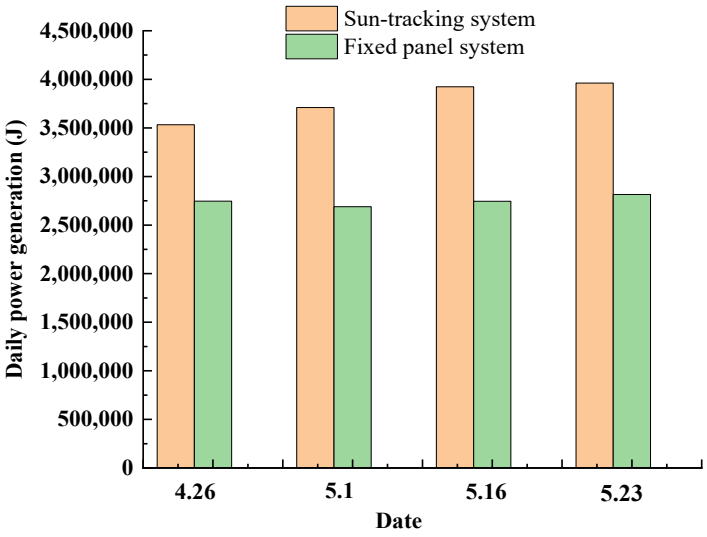

Figure 7. Comparisons on daily power output between the passive sun-tracking solar panel system and the fixed solar panel system at four sunny days.

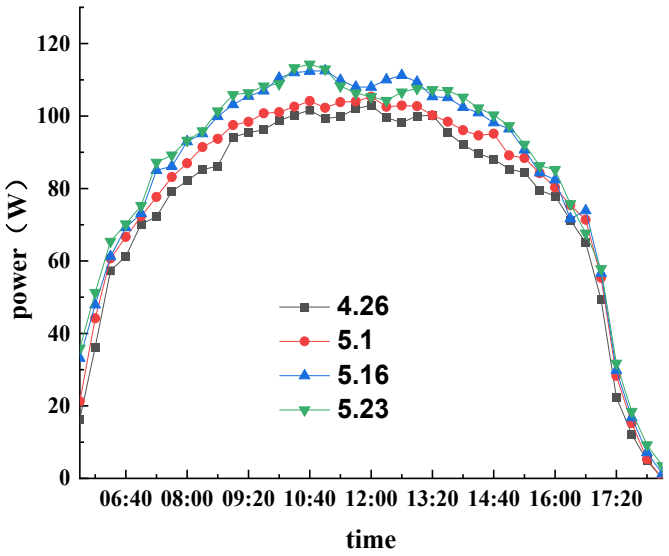

Figure 8. The power output curves of the passive sun-tracking system at various sunny days in the spring season showing the temperature effect.

In **Figure 7**, it is observed small difference in the output power of the fixed solar system among the few days, while the power output of the tracking solar system increases gradually with the change of date. The reason behind this observation can contribute to the different weather temperatures in these days. By referring to **Table 1**, it is observed the higher power output of the solar tracking system occurs at the date with higher weather temperature. **Figure 8** depicts the relationship between the weather temperatures and power output capacity of the passive sun-tracking solar panel system. In accordance to **Table 1**, the temperature on May 23rd is the highest at 18 ℃–27 ℃ and the temperature on April 26th is the lowest at 11 ℃–15 ℃, the solar panel power output accordingly records the highest values on May 23rd and the lowest values on April 26th. The power output from the fixed solar panel system shall be also sensible to the air temperature, however as shown in **Figure 6a–d**, the peak power output region of the fixed panel system only confines in the narrow mid noon period of the day, which restricts the favorable temperature effect on the daily power output of the fixed panel system.

To check the robustness of the passive sun tracking system under unfavorable cloudy weather conditions, we conducted measurement in the date of May 24th, when the weather was cloudy and sunny. **Figure 9** plots the real time power output data of the sun tracking system together with those of the fixed panel system. The results clearly show that the power output levels under both configurations stayed at the low level under the cloudy condition at morning and noon, but returned to the optimal performance at the afternoon of that day when the weather turned into sunny. It is also found from **Figure 9** that the power output curves for both systems have the similar trends but the one for passive sun-tracking system is obviously higher than the solar PV panel fixed system. It is concluded the passive sun-tracking system show high sensitivity to the sun radiation even under the cloudy weather conditions and therefore enhances significantly the solar PV power generation efficiency.

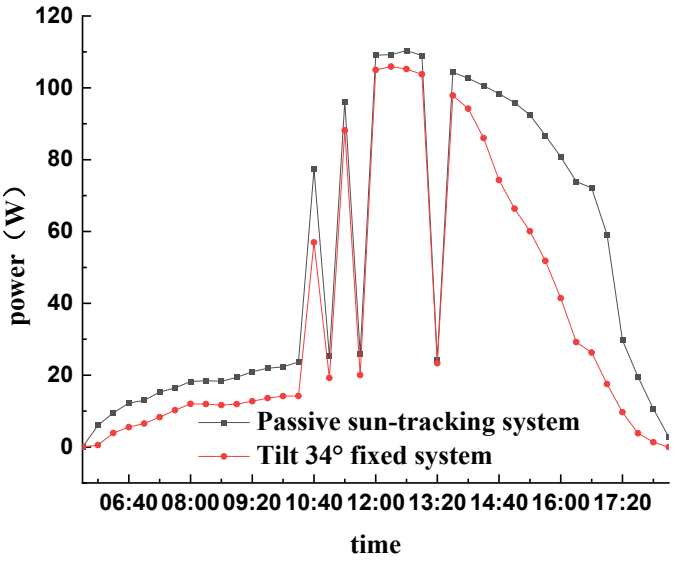

Figure 9. The daily power output result for both passive sun-tracking system and the fixed panel system at the cloudy and sunny day.

Table 2 summarizes the exact power generation outputs of the dual-axis sun tracking system and the fixed panel system in the aforementioned four sunny days and the one cloudy and sunny day. The power generation enhancement rates of the sun tracking system against the fixed panel system are also provided in the table. It is observed that, by employing the sun tracking system, the power generation capacity of the solar PV system could increase remarkably by 28.5%–42.9%, clearly showing the advantages of the passive dual-axis sun tracking system reported in this paper.

Table 2. Comparisons on the daily power generation results under different weather conditions between the sun-tracking system and the fixed panel system.

Date and weather	Power output of sun tracking system (J)	Power output of fixed system(J)	Enhancement rate
April 26 (sunny)	3,533,365.8	2,746,718	28.6%
May 1 (sunny)	3,709,486.92	2,689,351.2	37.9%
May 16 (sunny)	3,923,015.16	2,744,821.2	42.9%
May 23 (sunny)	3,961,084.8	2,714,829.2	40.7%
May 24 (cloudy and sunny)	2,342,420.4	1,710,064.8	37.0%

3.5. Economic analysis

The advantages of the passive sun-tracking system on economic aspects were demonstrated based on comparisons with other reported apparatus with the similar functions. The apparatus designed by Boukdir and EL Omari [36] employed 3D printed support structure together with multiple parts, including three LDR sensors, Fresnel lenses, vacuum tube collectors, microcontrollers, RTC modules, touch screens, power modules and so on. The dual-axis solar tracker developed by Anshory et al. [39] employed the external power source to help rotating the panel support based on the ESP8266 microcontroller and the LDR sensor. Lu and Ajay [38] used

two different sensors, one for sun position prediction and one for solar panel movement adjustment, to fulfill the dual axis sun tracking operation with help of the external power supply. It is concluded, therefore, the passive sun-tracking system reported in this paper show superior cost advantages based on the fact that it is built at simple mechanical structures without employing external power source and complex control systems.

Table 3 lists the total expenses for worm gear, LDR with controller and two motors, which are the supplementary parts of the passive sun-tracking system over the fixed tilted system. The annual benefit is estimated at 35% extra daily power output (about 0.2 kWh) for 240 sunny days (accounting for approximately 65% of 365 days in Qingdao city) at electricity price of 1RMB/kWh. It is calculated, therefore, the payback period for the passive sun-tracking is about 10 years.

Table 3. Cost-benefit analysis.

Cost (parts vs. prices)		**Benefit**	
worm gear	120 RMB	Daily extra power output	0.2 kWh
LDR with controller	250 RMB	Electricity	1 RMB/kWh
2 motors	110 RMB	Annual power output days	240

4. Conclusion

In this paper, a passive sun-tracking system was designed and fabricated. Detailed mechanical parts, the control part and the measurement unit were described. The advantages of the sun tracking system were illustrated by comparing with the power output of a fixed solar panel system. It is concluded that:

1) The power consumption to drive the passive sun tracking solar panel system is less than 5 W and can be well covered by the power generated by the solar panel, which is in the range of 20–100 W on a sunny day in the spring season;
2) Based on comparative measurement results on the power output of the sun passive tracking solar panel system and the fixed panel system at a tilting angle of 34°, it is concluded that the power generation efficiency of the passive sun tracking system is obviously higher than that of the fixed panel system, especially in the morning and afternoon of the day;
3) The accumulative daily power output of the solar panel in the passive sun-tracking system is 28.5%–42.9% higher than that of the fixed panel system under the sunny weather conditions. Even in the partly cloudy weather, the passive sun-tracking solar system could still generate 37% more power than the fixed panel system.

Author contributions: Conceptualization, YL and DD; methodology, YL and DD; formal analysis, GS and DH; investigation, GS and DH; writing—original draft preparation, GS; writing—review and editing, ZH and DD; supervision, ZH and DD; project administration, YL and DD. All authors have read and agreed to the published version of the manuscript.

Acknowledgments: We gratefully acknowledge the financial support of the Graduate tutor foundation of Qingdao University of Science and Technology (120202190414).

Conflict of interest: The authors declare no conflict of interest.

References

1. Wang X, Cui X, Wang F, et al. Miscibility characteristics of the CO2/n-hexadecane system with presence of water component based on the phase equilibrium calculation on the interface region. Colloids and Surfaces A: Physicochemical and Engineering Aspects. 2021; 629: 127463. doi: 10.1016/j.colsurfa.2021.127463
2. Cui P, Liu Z, Cui X, et al. Impact of water on miscibility characteristics of the CO2/n-hexadecane system using the pendant drop shape analysis method. Arabian Journal of Chemistry. 2023; 16(9): 105038. doi: 10.1016/j.arabjc.2023.105038
3. Cui X, Zheng L, Liu Z, et al. Determination of the minimum miscibility pressure of the CO2/oil system based on quantification of the oil droplet volume reduction behavior. Colloids and Surfaces A: Physicochemical and Engineering Aspects. 2022; 653: 130058. doi: 10.1016/j.colsurfa.2022.130058
4. Du D, Sun S, Zhang N, et al. Pressure distribution measurements for co2 foam flow in porous media. Journal of Porous Media. 2015; 18(11): 1119-1126. doi: 10.1615/jpormedia.2015012151
5. Du D, Zhang N, Li Y, et al. Parametric studies on foam displacement behavior in a layered heterogeneous porous media based on the stochastic population balance model. Journal of Natural Gas Science and Engineering. 2017; 48: 1-12. doi: 10.1016/j.jngse.2017.08.035
6. Du D, Zheng L, Ma K, et al. Determination of diffusion coefficient of a miscible CO2/n-hexadecane system with Dynamic Pendant Drop Volume Analysis (DPDVA) technique. International Journal of Heat and Mass Transfer. 2019; 139: 982-989. doi: 10.1016/j.ijheatmasstransfer.2019.05.083
7. Du D, Zhang X, Yu K, et al. Parameter Screening Study for Optimizing the Static Properties of Nanoparticle-Stabilized CO2 Foam Based on Orthogonal Experimental Design. ACS Omega. 2020; 5(8): 4014-4023. doi: 10.1021/acsomega.9b03543
8. Li Y, Zhao D, Du D. Computational study on the three phase displacement characteristics of foam fluids in porous media. Journal of Petroleum Science and Engineering. 2022; 215: 110732. doi: 10.1016/j.petrol.2022.110732
9. Liu Z, Cui P, Cui X, et al. Prediction of CO2 solubility in NaCl brine under geological conditions with an improved binary interaction parameter in the Søreide-Whitson model. Geothermics. 2022; 105: 102544. doi: 10.1016/j.geothermics.2022.102544
10. Liu Z, Yan S, Zang H, et al. Quantization of the water presence effect on the diffusion coefficients of the CO2/oil system with the dynamic pendant drop volume analysis technique. Chemical Engineering Science. 2023; 281: 119142. doi: 10.1016/j.ces.2023.119142
11. Song X, Cui X, Jiang L, et al. Multi-parameter screening study on the static properties of nanoparticle-stabilized CO2 foam near the CO2 critical point. Arabian Journal of Chemistry. 2022; 15(3): 103676. doi: 10.1016/j.arabjc.2021.103676
12. Chong Z, Wang Q, Wang L. Is the photovoltaic power generation policy effective in China? A quantitative analysis of policy synergy based on text mining. Technological Forecasting and Social Change. 2023; 195: 122770. doi: 10.1016/j.techfore.2023.122770
13. He YL, Qiu Y, Wang K, et al. Perspective of concentrating solar power. Energy. 2020; 198: 117373. doi: 10.1016/j.energy.2020.117373
14. Li YG, Du DX. Characterization of Amorphous Silicon Thin Films Deposited on Upilex-s Polyimide Substrates for Application in Flexible Solar Cells. Advanced Materials Research. 2009; 87-88: 416-421. doi: 10.4028/www.scientific.net/amr.87-88.416
15. Li G, Li M, Taylor R, et al. Solar energy utilisation: Current status and roll-out potential. Applied Thermal Engineering. 2022; 209: 118285. doi: 10.1016/j.applthermaleng.2022.118285
16. Qiu S, Wang K, Lin B, et al. Economic analysis of residential solar photovoltaic systems in China. Journal of Cleaner Production. 2021; 282: 125297. doi: 10.1016/j.jclepro.2020.125297
17. Russo MA, Carvalho D, Martins N, et al. Future perspectives for wind and solar electricity production under high-resolution climate change scenarios. Journal of Cleaner Production. 2023; 404: 136997. doi: 10.1016/j.jclepro.2023.136997
18. Shahabuddin M, Alim MA, Alam T, et al. A critical review on the development and challenges of concentrated solar power

technologies. Sustainable Energy Technologies and Assessments. 2021; 47: 101434. doi: 10.1016/j.seta.2021.101434
19. Tang W, Qi J, Wang Y, et al. Dense station-based potential assessment for solar photovoltaic generation in China. Journal of Cleaner Production. 2023; 414: 137607. doi: 10.1016/j.jclepro.2023.137607
20. Zhang X, Ang YS, Ye Z, et al. Three-terminal heterojunction bipolar transistor solar cells with non-ideal effects: Efficiency limit and parametric optimum selection. Energy Conversion and Management. 2019; 188: 112-119. doi: 10.1016/j.enconman.2019.03.034
21. Zhang X, Li J, Wang J, et al. Three-dimensional Dirac material anode enables concentrated solar thermionic converters. Optics Letters. 2021; 46(18): 4530. doi: 10.1364/ol.434653
22. Zhang X, Rahman E. Solar thermionic energy converters with micro-gap spacers. Optics Letters. 2023; 48(15): 4173. doi: 10.1364/ol.498374
23. García-López M, Montano B, Melgarejo J. The financial competitiveness of photovoltaic installations in water utilities: The case of the Tagus-Segura water transfer system. Solar Energy. 2023; 249: 734-743. doi: 10.1016/j.solener.2022.12.025
24. Palm J. Household installation of solar panels – Motives and barriers in a 10-year perspective. Energy Policy. 2018; 113: 1-8. doi: 10.1016/j.enpol.2017.10.047
25. Yao H, Zhou Q. Research status and application of rooftop photovoltaic Generation Systems. Cleaner Energy Systems. 2023; 5: 100065. doi: 10.1016/j.cles.2023.100065
26. Imteaz MA, Ahsan A. Solar panels: Real efficiencies, potential productions and payback periods for major Australian cities. Sustainable Energy Technologies and Assessments. 2018; 25: 119-125. doi: 10.1016/j.seta.2017.12.007
27. Widodo Besar Riyadi T, Effendy M, Radiant Utomo B, et al. Performance of a photovoltaic-thermoelectric generator panel in combination with various solar tracking systems. Applied Thermal Engineering. 2023; 235: 121336. doi: 10.1016/j.applthermaleng.2023.121336
28. Mamodiya U, Tiwari N. Dual-axis solar tracking system with different control strategies for improved energy efficiency. Computers and Electrical Engineering. 2023; 111: 108920. doi: 10.1016/j.compeleceng.2023.108920
29. Zhu Y, Liu J, Yang X. Design and performance analysis of a solar tracking system with a novel single-axis tracking structure to maximize energy collection. Applied Energy. 2020; 264: 114647. doi: 10.1016/j.apenergy.2020.114647
30. Mpodi EK, Tjiparuro Z, Matsebe O. Review of dual axis solar tracking and development of its functional model. Procedia Manufacturing. 2019; 35: 580-588. doi: 10.1016/j.promfg.2019.05.082
31. Josely Jose P, Akbari P, Dhokiya J, et al. Solar tracking: The best alternative to obtain more solar power output. Materials Today: Proceedings. 2022; 67: 921-926. doi: 10.1016/j.matpr.2022.08.065
32. Zaghba L, Khennane M, Mekhilef S, et al. Experimental outdoor performance assessment and energy efficiency of 11.28 kWp grid tied PV systems with sun tracker installed in saharan climate: A case study in Ghardaia, Algeria. Solar Energy. 2022; 243: 174-192. doi: 10.1016/j.solener.2022.07.045
33. Muthukumar P, Manikandan S, Muniraj R, et al. Energy efficient dual axis solar tracking system using IOT. Measurement: Sensors. 2023; 28: 100825. doi: 10.1016/j.measen.2023.100825
34. Ravikiran Ch, Nagaraju S, Akhil D, et al. Design of solar array with sun position tracking system employing refrigerant. Materials Today: Proceedings. doi: 10.1016/j.matpr.2023.05.032
35. Awasthi A, Shukla AK, S.R. MM, et al. Review on sun tracking technology in solar PV system. Energy Reports. 2020; 6: 392-405. doi: 10.1016/j.egyr.2020.02.004
36. Boukdir Y, EL Omari H. Novel high precision low-cost dual axis sun tracker based on three light sensors. Heliyon. 2022; 8(12): e12412. doi: 10.1016/j.heliyon.2022.e12412
37. Palomino-Resendiz SI, Flores-Hernández DA, Cantera-Cantera LA, et al. Design and implementation of Model-Based Predictive Control for two-axis Solar Tracker. Solar Energy. 2023; 265: 112080. doi: 10.1016/j.solener.2023.112080
38. Lu W, Ajay P. Solar PV tracking system using arithmetic optimization with dual axis and sensor. Measurement: Sensors. 2024; 33: 101089. doi: 10.1016/j.measen.2024.101089
39. Anshory I, Jamaaluddin J, Fahruddin A, et al. Monitoring solar heat intensity of dual axis solar tracker control system: New approach. Case Studies in Thermal Engineering. 2024; 53: 103791. doi: 10.1016/j.csite.2023.103791
40. Kumar Gupta A, Kumar Chouksey V, Pandey A. Design and study of an autonomous linear welding robot with mechanical referencing system. Materials Today: Proceedings. Published online August 2023. doi: 10.1016/j.matpr.2023.08.111
41. Xu L, Ding P, Zhang Y, et al. Sensitivity analysis of the shading effects from obstructions at different positions on solar photovoltaic panels. Energy. 2024; 290: 130229. doi: 10.1016/j.energy.2023.130229

42. Zhou X, Duan Z. Investigation on the basic principles of human-machine contact force, based on screw theory. Heliyon. 2023; 9(3): e13851. doi: 10.1016/j.heliyon.2023.e13851
43. Alomar OR, Ali OM, Ali BM, et al. Energy, exergy, economical and environmental analysis of photovoltaic solar panel for fixed, single and dual axis tracking systems: An experimental and theoretical study. Case Studies in Thermal Engineering. 2023; 51: 103635. doi: 10.1016/j.csite.2023.103635

Thermal Science and Engineering 2024, 7(1), 5842.
https://doi.org/10.24294/tse.v7i1.5842

Review

Exploring the versatile production techniques and applications of nitrogen-doped activated carbon

Reza Joia[1,2,*], Meiram Atamanov[1], Kuanysh Umbetkaliev[1], Mohammad Hamid Mohammadi[3,4], Sayed Reza Sarwari[2], Taibullah Modaqeq[1]

[1] Department of Chemical Physics and Material Science, Faculty of Chemistry and Chemical Technology, Al-Farabi Kazakh National University, Almaty 050040, Kazakhstan
[2] Department of Chemistry, Faculty of Education, Nimruz Higher Education Institute, Nimruz 4301, Afghanistan
[3] Department of Biotechnology, Faculty of Biology and Biotechnology, Al-Farabi Kazakh National University, Almaty 050040, Kazakhstan
[4] Department of Biology, Faculty of Education, Daikundi Higher Education Institute, Daikundi 4201, Afghanistan
*** Corresponding author:** Reza Joia, joia.reza@yahoo.com

CITATION

Joia R, Atamanov M, Umbetkaliev K, et al. Exploring the versatile production techniques and applications of nitrogen-doped activated carbon. Thermal Science and Engineering. 2024; 7(1): 5842. https://doi.org/10.24294/tse.v7i1.5842

ARTICLE INFO

Received: 4 December 2023
Accepted: 17 January 2024
Available online: 29 January 2024

Abstract: Carbon based materials are really an integral component of our lives and widespread research regarding their properties was conducted along this process. The addition of dopants to carbon materials, either during the production process or later on, has been actively investigated by researchers all over the world who are looking into how doping can enhance the performance of materials and how to overcome the current difficulties. This study explores synthesis methods for nitrogen-doped carbon materials, focusing on advancements in adsorption of different pollutants like CO_2 from air and organic, inorganic and ions pollutants from water, energy conversion, and storage, offering novel solutions to environmental and energy challenges. It addresses current issues with nitrogen-doped carbon materials, aiming to contribute to sustainable solutions in environmental and energy sciences. Alongside precursor types and synthesis methods, a significant relationship exists between nitrogen content percentage and adsorption capacity in nitrogen-doped activated carbon. Nitrogen content ranges from 0.64% to 11.23%, correlating with adsorption capacities from 0.05 mmol/g to 7.9 mmol/g. Moreover, an electrochemical correlation is observed between nitrogen atom increase and specific capacity in nitrogen-doped activated carbon electrodes. Higher nitrogen percentage corresponds to increased specific capacity and capacity retention. This comprehensive analysis sheds light on the potential of nitrogen-doped carbon materials and highlights their significance in addressing critical environmental and energy challenges.

Keywords: CO_2 capture; doping agent; energy conversion; energy storage; raw material; synthesis methods

1. Introduction

Nitrogen-doped activated carbon, a sophisticated and innovative material, has emerged as a key player in the realm of environmental science and technology, particularly in the context of carbon dioxide (CO_2) adsorption [1]. This unique variant of activated carbon holds significant importance in addressing the escalating concerns related to global climate change and greenhouse gas emissions [2]. The integration of nitrogen into the carbon matrix enhances its adsorption capabilities, making it an invaluable tool in the pursuit of sustainable solutions. One of the pivotal roles of nitrogen-doped activated carbon lies in its exceptional capacity for CO_2 adsorption [3]. Carbon dioxide, a major greenhouse gas, contributes substantially to the warming of the Earth's atmosphere. The urgency to mitigate the adverse effects of climate change has intensified the search for efficient methods to capture and sequester CO_2 [4].

Nitrogen-doped activated carbon, with its tailored surface chemistry and increased porosity, provides an ideal substrate for the adsorption of CO_2 molecules [5]. The introduction of nitrogen functionalities enhances the affinity of the material for CO_2, making it a promising candidate for carbon capture applications [6]. The production methods employed in the synthesis of nitrogen-doped activated carbon play a crucial role in determining its structural properties and adsorption performance [7]. Typically derived from precursor materials such as biomass or synthetic polymers, the activation process involves subjecting the carbonaceous material to high temperatures in the presence of a nitrogen-containing gas [8]. This not only creates an activated carbon framework with a high surface area but also introduces nitrogen atoms into the carbon lattice [9]. The resulting material exhibits improved textural properties and enhanced surface functionality, contributing to its heightened CO_2 adsorption capacity [10]. Understanding the necessity of CO_2 capture becomes imperative in the context of climate change and its far-reaching consequences. The Earth's climate is intricately linked to the delicate balance of greenhouse gases in the atmosphere [11]. The alarming increase in CO_2 concentrations, the human activities such as the combustion of fossil fuels and the clearing of forests, are count as the main cause of the global temperature increases [12]. By capturing and sequestering CO_2, nitrogen-doped activated carbon offers a tangible and effective means to mitigate the impacts of climate change [12]. At all, nitrogen-doped activated carbon stands at the forefront of sustainable technologies, particularly in the vital realm of CO_2 adsorption [13]. Its tailored production methods and inherent structural properties make it a powerful tool in the quest for mitigating the impacts of climate change [14]. As the global community grapples with the imperative to reduce CO_2 emissions, the development and application of advanced materials like nitrogen-doped activated carbon underscore the potential for innovation to contribute to a more sustainable and environmentally conscious future [15].

2. Production of N-doped activated carbon

Nitrogen doped activated carbon (NACs) is already produced by scientists from different types of plant waste by various activation methods and they obtained N-doped AC with high surface area, suitable structure and pore size and huge adsorption capacity for uptake CO_2 [16]. The general synthesis principle of Nitrogen doped AC are classified in Chemical or direct activation also this method is known as in-situ synthesis [17], Physical activation [18], and hydrothermal method [13].

Chemical Activation with Nitrogen-Containing Compounds: In this method, the precursor material is impregnated with a nitrogen-containing compound, like urea [19], melamine [20], before carbonization and activation. The activation process is carried out at high temperatures, typically between 700–900 °C and adding some activation agent like KOH [21], ZnCl [22], ... This method introduces nitrogen atoms to the activated carbon structure [23].

Physical Methods: Physical activation is a widely used method for producing activated carbon. The procedure includes converting a precursor material into carbon through carbonization, followed by activation using a physical agent like steam or carbon dioxide [16]. Nitrogen doping can be achieved during the physical activation

process by introducing nitrogen-containing gases, such as ammonia [24] or other gases that contain nitrogen atoms [9]. The synthesis of nitrogen-doped activated carbons (N-ACs) through physical methods involves processes that modify the carbon structure without the use of chemical agents [10]. Various physical methods and associated nitrogen types include:

High-Temperature Pyrolysis: N-doped activated carbons are created through the pyrolysis of carbon precursors at elevated temperatures, allowing for the incorporation of nitrogen into the carbon lattice [25]. Nitrogen functionalities introduced may include pyridinic and pyrrolic nitrogen.

Gas Activation: In this method, carbon precursors are exposed to activating gases, such as steam or carbon dioxide, at high temperatures [26]. Physical activation results in tailored pore structures and the introduction of nitrogen functionalities like pyridinic and pyrrolic nitrogen [27].

Template Method: A template, often a sacrificial substance, is utilized to create porous structures in the carbon material. Nitrogen-doping is achieved through the introduction of nitrogen-containing precursors during the templating process [28].

These physical synthesis methods yield nitrogen-doped activated carbons with specific characteristics, offering versatility in applications such as CO_2 capture.

Hydrothermal method: this is a promising technique for obtaining nitrogen-doped activated carbon due to its ability to incorporate nitrogen into the carbon structure and control the pore size distribution [29]. In this method according to **Figure 1** the precursor is mixed with a nitrogen-containing compound, such as urea or ammonia, and placed in furnace tube for several hours and 400-8000C [11], according to the type of precursor. And after passing hydrothermal treatment, applied carbonization and activation steps the same as physical method on threated material [27].

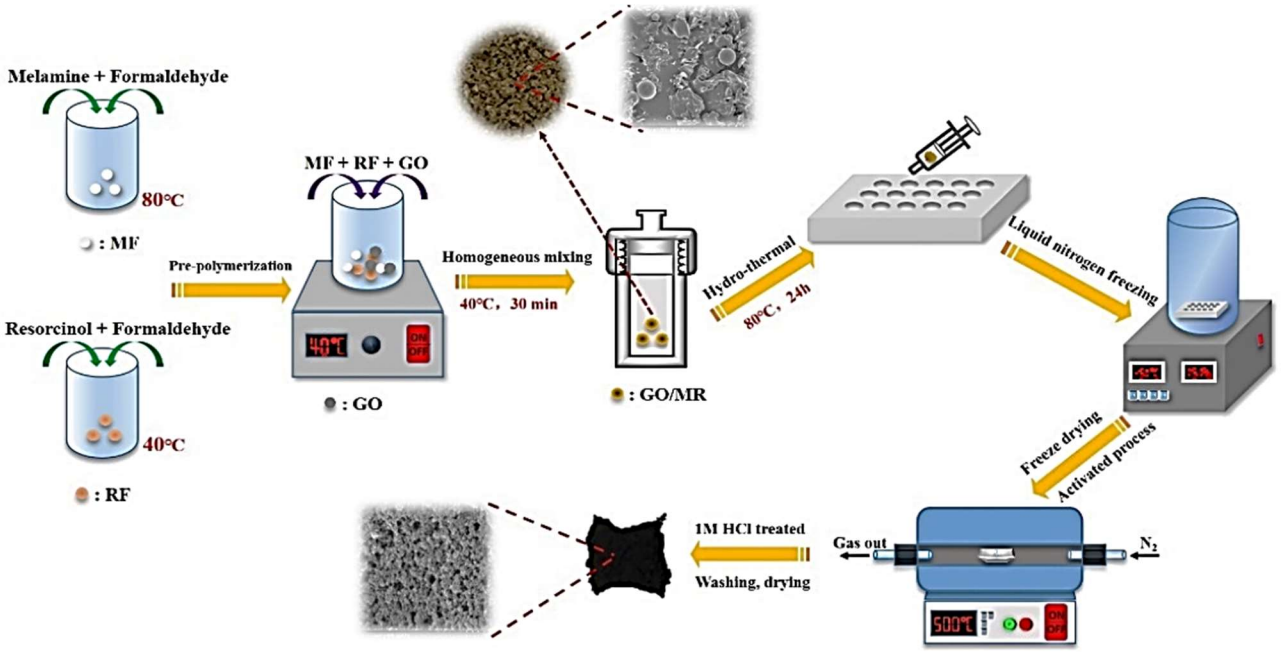

Figure 1. Schematic exhibition of hydrothermal synthesis process for N-doped activated carbon materials derived from a GO/MR composite. Reproduced by permission from Ref [30].

However, the selection of raw materials with excellent carbon content and no

inorganic components, suitable production method and high nitrogen content doping agents are all important to achieve N-doped activated carbon with high quality (high surface area, high adsorption capacity, and appropriate pore size and pore structure [31]. The production of N-doped activated carbons (N-ACs) in all mentioned methods involve introducing nitrogen functionalities into the carbon matrix, to increase CO_2 adsorption capacity of product [32]. There are three types of nitrogen functionalities that were introduced during production (see **Figure 2**).

Pyridinic Nitrogen: Embedded in the carbon lattice, pyridinic nitrogen provides active sites for CO_2 adsorption [33].

Pyrrolic Nitrogen: Present in the form of five-membered rings, pyrrolic nitrogen contributes to enhanced surface reactivity [34].

Quaternary Nitrogen: This nitrogen form improves basicity and can act as a potential site for CO_2 adsorption [34].

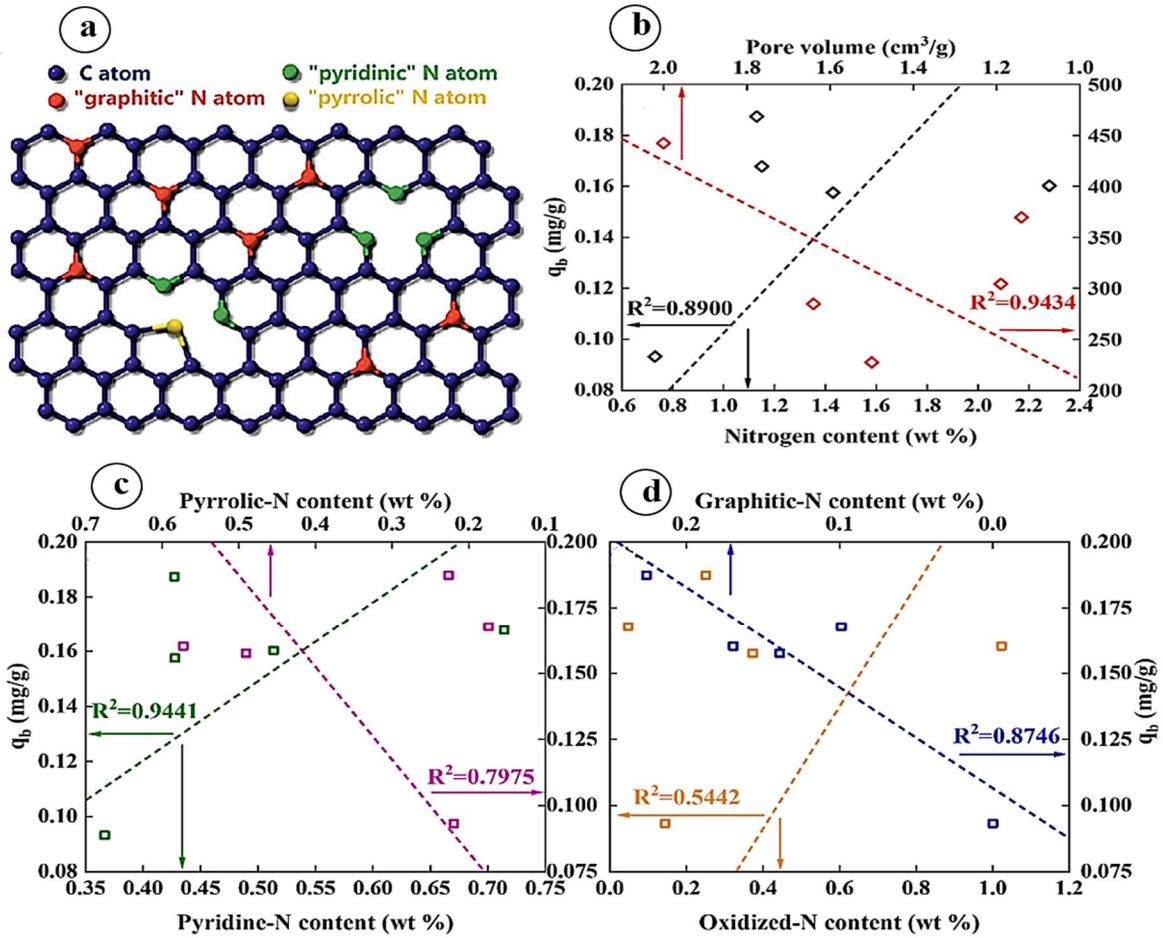

Figure 2. (a) Schematic Representation of Various Nitrogen Atom Types; **(b)** Nitrogen with graphitic, pyridinic, and pyrrolic structures, contributes to the composition of N-doped AC. Reprinted by permission from Ref [33]; **(b)** Correlations between adsorption capacity and lattice volume (normalized by BET surface area), as well as with the nitrogen content of the polymer species (qb values); **(c, d)** Affinity relationship between nitrogen content and qb. Reproduced by permission from Ref [35].

3. Conducted methods and synthesized N-doped activated carbon

Numerous methods for producing N-doped materials have been documented in

the literature (see **Table 1**), each utilizing different nitrogen sources, obtaining conditions, and equipment. The synthesis of N-doped carbon materials can occur either in situ or as a separate post-treatment process following the preparation of carbon materials. The addition of nitrogen atoms into carbon network can be achieved during CVD by use of nitrogen compounds together with carbon source or through the use of nitrogen containing carbon based compounds [33], This method is particularly beneficial for carbon nanotubes and graphene production [6]. However, other synthesis techniques such as solvothermal and arc-discharge methods can give the doping characteristics as well [36]. Other materials such as biomass have been used as a precursor. Pyrolysis acts as an in situ doping technique that is done at 800 ℃ in mostly cases [37]. Consideration of MOFs with nitrogen and carbon atoms has been done as precursors [38]. for N-doped carbon materials. These types of materials are usually formed by carbonization of MOFs at temperatures between 500 ℃ and 800 ℃. But the temperatures over 800 ℃ may cause the issue of structural damages and degradation [39]. On some other occasions mechanochemistry has been applied to bring in nitrogen species to the carbon matrix without requiring high temperatures [13].

Another approach is comprising of the electrochemical exfoliation of a carbon material to form N-doped graphene as electrode catalyst. This led to an amelioration of the graphene capacity in comparison to the pristine graphene [40]. By contrast, the second type of technique-post-treatment technique-is to add additional nitrogen atoms to the existing sites such as edge of a substrate and defects. For example, post-treatment techniques include annealing (300–500 ℃), hydrothermal processes [41], plasma treatment [13], and ion implantation [33].

Of all the doping techniques, chemical vapor deposition (CVD) is noted to be especially useful for nitrogen doping of carbon materials because it is highly efficient and also it is adaptable [34]. However, it requires significant temperatures. Implementation of ions produces more doped materials with few impurities, allows for precise control over doping levels and guarantees consistency of doping, whereas their disadvantages are the high cost and energy demands [42]. Leveraging the phenomenon of self-doping biomass as a potential source of precursors appears to be an attractive solution due to its abundant availability and eco-friendly nature. Nevertheless, using activation agents requires serious consideration, given that some chemicals like KOH can be harmful to the environment [13]. Consequently, reflection should become a mandatory step when choosing a more sustainable option, especially in the case of biomass application [43].

Table 1. The summary of some literature that is used for this review.

N-doped AC from	Production method	N-(%), surface area (m^2/g)	Application	Performance	Ref
Rice husk	Hydrothermal, KOH-activated	- (1495.52)	CO_2 adsorption	5.83 mmol/g at 273 K, 1 bar	[1]
Rice husk	Pre-deashed, pyrolysis, ammonia activated	N-0.38%,	CO_2 adsorption	High accordingly	[44]
FAU zeolite	Pyrolysis, Ca2+ ions catalyzed	N-5%, (2400)	CO_2 adsorption	3.25 mmol/g, 1 bar, (30 ℃)	[27]
Ethylenediamine + carbon tetrachloride	Pyrolysis, KOH activated	and N-3.3%, (1463)	supercapacitor	363 F/g at 0.1 A/g in 1 M H_2SO_4	[45]

Table 1. (*Continued*).

N-doped AC from	Production method	N-(%), surface area (m^2/g)	Application	Performance	Ref
Samanea saman leaves	Direct-activated by NaOH	N-4.6%, (2930)	supercapacitor	in organic electrolyte 179 F/g and 88 F/cm^3	[23]
Soybean	Both (chemical used $ZnCl_2$ and followed by physical used CO_2)	N-0.64%, (811)	CO_2 adsorption	23 mg/g at 120 C	[46]
Waste leaves of citrus aurantium	Hydrothermal carbonization, $ZnCl_2$-activated	-	CO_2 adsorption	8.43 mml/g, 1 bar, (25 ℃)	[47]
Cross-linked triazine polymer	Pyrolysis, KOH activated	N (7.89 atomic %), P (0.74 atomic %). (1332)	CO_2 adsorption, Supercapacitor	1.52 and 5.68 mmol/g at 1 and 5 bar, 172.7 F/g at a current density of 1 A/g.	[48]
Fe_3O_4+N-doped AC	Hydrothermal	-	Li- ion battery	480 mAh/g) at 20 A/g-1000 cycles.	[49]
N-doped rGO	Pyrolysis	-	Supercapacitor, Na-ion batteries	18.7 F/cm^3 at a current density of 1 A/cm^3.	[50]
Coconut shells	Hydrothermal, KOH activated	nitrogen and oxygen contents (11.23%, 13.53%)	CO_2 adsorption	(7.9 mmol/g, 100 kPa and 273 K	[51]
Yangchangwan coal	Hydrothermal, KOH activated	N-3.3%, (1920.7-3078.9)	CO_2 adsorption	5.96mmol/g at 25 ℃ and 3.92 mmol/g at 0 ℃	[19]
CNs grafted on ACFs	Chemical vapor deposition (CVD)	-	CO_2 adsorption	1.53–1.92 mmol/g at 1bar, 25 ℃	[34]
Hollow Ga_2O_3@N-CQD nanospheres	Hydrothermal	-	Li-ion battery	at 0.5 A/g, 700.5 mAh/g-500 cycle	[52]
Chitosan gel	Sol-gel, KNO3 activated	N-8.6%, O-13.5%, (678.8)	Supercapacitor	329.2 F/g in 6M KOH at 0.5A/g	[53]
PACP hollow nanosphere	Co-polymerization strategy-NH3-assisted carbonization, KOH activated.	N-6.25 atom%, (1237)	Energy Storage	789 mAh g^{-1} at 0.5 C after 200 cycles	[54]
Melamine resorcinol formaldehyde resin-graphene Oxide (MR-GO)	Pyrolysis, KOH activated	N-6.92%, (1264)	CO_2 adsorption	5.21 mmol/g at 25 ℃ and 500 kPa	[30]

Table 1: Overview of N-doped carbon materials outlined.

4. Application of N-doped activated carbon

The application of nitrogen-doped activated carbon represents a pivotal stride in materials science, presenting a myriad of opportunities across diverse sectors. The advantageous properties imbued by nitrogen doping have propelled this material to the forefront of technological innovation, with implications for energy storage, catalysis, and environmental remediation [13]. One of the most noteworthy applications is in the realm of energy storage [55]. Nitrogen-doped activated carbon has exhibited exceptional performance as an electrode material, especially in the evolution of supercapacitor and batteries [56]. Its enhanced electrochemical properties, stemming from the introduction of nitrogen functionalities, contribute to improved energy density, charge-discharge efficiency, and overall stability [57]. These attributes are critical for addressing the growing need for efficient and sustainable energy storage solutions in the face of escalating global energy needs [58]. Catalysis is another domain where nitrogen-doped activated carbon has demonstrated considerable prowess [59]. The introduction of nitrogen species into the carbon matrix serves as a

catalyst, influencing various chemical reactions [60]. This has far-reaching implications for industrial processes, including the production of fine chemicals and environmental remediation strategies. The catalytic activity, combined with the material's stability, makes it a compelling choice for advancing green and sustainable chemical synthesis. Moreover, the environmental applications of nitrogen-doped activated carbon are noteworthy [12]. Its adsorption capacity, influenced by the nitrogen functionalities, proves effective in capturing and removing pollutants from air and water [11]. This capability aligns with the growing emphasis on developing materials for environmental remediation, addressing issues such as water purification and air quality management [61]. As research on nitrogen-doped activated carbon continues to unfold, its versatility and adaptability become increasingly apparent. The exploration of novel synthesis methods, coupled with a deeper understanding of its structural and chemical characteristics, opens avenues for even more tailored applications [10]. Ultimately, the multifaceted nature of nitrogen-doped activated carbon positions it as a cornerstone material, contributing significantly to advancements in sustainable technologies and environmental conservation [18].

4.1. CO_2 adsorption

As the greenhouse gas CO_2 is being widely recognized as the major contributor to global warming, scientists have been researching the potential of nitrogen-doped materials in environmental and sustainable solutions [62]. The CO_2 adsorption process utilizes solid adsorbents having different adsorption mechanisms [31]. A range of porous solid materials, including carbon materials [7], and metal-organic frameworks (MOFs) [63], and their composites, have been researched and tested as CO_2 adsorbents [2]. Carbonaceous materials are among the most affordable options and have excellent CO_2 adsorption effectiveness (see **Figure 3a**), structural stability, and chemical stability. They can be used in many applications [64]. For instance, the formation of N-doped activated carbon (N-doped AC) by physical activation with carbon dioxide and nitrogen gas and has been reported. The material was carbonized at 800 ℃ and then activated with carbon dioxide and nitrogen gas at 800 ℃ for 2 h. The nitrogen doped AC thus produced had elevated nitrogen content and well defined pore size distribution and hence was suitable for catalysis [65]. The study further investigated the effect of activation temperature on the structures and properties of N-doped AC resulting from steam and ammonia physical activation. Beforehand, the precursor was carbonized at 900 ℃ and it was activated with steam and ammonia at 750 to 950 ℃ for 2 h. Our research showed that the activation temperature was the major factor governing the pore size distribution and nitrogen content of N-doped AC [66]. Moreover, peanut shell activated carbon was produced through the hydrothermal method by using urea solution as nitrogen source and KOH as a chemical activator. The synthesized activated carbon had a high surface area of 2700 m^2/g and a nitrogen content of 4.9%. The adsorption isotherm showed that the activated carbon had a high CO_2 adsorption capacity of 7.6 mmol/g at 298 K and 1 bar [67]. doping nitrogen in activated carbon enhances CO_2 adsorption capacity through several mechanisms: as instance, increasing the surface area [68], provide the context of chemisorption [7], improved pore structure, enhanced wettability, and increase surface basicity [8]. these

combined effects make N-doped activated carbon a promising material for CO_2 capture (**Figure 3b**), and sequestration applications.

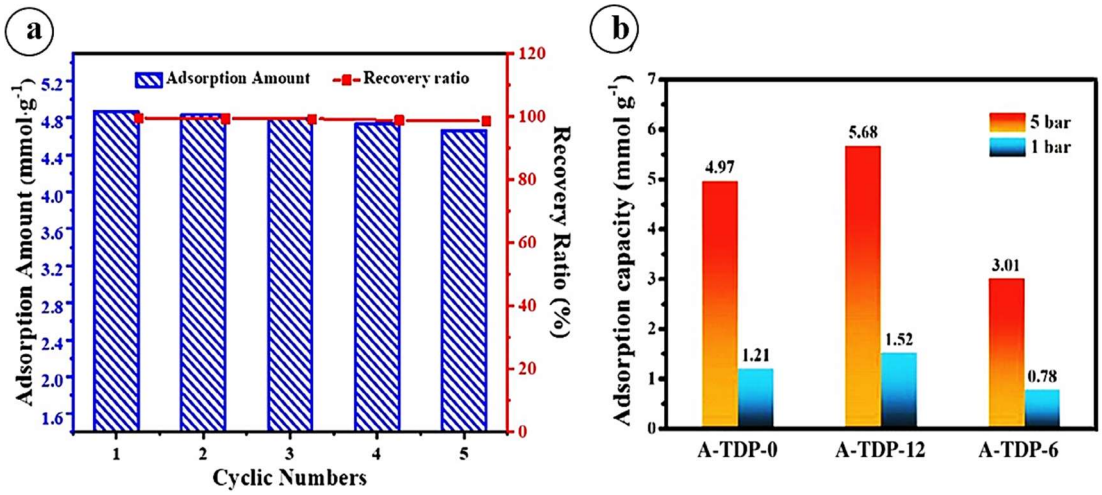

Figure 3. Cycling of CO_2 adsorption by GO (0.25)/MR-500 at 298.15 K and 500 kPa. **(a)** Amount of CO_2 adsorbed by MR/GO material at RT and 5 bar in 5 cycles. Reprinted by permission from Ref [30]. **(b)** The adsorption capabilities of diverse N/P co-doped carbon materials under varying pressures. Reprinted by permission from Ref [48].

4.2. Up taking Mechanisms of CO_2 by N-doped AC

The adsorption of carbon dioxide (CO_2) by nitrogen-doped activated carbon involves several key mechanisms that contribute to the overall process. Activated carbon is a porous material with a high surface area, and the introduction of nitrogen functionalities enhances its ability to adsorb CO_2 [19]. Here's an overview of the mechanisms involved:

4.2.1. Pore filling and surface adsorption

Nitrogen-doped activated carbons play a vital role in CO_2 adsorption by employing a dual mechanism of pore filling and surface adsorption (**Figure 4a**). These materials, crafted through diverse methods like urea modification, KOH activation, and physical activation, demonstrate remarkable efficacy in capturing CO_2 [7]. Nitrogen doping significantly enhances CO_2 adsorption capacity by introducing active sites for interaction with CO_2 molecules [8]. Pores within the activated carbon structure facilitate pore filling, enabling the physical entry of CO_2 molecules [69]. Furthermore, the nitrogen-doped activated carbon surface provides specific sites for chemical adsorption, fostering interactions with CO_2 molecules [1]. Research underscores the substantial contribution of N-doping to CO_2 adsorption, surpassing the impact of exceedingly high surface area values [70]. The synthesis of N-rich porous carbon serves as a tangible demonstration of the favorable traits that enhance CO_2 uptake [31].

4.2.2. Chemisorption with nitrogen functionalities

Nitrogen doping introduces nitrogen-type functional groups on to the activated carbonaceous surface. The most common nitrogen precursors include pyridinic, pyrrolic and graphitic nitrogen. When such nitrogen groups chemically bind with CO_2 with the help of chemisorption, these bonds become stronger and result in inherently resilient chemical bonds. As such, pyridinic nitrogen is the most active nitrogen found

in graphene as it can bond with CO_2 through Lewis acid-base action, (**Figure 4b**).

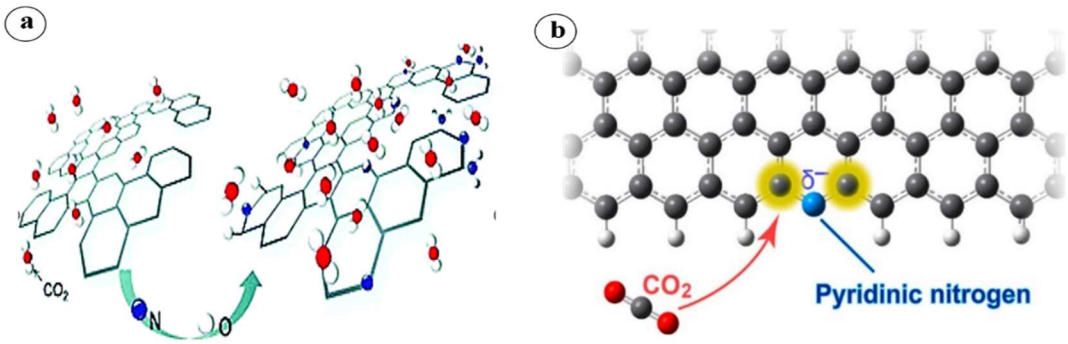

Figure 4. (a) Illustrate the adsorption of CO_2 on the surface of activated carbon. Reprinted by permission from Ref [6]. **(b)** show CO_2 by chemisorption process of CO_2 on N-doped AC Reprinted by permission from Ref [71].

4.2.3. Lewis acid-base interactions

Nitrogen functionalities, especially those with lone pair electrons, can act as Lewis bases, whereas CO_2 can act as a Lewis acid [72]. The Lewis acid and base reactions involve giving and taking electrons to make coordinate covalent bonds. This interaction improves the material's ability to capture CO_2 [73].

4.2.4. Electrostatic interactions

The presence of nitrogen-containing groups can introduce additional charge distribution on the surface of activated carbon. CO_2, being a polar molecule, can interact with the charged sites through electrostatic interactions, further contributing to its adsorption [74].

4.2.5. Enhanced surface heterogeneity

Nitrogen doping increases the surface heterogeneity of activated carbon, making different active sites for capturing CO_2, (see **Figure 5**). The diverse range of active sites allows for multiple interactions, including physical adsorption, chemisorption, and electrostatic interactions [75].

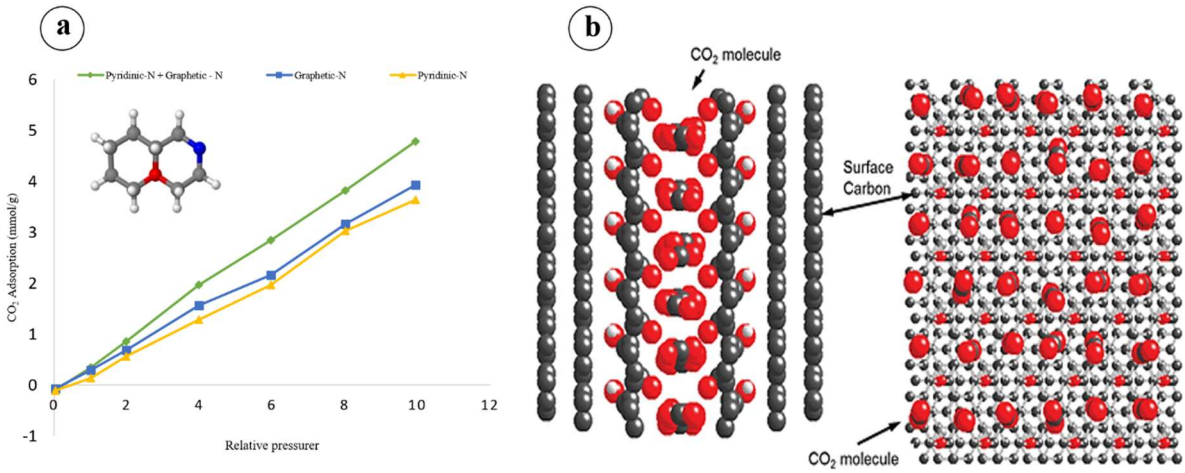

Figure 5. (a) Presents a simulation of CO_2 uptake isotherms at 298 K, exploring a pressure range up to 10 bar. The simulation involves a generated structure, highlighting the presence of Pyridinic-N (shown in yellow), Graphitic-N (depicted in Blue), and a mixture of both (in Brown). Reproduced by permission from Ref [76]; **(b)** Influence of Surface Variability on CO_2 Adsorption in Microporous Carbon Materials. Reprinted by permission from Ref [75].

4.2.6. Selective adsorption

Nitrogen-doped activated carbon can exhibit selective adsorption, preferentially adsorbing CO_2 over other gases due to specific interactions and affinity for CO_2 molecules [4]. The combination of physical adsorption [6], chemisorption [71], Lewis's acid-base interactions [72,73], electrostatic interactions [74], and surface heterogeneity [75], results in an effective adsorption process for CO_2 by nitrogen-doped activated carbon. This makes such materials promising candidates for applications in carbon capture and storage, as well as other environmental and energy-related processes.

Research manuscripts reporting large datasets that are deposited in a publicly available database should specify where the data have been deposited and provide the relevant accession numbers. If the accession numbers have not yet been obtained at the time of submission, please state that they will be provided during review. They must be provided prior to publication.

Interventionary studies involving animals or humans, and other studies that require ethical approval, must list the authority that provided approval and the corresponding ethical approval code.

4.3. Energy storage systems

4.3.1. Supercapacitor

The strategy of nitrogen doping into the structure of carbon-based materials has become the biggest game changer in enhancing the specific capacitance of electrode materials, which in turn has ignited interest in using N-doped AC, in supercapacitors these days [77]. Various aspects including porosity, surface area, and the exact amount and type of nitrogen are the factors which determine the electrochemical performance of N-doped AC electrodes, in terms of the specific capacitance, rate capability, and cycle stability [78]. The most recent research indicates that the nature of N atom arrangement on the surface of N-doped ACs (including pyrrolic N, pyridine N and quaternary N/graphite N, and N oxides of pyridine N) depends on the temperature of heat treatment and on the nitrogen source. Although the most commonly utilized types of nitrogen end up being hydrogenated nitrogen and pyridinic nitrogen, a great number of nitrogen types are usually present in N-doped ACs which are prepared through high-temperature heat treatment (>600 ℃) or hydrothermal approach [79]. Although much work has been done to improve the application of N-doped ACs for electrochemical capacitors, it is difficult to find a straight line representing the positive changes between the capacitance of specific Cs and surface area or nitrogen content in N-Acs [80].

The most problematic issues are small size pores inaccessible for ionized solvent molecules, potential nitrogen atom polarity, and pseudo capacitance effects caused by oxygen groups of carbon-based products. In addition to that, the nature of the electrolyte, consisting of concentration, properties, and wettability to the electrodes as well, plays a crucial role in specific capacitance of N-ACs. This complexity stems from the connection of nitrogen to functional groups that are synthesized through conventional methods, which created the hindrance of distinguishing individual role of each group [81]. Besides that, the same carbon materials doped and non-doped with

nitrogen groups can hardly be prepared with the same characteristics, which in turn makes it even harder to clearly understand the practical effect of nitrogen-containing functional groups on capacitance [82]. The role of N-atoms on graphene edges which had initially suggested that this is the factor capable of causing pseudo capacitance has not yet been fully understood or confirmed, in relation to its mechanism. The strongest link between capacitance and surface groups, and the porosity of the carbon enhanced with nitrogen anodes in acidic electrolytes is also reported [83]. In addition to this, bulk gravimetric capacitance correlation was noted with the amount of basal planes whereas normalized capacitance in micropores was determined to directly depend on the dispersion of quaternary nitrogen and pyridinic-N-oxide nitrogen species mainly under increased current densities. Moreover, pyridinic and pyrrolic nitrogen were accompanied by quinone oxygen groups in the core structure of MOFs and were revealed to be the vital capacitance contributors [81]. Building on the results of such research, the further teamwork was focused on the production of "ammonia-activated non-porous carbon materials with low surface area by melamine mica composites". Along with this, those materials proved their cycle stability and capacitance that was three times higher compared to the performance of untreated composites standing for the significance of nitrogen content and surface chemistry. Nitrogen insertion by carbon-based materials, especially N-ACs, and their mutual relationship with supercapacitors is also under investigation on application performances. Materials that underwent pre-ammonia treatment produced higher nitrogen content as well as increased concentrations of pyrrole-type nitrogen-containing functional groups due to which the pseudo capacitance was improved [84]. Several investigations have disclosed that pyrrole and, sometimes, pyridine natures give rise to pseudo-capacitive effects. XPS provide evidences for this effect; binding energies could be found within the range of 398.0–400.5 eV. There are images of negative clusters of atoms, for instance pyrrolic-N and pyridinic-N, outside the structure of carbon that are linked to pseudo capacitance whereas positive clusters, such as quaternary-N and pyridine-N-oxide are proposed to contribute to electron transfer in carbon (**Figure 6**) [85].

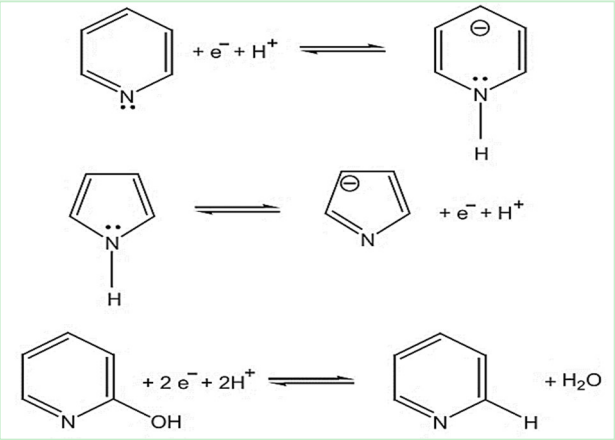

Figure 6. Illustrates potential redox reactions associated with nitrogen species of pyridinic, pyrrolic, and pyridonic types.

Nevertheless, the pseudo capacitance of quaternary-N is an area of disagreement among researchers. Some studies propose that quaternary-N can generate pseudo-

capacitance by interacting with protons in H_2SO_4 electrolyte or by the electrical double-layer formation boosting. Alternatively, some scientists suggest ions' interactions with anions in KOH electrolyte [86]. For example, in a study PPy nanospheres (PNs), carbon nanospheres (CNs), and microporous carbon nanospheres (MCNs) derived from chemical activation of CNs. MCNs, with a developed microporous structure and lower quaternary-N and pyridinic-N functionalities, exhibited significantly improved specific capacitance compared to PNs and CNs. Nitrogen-doped porous CNFs containing N-Q and N-6 displayed reversible specific capacitance in aqueous KOH electrolyte, highlighting the influence of nitrogen functionalities [87]. One of the experiments demonstrated the synthesis of N-doped CNTs (N-CNTs) via chemical vapor deposition (CVD) and the roles of pyrrolic, pyridinic, and quaternary nitrogen groups in acidic and basic electrolytes, respectively. As per their suggestion, N-Q functional groups were found to enhance capacitance through interaction with anions [88]. Intricate mechanisms of redox reactions involving N-containing functional groups were elucidated using ex situ XPS coupled cyclic voltammetry (CV) analysis, suggesting electrochemical redox reactions between pyridinic and pyridonic-N, as well as N-O and pyridinic-N [89]. A large variety of papers have been published on the review of capacitance and the porosity of NCs, but the links of the number of basic groups and capacitance is being in the shadows. The principle reason for the lower porosity and nitrogen content of the NC-based materials adopted is the considerable trouble of obtaining the ideal balance between both the high content of pores and nitrogen atoms [77]. Furthermore, other researchers reported a broad KOH activation method that allows for potassium-riched nitrogen-doped porous carbons (NPC's), so that the synthesis methods are the key for getting the functional capacitors to achieve a faster performance in charging and discharging. Because KOH weight ratio to carbon strongly affects the porosity and nitrogen content of the resulting NPCs during their manufacturing, these parameters were found to be more variable between the produced NPCs. With the KOH/carbon weight ratio being increased from 0.5 to 2, specific surface area of the NPCs also rises from 522 to 1913 m^2/g whilst the content of N decreases from 10.8% to 1.1%. Another issues present in the aging process would be the falling N/P ratio which leads to a decline of the pyridinic-N content and an increase of the pyrrolic/pyridonic-N, quaternary-N, and pyridine-N-oxide content [90].

Additionally, nitrogen content per unit weight reduced at high KOH/NPC ratio but pyridinic-N and pyrrolic/pyridonic-N namely stayed dominant anyhow in all synthesized NPCs. The electrochemical tests showed that NPC-1, was made with a low amount of KOH: carbon ratio of 1.0 and had the higher specific capacitance at 363 F/g that was tested at the current density of 0.1 A/g in aaqueous electrolyte with 1M H_2SO_4. The authors expected this to do something highlighting their success to contribute it to factors such as the greater specific surface area of NPC-1 compared to NPC-0.5 and the higher nitrogen content of NPC-1 compared to NPC-2. The jointly arising tight double-layer capacitance and extra pseudo capacitance are responsible for the system of NPC-1 having the highest specific capacitance [91].

Again, the method of KOH activation was used to prepare NCNPs with hierarchical porous N-doped carbons as the second instance. The capacitance that measured the specific area, rise with the growth in the specific surface areas, and

capacitance normalized by specific surface area (CA = cm/S_{BET}), increase with nitrogen content mol % (represents the concentration of a component in a mixture, calculated as moles of component per 100 moles) [92]. Similar patterns were observed in the hierarchically porous, nitrogen-doped carbon nanotubes (NCNTs) generated from the KOH activation of those NCNTs retrieved from the polyaniline nanotubes. Under the identical nitrogen composition, the calculations of specific capacitance were near similar, reflecting the changes in surface area only to the certain degree [93]. The above findings thus establish an intricate connection between the role of porosity, nitrogen content and electrochemical performance in nitrogen-doped carbon material, highlighting the importance of having an intimate control over synthesis parameters for achieving the highest specific capacitance in supercapacitor applications [45]. The effects of carbonization temperature on N content, pore structure and surface area are known, and also the influence on specific capacitance (Csp) is well understood [94]. This could be illustrated through nitrogen doped graphitic porous carbon nanofibers (CNFs) acquired from carbonaceous nanofibers coated with polypyrrole (CNFs@PPy) at different temperatures (ranging from 500 to 1100 ℃) which exhibited the highest pseudocapacitance at 900 ℃ [95]. Such high pseudo capacitance was the result of a synergized effect: both nitrogen doping that rendered new carbon species as having better electron donor/acceptor characteristics and a high BET surface area that enhanced the electolyte ion transportion [96]. The same trends observed in nitrogen-enriched carbon nanowires produced directly from the polypropylene aniline nanofibers using elevated temperatures (started at 600 ℃ and reaching 900 ℃) upon calcination resulted in a decrease in the nitrogen content at increased calcination temperatures. The samples had the highest specific capacity at 700 ℃ because of the fact that the surfaces area was balanced in its proportion with the nitrogen grown [90]. It has also been reported that smaller pores diameter in the porous carbon spheres administrate higher capacitance and faster rate compare to the larger spheres which having similar surface area. This is due to the less resistance in masses and to charge transfer, the rise in the EDLC performance, and a better way by which the pores are inaccessible to the aqueous electrolyte [97].

Nitrogen-dope carbon structure (NC) is also associated with specific capacitance and rate performance action. The same impurity (nitrogen) of carbon nanoparticles (NCNPs), carbon nanotubes (NCNTs), and carbon nanowires (NCNWs) derived from aniline under various treatment conditions resulted in different electrochemical performances. Varying parameters like smaller particles size, appropriate pore size distribution are keeping a nitrogen functionalities were found to be contributors of better specific capacitances [98]. The selection of electrolyte is also an essential factor for the specific capacitance of dielectrics [77]. For example, in one study, NCs doped by KOH showed improved power output when the acidic based electrolytes were used instead of the basic ones [99]. and the main reason is referred to the fact that carbon surface is markedly more basic in the presence of nitrogen. Next, carbon gels created from the gelatin biomolecules showed that there was higher specific capacitance in the acidic H_2SO_4 solution compared to the basic KOH solution (**Figure 7**). This proves that the type of electrolyte can be changed by the use of pseudo capacitance [77].

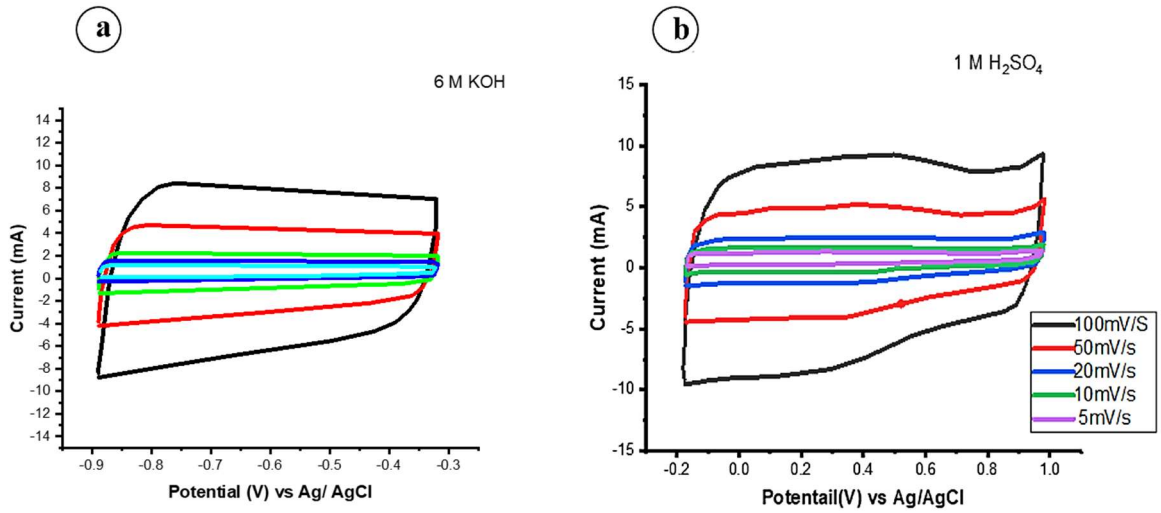

Figure 7. Illustrates the electrochemical capacitive behavior of Nano catalysts (NCs) in 6 M KOH (left column) and 1 M H_2SO_4 (right column) aqueous solutions using a three-electrode configuration. Panels **(a)** and **(b)** present cyclic voltammograms recorded at different sweep rates. Reproduced by permission from Ref [100].

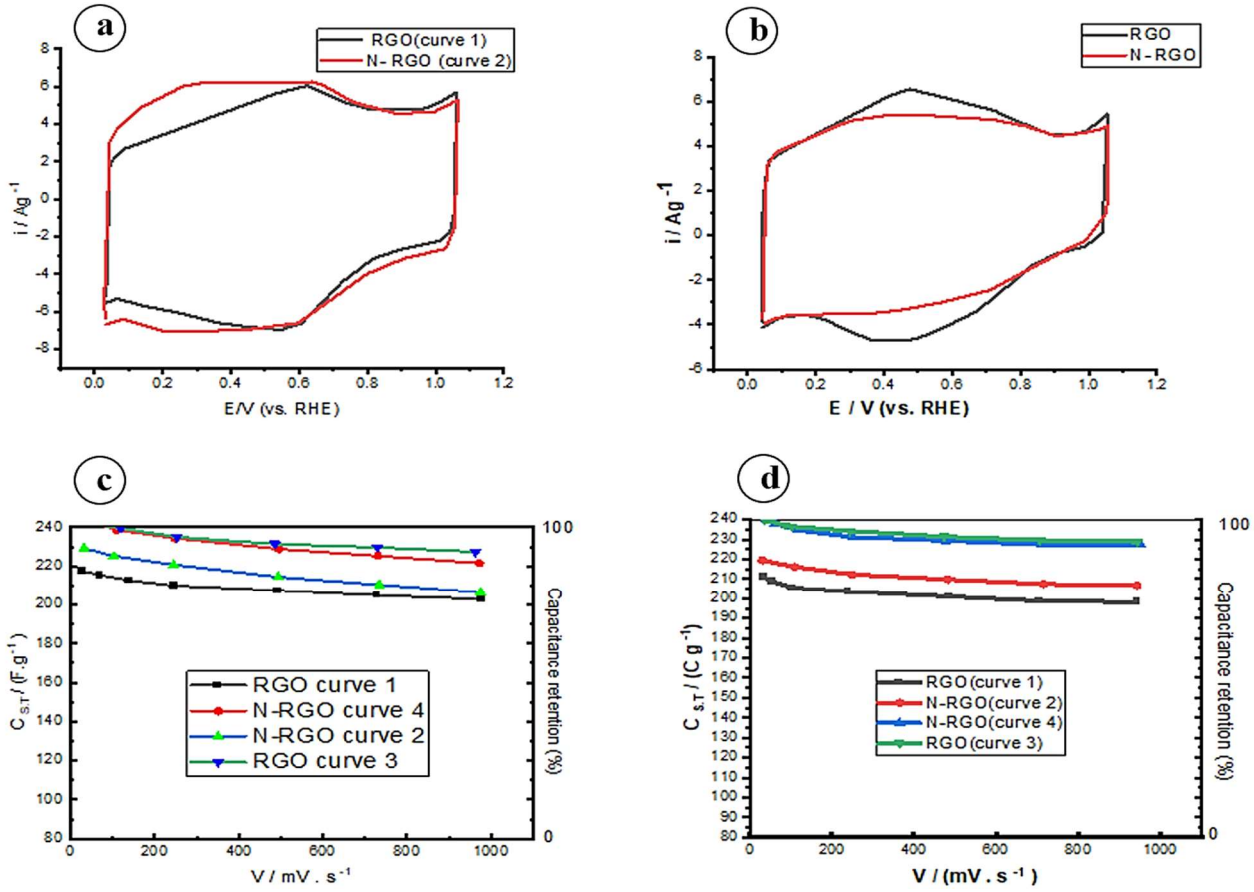

Figure 8. Displays cyclic voltammograms recorded in **(a)** 1 M H_2SO_4; **(b)** KOH at a sweep rate of 25 mV/s; and the total specific capacitance ($C_{S,T}$) and capacitance retention (calculated based on the value obtained at 25 mVs^{-1}) against the scan rate of the cyclic voltammetry (CV) for Reduced Graphene Oxide (rGO) and Nitrogen-Doped Reduced Graphene Oxide (N-rGO) in. **(c)** H_2SO_4; **(d)** KOH. Reproduced by permission from Ref [101].

These works assemble present together the intricate interplay of synthesis factors, carbonization process, composition, and electrolyte selection in dictating the

electrochemical behavior of nitrogen functionalized carbon materials for super capacitors. The application of a technique termed microwave-assisted hydrothermal synthesis include N-doped rGO and rGO [88]. This study intends to explore nitrogen-based functional groups (N-N and N-O) contribution to the specific capacitance, which depends on the nature of electrolytes (aqueous and non-aqueous). It was discovered that pseudo capacitance was increased mainly by pyridinic-N and pyrrolic-N/pyridonic-N in the acidic medium, as confirmed by the electrochemical studies using alkaline (1 M KOH) and acidic (1 M H_2SO_4) electrolytes (**Figure 8**). Due to double-layer capacity effect of N-rGO in H_2SO_4 that is higher than that in KOH, there are some N-containing groups that enhance the densities of electronic charges of graphene and aid in the adsorption of protons in the acidic electrolyte [88].

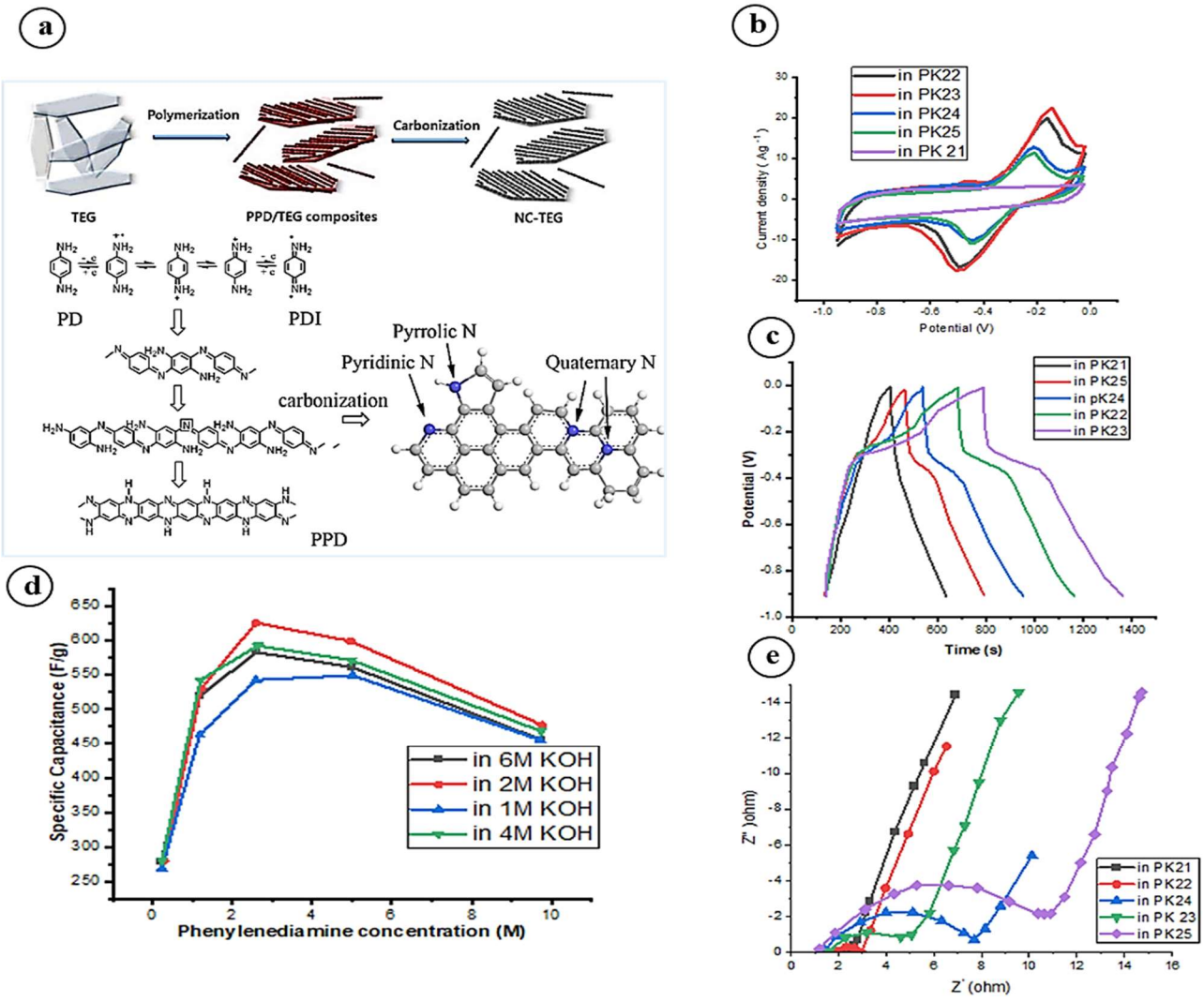

Figure 9. (a) Illustration of the preparation of NC-TEG. Reprinted by permission from Ref [103]. **(b)** cyclic voltammetry curves; **(c)** galvanic charge-discharge of the NC-TEG electrode under various concentrations of PD mediator in a 2 M KOH solution. Additionally, **(d)** compares the capacitance in different electrolytes, and **(e)** presents the electrochemical impedance spectroscopy (EIS) spectrum of NC-TEG with varying PD concentrations [103].

Contradictory results regarding specific capacitance in acidic versus basic electrolytes have been reported in the literature. Some studies demonstrated higher specific capacitance in acidic electrolytes, while others observed superior performance

in basic electrolytes. For instance, in a research study, 3-D SACFO carbon films of chicken eggshell membranes were developed, which showed higher specific capacitance in KOH than H_2SO_4. Furthermore, it was also determined that the capacity of the N-doped CNTs immersed in the KOH had greater specific capacitance than the ones which were dipped in the H_2SO_4 solution, which shows the importance of selecting an appropriate electrolyte [102]. The effect of nitrogen placeholders on specific capacity in distinct pH solutions is complex in nature and the consequent findings that are released in the literature vary. Continuing work is required to effectively complete the mechanism and further down the line innovative strategies may have to be applied in order to develop the complexity concept in the nitrogen-doping carbons. Yet, besides that, they study how different components of the electrolyte influence the capacitance. The authors demonstrated enhanced faradaic behavior through the epitaxial expression of a nitrogen doped carbon based layer embedded on thermally exfoliated graphene (NC-TEG) and Quinone insertion in the electrolyte into the electronic conductor (PD) (**Figure 9a**). The redox-activity peaks were dominantly observed in a cyclic voltammetry after the incorporation of PD (**Figure 9b**). suggesting a pseudo-capetic behavior. NC-SC epitomized tech using capacitor and exhibit gradual rise of the specific capacitance with addition of Pd, and reached its maximum specific capacitance in the mixed electrolyte (2 M KOH with 0.025 M Pd) and then showed a downward trend in the electrolyte with higher Pd concentration (**Figure 9d–e**). This study emphasized the importance of electrical composition alongside that of nitrogen as the doping agent in determining the performance of the electrolyte in the capacitive behavior of the carbon Nano-materials [103].

Lastly, the loading mass onto electrodes was discussed as a factor affecting specific capacity and rate performance. In general, an augmentation in loading mass typically leads to a reduction in specific capacity and rate performance. However, limited studies have been dedicated to exploring this aspect specifically in the context of nitrogen-doped carbon electrodes for batteries and capacitors.

4.3.2. Batteries

In an experimental work, Fe_3O_4 was synthesized into nitrogen-doped carbon and acted as a nano-capsule structure with self-filled channels. The Fe_3O_4@NC electrode was compared cycling and rate capabilities with the unmodified Fe_2O_3 electrode, and it exhibited superiority in both aspects. It was shown to function better and it had better stability particularly at high current densities as shown in **Figure 10a**,**b**. In addition, the ability of the Fe_3O_4@NC anode to be utilized in lithium-ion batteries (LIBs) over a long time was proved to be 480 mAh/g at a high charging density of 20 A/g over 1000 This average was designed to be consistently at 99.9% Coulombic efficiency. With much lower current density of 5 A/g, the reversible capacity attained 873 mAh/g, as **Figure 10c** shows [104].

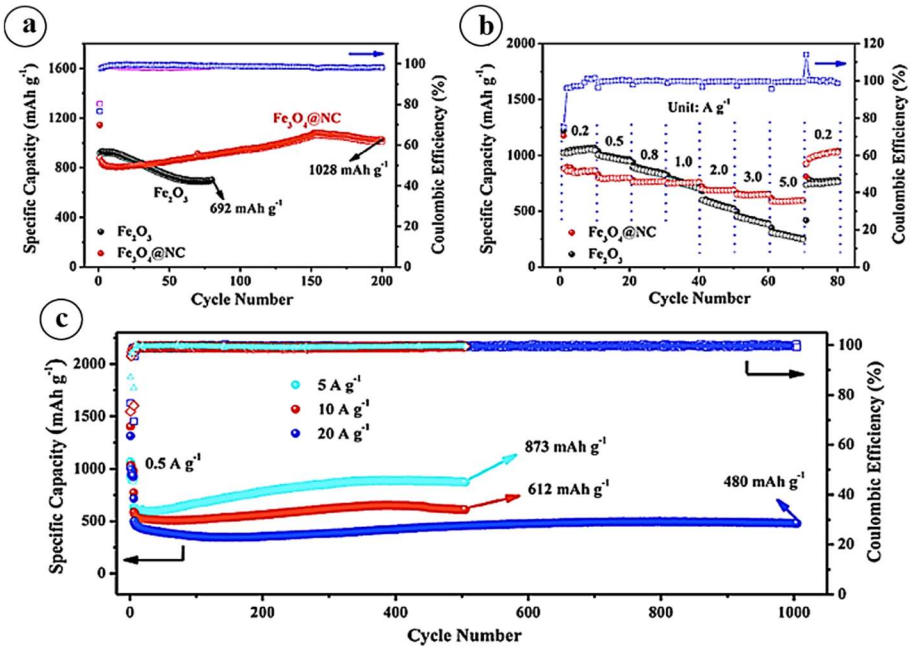

Figure 10. Illustrates the electrochemical performance of Fe_3O_4@NC and Fe_2O_3 as anodes in lithium-ion batteries (LIBs). **(a)** the cycling performances at a current density of 500 mA/g are presented; **(b)** showcases the rate performances of both materials in a half-cell configuration against Li/Li^+. Additionally, **(c)** provides insights into the cycling performance of the Fe_3O_4@NC anode under different current densities (5, 10, and 20 A/g) throughout 1000 cycles. This comprehensive analysis offers a detailed perspective on how these materials perform in terms of cycling stability and rate capabilities in the context. of LIBs. Reprinted by permission from Ref [49].

Moreover, Fe_3O_4@NC anode proved to be practical for high-eating applications, finished to the full charge within 2 min. This implicates the fact that Fe_3O_4@NC nanocarriers is in fact relevant to cases when the current charging is quick [104]. Another research worked on the formation of hollow iron oxide/carbon core-shell nanostructures for lithium ion battery (LIB). To achieve this synthesis, we dealt with Fe_2O_3@polydopamine nanocomposites from the Fe_2O_3 nanotubes and dopamine hydrochloride precursors. Lastly, compositing of Fe_3O_4@N-doped C was accomplished by controlling the carbonization process. In the last step of the Fabrication a series of experiments with Fe_3O_4@void@N-doped C-x composites differing in the void sizes was carried out by etching off Fe_3O_4. The work was performed by investigating the impact of changing etching time on void size. In the electrochemical assessment of LIBs, the sample was the best at 5 Volt for 5 h of etchant when a 2 moles/L HCl acid mixture was used and heated at 30 degrees centigrade. The Fe_3O_4@void@ N-Doped C-5 is capable of holding up to 1222 mAh/g after it was discharged at a rate of 200 mAh/g up to 100 cycles [105]. As a separate venture, gallium (Ga) was probed to be a candidate of self-healing anode component. Scientists brought into use a Ga–Sn liquid metal alloy with auto-healing features and wonderful energy and chemical performance applicable with alkali ion battery production. Lips-Ga_2O_3@nitrogen-doped carbon quantum dot (H–Ga_2O_3@N-CQD) nanospheres as a material for lithium ion batteries (LIB's) anode were developed. An

electrode eventually acquired a bulky size with the capacity of 1348.5 mAh/g at 0.1 A/g and after 500 cycles it was able to hold up to the reversible capacity of 700.5 mAh/g under 0.5 A/g [106]. In a similar way, nitrogen-doped porous carbon (NCFC) is obtained from silk cocoon and was used as the cathode (in combination with an ionic liquid) for Li-O_2 batteries. The irregular surface of the NCFC characterized by bending slices demonstrated advanced speci0c discharge product with more efficient sites available for electrochemical reactions. The Li-O_2 battery functionalized with NCFC is an excellent choice with a high energy efficiency and stability at various current densities surpassing carbon black super P Li-O_2 batteries in terms of the cycle life and over potential. As seen from these results, this compound seems to perform to Li-O_2 batteries and it is certain to be an excellent material for this kind of batteries [107]. This study highlighted that the performance of the electrochemical application improves by adding N through the doping process. Study can be considered as a successful one since increased porosity, surface area and the N moieties preservation were determined without NH3 removal. The modified PN-HCN with superior is an effect I-S batteries cathode host. It has reached the minimum theoretical capacity of 1620 mAh/g with the highest rate capability and longest cycling stability, which is 789 mAh/g at 0.5C after cycling 200 times Our results show that PN-HCN has not only enhanced performance but also produced surprising results seen in the three comparisons (**Figure 11a–c**). CV-HCN at different current densities (0.05, 0.1, 0.5, 0.8, and 1.0 A/g) is displayed in **Figure 11d**, showing a symmetric signature, which as a good reversibility sign [108].

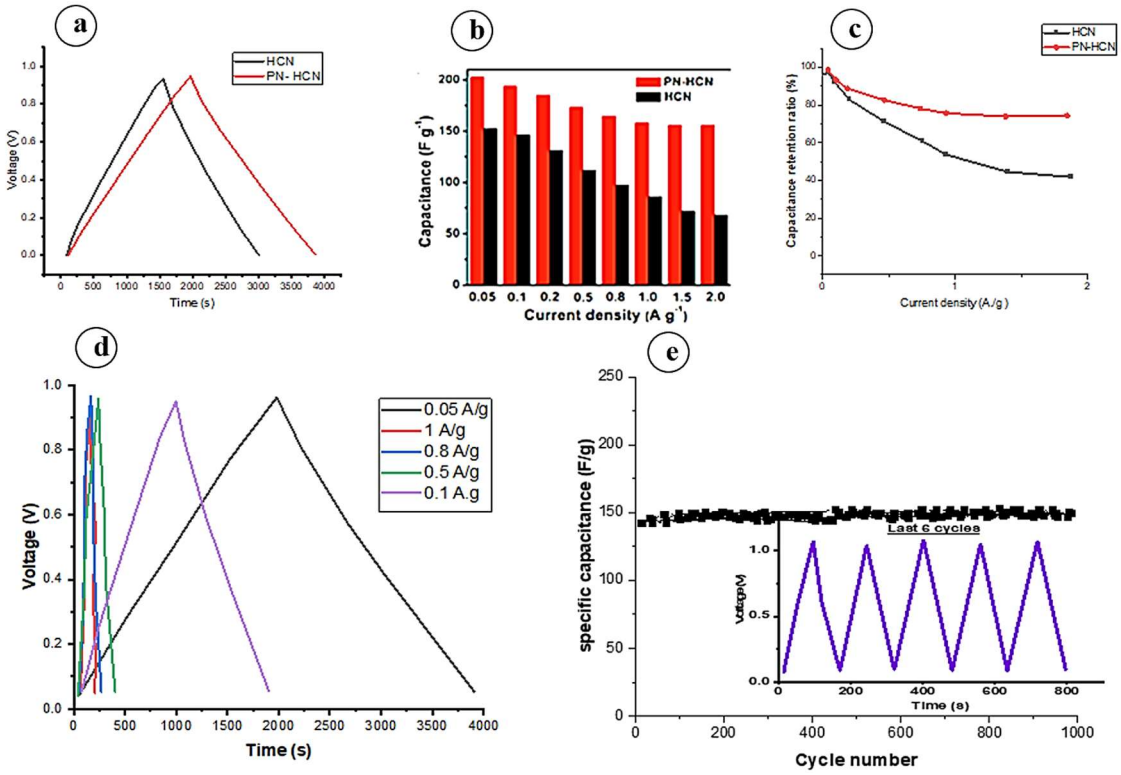

Figure 11. (a) GCD profile at 0.05 A.g; **(b)** Graphing the specific capacitances and current density; **(c)** Chart displaying the capacitance retention and current density for PN-HCN and HCN; **(d)** GCD profiles of PN-HCN at different current densities from 0.05 to 1.0 A.g; and **(e)** Cycling response of PN. Reproduced by permission from Ref [108].

In the course of cycling above 10,000 cycles PN-HCN has shown excellent cycling stability characterized by the high specific capacitance of 170 F/g, which remains stable and almost the same through such a long cycling (**Figure 11e**).The deliberate structural integration of enhanced porosity, well-maintained N functionality, and a precisely defined nanoscale hollow spherical structure underscores the importance and effectiveness of PN-HCN in enhancing electrochemical performance in Li–S batteries and supercapacitors compared to HCN without NH3 treatment [108]. Another remarkable experiment is in the list of other scientific analysis, where scientists have pointed out some ameliorations in the area of conductivity inhibition. N-doping is a tool that helps to increase the electrical conductivity of the carbon materials. It can actually be compared with electron facilitation in charge and discharge cycles. This is an indispensable element that leads to increasing the overall battery´s workflow. We should also add that nitrogen adsorbed carbon materials participate in the strength and stability increase of the battery, which provides a longer and more feasible work during repetitive charging and discharging [109]. The nitrogen doping causes a large surface expansion and thereby increased active points for action of electrochemical reactions. Thus, within the structure of a battery, these ions can circulate in a confined space allowing for a greater capacity and enhanced storage performance [109]. Besides this, the presence of elements such as nitrogen also allows for the ions to perform effective diffusion within the electrode making the batteries operate faster and the performances better [13]. In different battery types including lithium-ion batteries, sodium-ion batteries, and metal-ion batteries, the Nitrogen-doped carbon materials exhibited their versatility. These features are the evidences of their flexibility which is applied in numerous energy storage systems [110].

5. Conclusion

Nitrogen-doped activated carbon represents a multifaceted solution with profound implications across various domains, underscoring its pivotal role in advancing sustainable practices and addressing pressing environmental challenges.

1) The importance of production of nitrogen-doped activated carbon from plant waste and sustainability in green production cannot be overstated. By utilizing biomass-derived sources such as licorice residue, duck rice husk, walnut shell, feathers, and tea waste, the production process becomes not only cost-effective but also environmentally friendly. This approach not only mitigates waste but also aligns with the principles of circular economy, contributing to a greener and more sustainable future.

2) The significance of nitrogen-doped activated carbon in the adsorption of CO_2 is paramount. Through the interaction between nitrogen and carbon, complex and highly porous structures are formed, greatly enhancing their efficacy in capturing carbon dioxide from various sources. This capability holds immense promise in combating climate change by reducing greenhouse gas emissions and mitigating the adverse effects of global warming.

3) The importance and utilization of nitrogen-doped activated carbon for energy storage in different types, including supercapacitors and batteries, highlight its versatility and potential in the realm of energy storage technologies. From hollow

carbon nanospheres to carbon materials derived from Metal-Organic Frameworks (MOFs), nitrogen-doped activated carbon exhibits superior performance and long-term stability, making it an attractive candidate for next-generation energy storage devices. Furthermore, its catalytic properties and ability to enhance electrode materials in LIBs and ZIBs offer exciting avenues for further exploration and innovation in the pursuit of sustainable energy solutions.

Nitrogen-doped activated carbon stands as a beacon of hope in the quest for a more sustainable and environmentally conscious future. Its production from plant waste, efficacy in CO_2 adsorption, and utilization in energy storage applications underscore its transformative potential in driving the transition towards greener practices and mitigating the impacts of climate change.

Conflict of interest: The authors declare no conflict of interest.

Nomenclature

N-ACs	Nitrogen doped Activated Carbons
MOFs	Metal Organic Frameworks
CVD	Chemical Vapor Deposition
BET	Brunauer-Emmett-Teller
Cs	Specific Capacity
MR-GO	Melamine-resorcinol-formaldehyde Resin/Graphene oxide
PACP	Poly Aniline-Co-Pyrrole
mAh/g	Specific capacity of a battery or an electrode material in energy storage devices (milliAmpere-hour per gram of active material)
A/g	Current density in electrochemical systems or devices (ampere/ gram of active material)
XPS	X-ray Photoelectron Spectroscopy
CNs	Carbon Nanospheres
MCNs	Microporouse Carbon Nanospheres
PNs	Ppy nanospheres
CNFs	Carbon Nano Fibers
N-CNTs	Nitrogen doped Carbon Nano Tubes
NPCs	Nitrogen doped porous Carbons
NCNPs	Nitrogen doped Carbon Nano Particles
NC-TEG	Nitrogen doped Carbon based layer embedded Thermally Exfoliated Graphene
LIBs	Lithium Ion Batteries
PN-HCNs	Porous Nitrgeoon doped Hollow Carbon Nanoshphers

References

1. He S, Chen G, Xiao H, et al. Facile preparation of N-doped activated carbon produced from rice husk for CO_2 capture. Journal of Colloid and Interface Science. 2021; 582: 90-101. doi: 10.1016/j.jcis.2020.08.021
2. Wang J, Pu Q, Ning P, et al. Activated carbon-based composites for capturing CO_2: a review. Greenhouse Gases: Science and Technology. 2021; 11(2): 377-393. doi: 10.1002/ghg.2051
3. Sivadas DL, Vijayan S, Rajeev R, et al. Nitrogen-enriched microporous carbon derived from sucrose and urea with superior CO2 capture performance. Carbon. 2016; 109: 7-18. doi: 10.1016/j.carbon.2016.07.057
4. Abd AA, Othman MR, Kim J. A review on application of activated carbons for carbon dioxide capture: present performance, preparation, and surface modification for further improvement. Environmental Science and Pollution Research. 2021;

28(32): 43329-43364. doi: 10.1007/s11356-021-15121-9
5. Xu B, Zheng D, Jia M, et al. Nitrogen-doped porous carbon simply prepared by pyrolyzing a nitrogen-containing organic salt for supercapacitors. Electrochimica Acta. 2013; 98: 176-182. doi: 10.1016/j.electacta.2013.03.053
6. Wang M, Fan X, Zhang L, et al. Probing the role of O-containing groups in CO_2 adsorption of N-doped porous activated carbon. Nanoscale. 2017; 9(44): 17593-17600. doi: 10.1039/c7nr05977a
7. Abuelnoor N, AlHajaj A, Khaleel M, et al. Activated carbons from biomass-based sources for CO_2 capture applications. Chemosphere. 2021; 282: 131111. doi: 10.1016/j.chemosphere.2021.131111
8. Malini K, Selvakumar D, Kumar NS. Activated carbon from biomass: Preparation, factors improving basicity and surface properties for enhanced CO_2 capture capacity – A review. Journal of CO_2 Utilization. 2023; 67: 102318. doi: 10.1016/j.jcou.2022.102318
9. Sharma A, Jindal J, Mittal A, et al. Carbon materials as CO_2 adsorbents: a review. Environmental Chemistry Letters. 2021; 19(2): 875-910. doi: 10.1007/s10311-020-01153-z
10. Saha D, Kienbaum MJ. Role of oxygen, nitrogen and sulfur functionalities on the surface of nanoporous carbons in CO_2 adsorption: A critical review. Microporous and Mesoporous Materials. 2019; 287: 29-55. doi: 10.1016/j.micromeso.2019.05.051
11. Hassan MF, Sabri MA, Fazal H, et al. Recent trends in activated carbon fibers production from various precursors and applications—A comparative review. Journal of Analytical and Applied Pyrolysis. 2020; 145: 104715. doi: 10.1016/j.jaap.2019.104715
12. Ghosh A, Ghosh S, Seshadhri GM, et al. Green synthesis of nitrogen-doped self-assembled porous carbon-metal oxide composite towards energy and environmental applications. Scientific Reports. 2019; 9(1). doi: 10.1038/s41598-019-41700-5
13. Al-Hajri W, De Luna Y, Bensalah N. Review on Recent Applications of Nitrogen-Doped Carbon Materials in CO2 Capture and Energy Conversion and Storage. Energy Technology. 2022; 10(12). doi: 10.1002/ente.202200498
14. Heidarinejad Z, Dehghani MH, Heidari M, et al. Methods for preparation and activation of activated carbon: a review. Environmental Chemistry Letters. 2020; 18(2): 393-415. doi: 10.1007/s10311-019-00955-0
15. Zhou Y, Tan P, He Z, et al. CO_2 adsorption performance of nitrogen-doped porous carbon derived from licorice residue by hydrothermal treatment. Fuel. 2022; 311: 122507. doi: 10.1016/j.fuel.2021.122507
16. Wang J, Kaskel S. KOH activation of carbon-based materials for energy storage. Journal of Materials Chemistry. 2012; 22(45): 23710. doi: 10.1039/c2jm34066f
17. Tan X, Liu S, Liu Y, et al. Biochar as potential sustainable precursors for activated carbon production: Multiple applications in environmental protection and energy storage. Bioresource Technology. 2017; 227: 359-372. doi: 10.1016/j.biortech.2016.12.083
18. Serafin J, Kishibayev K, Tokpayev R, et al. Functional Activated Biocarbons Based on Biomass Waste for CO_2 Capture and Heavy Metal Sorption. ACS Omega. 2023; 8(50): 48191-48210. doi: 10.1021/acsomega.3c07120
19. Wang Y, Hu X, Guo T, et al. Efficient CO_2 adsorption and mechanism on nitrogen-doped porous carbons. Frontiers of Chemical Science and Engineering. 2020; 15(3): 493-504. doi: 10.1007/s11705-020-1967-0
20. Tan Y, Wang X, Song S, et al. Preparation of Nitrogen-Doped Cellulose-Based Porous Carbon and Its Carbon Dioxide Adsorption Properties. ACS Omega. 2021; 6(38): 24814-24825. doi: 10.1021/acsomega.1c03664
21. Laksaci H, Khelifi A, Belhamdi B, et al. Valorization of coffee grounds into activated carbon using physic—chemical activation by KOH/CO_2. Journal of Environmental Chemical Engineering. 2017; 5(5): 5061-5066. doi: 10.1016/j.jece.2017.09.036
22. Chang B, Shi W, Yin H, et al. Poplar catkin-derived self-templated synthesis of N-doped hierarchical porous carbon microtubes for effective CO_2 capture. Chemical Engineering Journal. 2019; 358: 1507-1518. doi: 10.1016/j.cej.2018.10.142
23. Sattayarut V, Wanchaem T, Ukkakimapan P, et al. Nitrogen self-doped activated carbons via the direct activation of Samanea samanleaves for high energy density supercapacitors. RSC Advances. 2019; 9(38): 21724-21732. doi: 10.1039/c9ra03437d
24. Ruan W, Wang Y, Liu C, et al. One-step fabrication of N-doped activated carbon by NH3 activation coupled with air oxidation for supercapacitor and CO_2 capture applications. Journal of Analytical and Applied Pyrolysis. 2022; 168: 105710. doi: 10.1016/j.jaap.2022.105710

25. Fan P, Ren J, Pang K, et al. Cellulose-Solvent-Assisted, One-Step Pyrolysis to Fabricate Heteroatoms-Doped Porous Carbons for Electrode Materials of Supercapacitors. ACS Sustainable Chemistry & Engineering. 2018; 6(6): 7715-7724. doi: 10.1021/acssuschemeng.8b00589
26. Pastor-Villegas J, & Durán-Valle CJ. Pore structure of activated carbons prepared by carbon dioxide and steam activation at different temperatures from extracted rockrose. Carbon N. Y. 2002; 40(3): 397-402. doi: 10.1016/S0008-6223(01)00118-X
27. Lee SK, Han SW, Cha GY, et al. Base-type nitrogen doping in zeolite-templated carbon for enhancement of carbon dioxide sorption. Journal of CO_2 Utilization. 2022; 62: 102084. doi: 10.1016/j.jcou.2022.102084
28. Fu N, Wei HM, Lin HL, et al. Iron Nanoclusters as Template/Activator for the Synthesis of Nitrogen Doped Porous Carbon and Its CO_2 Adsorption Application. ACS Applied Materials & Interfaces. 2017; 9(11): 9955-9963. doi: 10.1021/acsami.6b15723
29. Varghese SM, Chowdhury AR, Arnepalli DN, et al. Delineating the effects of pore structure and N-doping on CO_2 adsorption using coco peat derived carbon. Carbon Trends. 2023; 10: 100250. doi: 10.1016/j.cartre.2023.100250
30. Ouyang L, Xiao J, Jiang H, et al. Nitrogen-Doped Porous Carbon Materials Derived from Graphene Oxide/Melamine Resin Composites for CO_2 Adsorption. Molecules. 2021; 26(17): 5293. doi: 10.3390/molecules26175293
31. Qiao Y, Wu C. Nitrogen enriched biochar used as CO_2 adsorbents: a brief review. Carbon Capture Science & Technology. 2022; 2: 100018. doi: 10.1016/j.ccst.2021.100018
32. Zhang H, Zheng Y, Cui Y. Melamine assisted preparation of nitrogen doped activated carbon from sustainable biomass for H_2 and CO_2 storage. International Journal of Hydrogen Energy. 2023; 48(47): 17914-17922. doi: 10.1016/j.ijhydene.2023.01.269
33. Wei Q, Tong X, Zhang G, et al. Nitrogen-Doped Carbon Nanotube and Graphene Materials for Oxygen Reduction Reactions. Catalysts. 2015; 5(3): 1574-1602. doi: 10.3390/catal5031574
34. Chiang YC, Hsu WL, Lin SY, et al. Enhanced CO_2 Adsorption on Activated Carbon Fibers Grafted with Nitrogen-Doped Carbon Nanotubes. Materials. 2017; 10(5): 511. doi: 10.3390/ma10050511
35. Jin B, Li J, Wang Y, et al. Nitrogen doping and porous tuning carbon derived from waste biomass boosting for toluene capture: Experimental study and density functional theory simulation. Chemical Engineering Journal Advances. 2022; 10: 100276. doi: 10.1016/j.ceja.2022.100276
36. Liu L, Deng QF, Hou XX, et al. User-friendly synthesis of nitrogen-containing polymer and microporous carbon spheres for efficient CO_2 capture. Journal of Materials Chemistry. 2012; 22(31): 15540. doi: 10.1039/c2jm31441j
37. Rashidi NA, Yusup S. Recent methodological trends in nitrogen–functionalized activated carbon production towards the gravimetric capacitance: A mini review. Journal of Energy Storage. 2020; 32: 101757. doi: 10.1016/j.est.2020.101757
38. Rajak R, Saraf M, Mobin SM. Robust heterostructures of a bimetallic sodium–zinc metal–organic framework and reduced graphene oxide for high-performance supercapacitors. Journal of Materials Chemistry A. 2019; 7(4): 1725-1736. doi: 10.1039/c8ta09528k
39. Wu YF, Liu D, Sung YS, et al. Effects of carbonization temperature on fabricating carbonized Universitetet i Oslo-66 as active materials for supercapacitors. Journal of Solid State Chemistry. 2022; 314: 123439. doi: 10.1016/j.jssc.2022.123439
40. Skorupska M, Ilnicka A, Lukaszewicz JP. N-doped graphene foam obtained by microwave-assisted exfoliation of graphite. Scientific Reports. 2021; 11(1). doi: 10.1038/s41598-021-81769-5
41. Jain A, Balasubramanian R, Srinivasan MP. Hydrothermal conversion of biomass waste to activated carbon with high porosity: A review. Chemical Engineering Journal. 2016; 283: 789-805. doi: 10.1016/j.cej.2015.08.014
42. Blicher A, Kalish IH, Brennan KF. Field-Effect Transistors. Encyclopedia of Physical Science and Technology. Published online 2003: 831-849. doi: 10.1016/b0-12-227410-5/00242-8
43. Gopalakrishnan A, Badhulika S. Effect of self-doped heteroatoms on the performance of biomass-derived carbon for supercapacitor applications. Journal of Power Sources. 2020; 480: 228830. doi: 10.1016/j.jpowsour.2020.228830
44. Zhang X, Zhang S, Yang H, et al. Effects of hydrofluoric acid pre-deashing of rice husk on physicochemical properties and CO_2 adsorption performance of nitrogen-enriched biochar. Energy. 2015; 91: 903-910. doi: 10.1016/j.energy.2015.08.028
45. Zhou M, Pu F, Wang Z, et al. Nitrogen-doped porous carbons through KOH activation with superior performance in supercapacitors. Carbon. 2014; 68: 185-194. doi: 10.1016/j.carbon.2013.10.079
46. Thote JA, Iyer KS, Chatti R, et al. In situ nitrogen enriched carbon for carbon dioxide capture. Carbon. 2010; 48(2): 396-402. doi: 10.1016/j.carbon.2009.09.042

47. Balou S, Babak SE, Priye A. Synergistic Effect of Nitrogen Doping and Ultra-Microporosity on the Performance of Biomass and Microalgae-Derived Activated Carbons for CO_2 Capture. ACS Applied Materials & Interfaces. 2020; 12(38): 42711-42722. doi: 10.1021/acsami.0c10218
48. Wang Y, Xiao J, Wang H, et al. Binary doping of nitrogen and phosphorus into porous carbon: A novel di-functional material for enhancing CO_2 capture and super-capacitance. Journal of Materials Science & Technology. 2022; 99: 73-81. doi: 10.1016/j.jmst.2021.05.035
49. Duan H, Zhang S, Chen Z, et al. Self-Formed Channel Boosts Ultrafast Lithium Ion Storage in Fe3O4@Nitrogen-Doped Carbon Nanocapsule. ACS Applied Materials & Interfaces. 2019; 12(1): 527-537. doi: 10.1021/acsami.9b16184
50. Islam MS, Faisal SN, Tong L, et al. N-doped reduced graphene oxide (rGO) wrapped carbon microfibers as binder-free electrodes for flexible fibre supercapacitors and sodium-ion batteries. Journal of Energy Storage. 2021; 37: 102453. doi: 10.1016/j.est.2021.102453
51. Guo T, Zhang Y, Chen J, et al. Investigation of CO_2 adsorption on nitrogen-doped activated carbon based on porous structure and surface acid-base sites. Case Studies in Thermal Engineering. 2024; 53: 103925. doi: 10.1016/j.csite.2023.103925
52. Zhang D, Wei Q, Huang H, et al. Ambient-Condition Strategy for Production of Hollow Ga2O3@rGO Crystalline Nanostructures Toward Efficient Lithium Storage. Energy & Environmental Materials. 2023; 7(2). doi: 10.1002/eem2.12585
53. Liu D, Yuan X, Yu J, et al. Chitosan gel synthesis nitrogen-doped porous carbon as electrode materials for supercapacitors. Journal of Dispersion Science and Technology. 2021; 43(12): 1872-1879. doi: 10.1080/01932691.2021.1880930
54. Xu F, Ding B, Qiu Y, et al. Hollow Carbon Nanospheres with Developed Porous Structure and Retained N Doping for Facilitated Electrochemical Energy Storage. Langmuir. 2019; 35(40): 12889-12897. doi: 10.1021/acs.langmuir.8b03973
55. Liang T, Chen C, Li X, et al. Popcorn-Derived Porous Carbon for Energy Storage and CO_2 Capture. Langmuir. 2016; 32(32): 8042-8049. doi: 10.1021/acs.langmuir.6b01953
56. Taurbekov A, Abdisattar A, Atamanov M, et al. Investigations of Activated Carbon from Different Natural Sources for Preparation of Binder-Free Few-Walled CNTs/Activated Carbon Electrodes. Journal of Composites Science. 2023; 7(11): 452. doi: 10.3390/jcs7110452
57. Yang X, He C, Qiu Y, et al. Electrochemical sensing based on biomass-derived, hierarchical, porous carbon for simultaneous detection of dopamine and uric acid. Materials Chemistry and Physics. 2022; 292: 126825. doi: 10.1016/j.matchemphys.2022.126825
58. Parveen N, Al-Jaafari AI, Han JI. Robust cyclic stability and high-rate asymmetric supercapacitor based on orange peel-derived nitrogen-doped porous carbon and intercrossed interlinked urchin-like $NiCo_2O_4$@3DNF framework. Electrochimica Acta. 2019; 293: 84-96. doi: 10.1016/j.electacta.2018.08.157
59. Iwanow M, Gärtner T, Sieber V, et al. Activated carbon as catalyst support: precursors, preparation, modification and characterization. Beilstein Journal of Organic Chemistry. 2020; 16: 1188-1202. doi: 10.3762/bjoc.16.104
60. Al-Hajri W, De Luna Y, Bensalah N. Review on Recent Applications of Nitrogen-Doped Carbon Materials in CO_2 Capture and Energy Conversion and Storage. Energy Technology. 2022; 10(12). doi: 10.1002/ente.202200498
61. Gong F, Li H, Wang W, et al. Scalable, eco-friendly and ultrafast solar steam generators based on one-step melamine-derived carbon sponges toward water purification. Nano Energy. 2019; 58: 322-330. doi: 10.1016/j.nanoen.2019.01.044
62. Yu Q, Bai J, Huang J, et al. One-Pot Synthesis of N-Rich Porous Carbon for Efficient CO_2 Adsorption Performance. Molecules. 2022; 27(20): 6816. doi: 10.3390/molecules27206816
63. Mahajan S, Lahtinen M. Recent progress in metal-organic frameworks (MOFs) for CO_2 capture at different pressures. Journal of Environmental Chemical Engineering. 2022; 10(6): 108930. doi: 10.1016/j.jece.2022.108930
64. Ouyang T, Cheng K, Gao Y, et al. Molten salt synthesis of nitrogen doped porous carbon: a new preparation methodology for high-volumetric capacitance electrode materials. Journal of Materials Chemistry A. 2016; 4(25): 9832-9843. doi: 10.1039/c6ta02673g
65. Wang Y, Wang J, Ma C, et al. Fabrication of hierarchical carbon nanosheet-based networks for physical and chemical adsorption of CO_2. Journal of Colloid and Interface Science. 2019; 534: 72-80. doi: 10.1016/j.jcis.2018.08.063
66. Volperts A, Plavniece A, Kaare K, et al. Influence of Chemical Activation Temperatures on Nitrogen-Doped Carbon Material Structure, Pore Size Distribution and Oxygen Reduction Reaction Activity. Catalysts. 2021; 11(12): 1460. doi: 10.3390/catal11121460

67. Wang S, Nam H, Nam H. Preparation of activated carbon from peanut shell with KOH activation and its application for H_2S adsorption in confined space. Journal of Environmental Chemical Engineering. 2020; 8(2): 103683. doi: 10.1016/j.jece.2020.103683
68. Khosrowshahi MS, Abdol MA, Mashhadimoslem H, et al. The role of surface chemistry on CO_2 adsorption in biomass-derived porous carbons by experimental results and molecular dynamics simulations. Scientific Reports. 2022; 12(1). doi: 10.1038/s41598-022-12596-5
69. Lin Z, Wang R, Tan S, et al. Nitrogen-doped hydrochar prepared by biomass and nitrogen-containing wastewater for dye adsorption: Effect of nitrogen source in wastewater on the adsorption performance of hydrochar. Journal of Environmental Management. 2023; 334: 117503. doi: 10.1016/j.jenvman.2023.117503
70. Teo EYL, Muniandy L, Ng EP, et al. High surface area activated carbon from rice husk as a high performance supercapacitor electrode. Electrochimica Acta. 2016; 192: 110-119. doi: 10.1016/j.electacta.2016.01.140
71. Shibuya R, Takeyasu K, Guo D, et al. Chemisorption of CO_2 on Nitrogen-Doped Graphitic Carbons. Langmuir. 2022; 38(47): 14430-14438. doi: 10.1021/acs.langmuir.2c01987
72. Kiuchi H, Shibuya R, Kondo T, et al. Lewis Basicity of Nitrogen-Doped Graphite Observed by CO_2 Chemisorption. Nanoscale Research Letters. 2016; 11(1). doi: 10.1186/s11671-016-1344-6
73. Ma X, Li L, Chen R, et al. Heteroatom-doped nanoporous carbon derived from MOF-5 for CO_2 capture. Applied Surface Science. 2018; 435: 494-502. doi: 10.1016/j.apsusc.2017.11.069
74. To JWF, He J, Mei J, et al. Hierarchical N-Doped Carbon as CO_2 Adsorbent with High CO_2 Selectivity from Rationally Designed Polypyrrole Precursor. Journal of the American Chemical Society. 2016; 138(3): 1001-1009. doi: 10.1021/jacs.5b11955
75. Liu Y, Wilcox J. Effects of Surface Heterogeneity on the Adsorption of CO_2 in Microporous Carbons. Environmental Science & Technology. 2012; 46(3): 1940-1947. doi: 10.1021/es204071g
76. Khosrowshahi MS, Abdol MA, Mashhadimoslem H, et al. The role of surface chemistry on CO_2 adsorption in biomass-derived porous carbons by experimental results and molecular dynamics simulations. Scientific Reports. 2022; 12(1). doi: 10.1038/s41598-022-12596-5
77. Ilnicka A, Skorupska M, Szkoda M, et al. Combined effect of nitrogen-doped functional groups and porosity of porous carbons on electrochemical performance of supercapacitors. Scientific Reports. 2021; 11(1). doi: 10.1038/s41598-021-97932-x
78. Kishore B, Shanmughasundaram D, Penki TR, et al. Coconut kernel-derived activated carbon as electrode material for electrical double-layer capacitors. Journal of Applied Electrochemistry. 2014; 44(8): 903-916. doi: 10.1007/s10800-014-0708-9
79. Xiao Y, Cai X, Sun W, et al. Nitrogen-enriched activated carbons via dual N-doping processes: Electrode material for high gravimetric- and volumetric-performance supercapacitor. Journal of Energy Storage. 2022; 56: 106040. doi: 10.1016/j.est.2022.106040
80. Seevakan K, Manikandan A, Devendran P, et al. Structural, magnetic and electrochemical characterizations of $Bi_2Mo_2O_9$ nanoparticle for supercapacitor application. Journal of Magnetism and Magnetic Materials. 2019; 486: 165254. doi: 10.1016/j.jmmm.2019.165254
81. Liu H, Song H, Chen X, et al. Effects of nitrogen- and oxygen-containing functional groups of activated carbon nanotubes on the electrochemical performance in supercapacitors. Journal of Power Sources. 2015; 285: 303-309. doi: 10.1016/j.jpowsour.2015.03.115
82. Huang X, Kim S, Heo MS, et al. Easy Synthesis of Hierarchical Carbon Spheres with Superior Capacitive Performance in Supercapacitors. Langmuir. 2013; 29(39): 12266-12274. doi: 10.1021/la4026969
83. Zhang S, Shi X, Wróbel R, et al. Low-cost nitrogen-doped activated carbon prepared by polyethylenimine (PEI) with a convenient method for supercapacitor application. Electrochimica Acta. 2019; 294: 183-191. doi: 10.1016/j.electacta.2018.10.111
84. Hulicova D, Yamashita J, Soneda Y, et al. Supercapacitors Prepared from Melamine-Based Carbon. Chemistry of Materials. 2005; 17(5): 1241-1247. doi: 10.1021/cm049337g
85. Hulicova-Jurcakova D, Fiset E, Lu GQM, et al. Changes in Surface Chemistry of Carbon Materials upon Electrochemical Measurements and their Effects on Capacitance in Acidic and Neutral Electrolytes. ChemSusChem. 2012; 5(11): 2188-2199. doi: 10.1002/cssc.201200376

86. Zdolšek N, Rocha RP, Krstić J, et al. Electrochemical investigation of ionic liquid-derived porous carbon materials for supercapacitors: pseudocapacitance versus electrical double layer. Electrochimica Acta. 2019; 298: 541-551. doi: 10.1016/j.electacta.2018.12.129
87. Su F, Poh CK, Chen JS, et al. Nitrogen-containing microporous carbon nanospheres with improved capacitive properties. Energy Environ Sci. 2011; 4(3): 717-724. doi: 10.1039/c0ee00277a
88. Ejaz A, Jeon S. The individual role of pyrrolic, pyridinic and graphitic nitrogen in the growth kinetics of Pd NPs on N-rGO followed by a comprehensive study on ORR. International Journal of Hydrogen Energy. 2018; 43(11): 5690-5702. doi: 10.1016/j.ijhydene.2017.12.184
89. Chen X, Paul R, Dai L. Carbon-based supercapacitors for efficient energy storage. National Science Review. 2017; 4(3): 453-489. doi: 10.1093/nsr/nwx009
90. Zhou M, Pu F, Wang Z, et al. Nitrogen-doped porous carbons through KOH activation with superior performance in supercapacitors. Carbon. 2014; 68: 185-194. doi: 10.1016/j.carbon.2013.10.079
91. Zhu D, Cheng K, Wang Y, et al. Nitrogen-doped porous carbons with nanofiber-like structure derived from poly (aniline-co-p-phenylenediamine) for supercapacitors. Electrochimica Acta. 2017; 224: 17-24. doi: 10.1016/j.electacta.2016.12.023
92. Zheng L, Tang B, Dai X, et al. High-yield synthesis of N-rich polymer-derived porous carbon with nanorod-like structure and ultrahigh N-doped content for high-performance supercapacitors. Chemical Engineering Journal. 2020; 399: 125671. doi: 10.1016/j.cej.2020.125671
93. Hao J, Wang X, Wang Y, et al. Hierarchical structure N, O-co-doped porous carbon/carbon nanotube composite derived from coal for supercapacitors and CO_2 capture. Nanoscale Advances. 2020; 2(2): 878-887. doi: 10.1039/c9na00761j
94. Kwiatkowski M, Hu X, Pastuszyński P. Analysis of the Influence of Activated Carbons' Production Conditions on the Porous Structure Formation on the Basis of Carbon Dioxide Adsorption Isotherms. Materials. 2022; 15(22): 7939. doi: 10.3390/ma15227939
95. Chen LF, Zhang XD, Liang HW, et al. Synthesis of Nitrogen-Doped Porous Carbon Nanofibers as an Efficient Electrode Material for Supercapacitors. ACS Nano. 2012; 6(8): 7092-7102. doi: 10.1021/nn302147s
96. Lin X, Yin S, Zhang W, et al. N/P/O doped porous carbon materials for supercapacitor with high performance. Diamond and Related Materials. 2022; 125: 109025. doi: 10.1016/j.diamond.2022.109025
97. Han X, Jiang H, Zhou Y, et al. A high performance nitrogen-doped porous activated carbon for supercapacitor derived from pueraria. Journal of Alloys and Compounds. 2018; 744: 544-551. doi: 10.1016/j.jallcom.2018.02.078
98. Zhong Z, Mahmoodi S, Li D, et al. Electrochemical Performance and Conductivity of N-Doped Carbon Nanotubes Annealed under Various Temperatures as Cathode for Lithium-Ion Batteries. Metals. 2022; 12(12): 2166. doi: 10.3390/met12122166
99. Zou K, Deng Y, Chen J, et al. Hierarchically porous nitrogen-doped carbon derived from the activation of agriculture waste by potassium hydroxide and urea for high-performance supercapacitors. Journal of Power Sources. 2018; 378: 579-588. doi: 10.1016/j.jpowsour.2017.12.081
100. Olejniczak A, Leżańska M, Pacuła A, et al. Nitrogen-containing mesoporous carbons with high capacitive properties derived from a gelatin biomolecule. Carbon. 2015; 91: 200-214. doi: 10.1016/j.carbon.2015.04.025
101. Lee YH, Chang KH, Hu CC. Differentiate the pseudocapacitance and double-layer capacitance contributions for nitrogen-doped reduced graphene oxide in acidic and alkaline electrolytes. Journal of Power Sources. 2013; 227: 300-308. doi: 10.1016/j.jpowsour.2012.11.026
102. Li Z, Zhang L, Amirkhiz BS, et al. Carbonized Chicken Eggshell Membranes with 3D Architectures as High-Performance Electrode Materials for Supercapacitors (Adv. Energy Mater. 4/2012). Advanced Energy Materials. 2012; 2(4): 430-430. doi: 10.1002/aenm.201290018
103. Yan Y, Kuila T, Kim NH, et al. N-doped carbon layer coated thermally exfoliated graphene and its capacitive behavior in redox active electrolyte. Carbon. 2015; 85: 60-71. doi: 10.1016/j.carbon.2014.12.069
104. Pan Q, Ding Y, Yan Z, et al. Designed synthesis of Fe3O4@NC yolk-shell hollow spheres as high performance anode material for lithium-ion batteries. Journal of Alloys and Compounds. 2020; 821: 153569. doi: 10.1016/j.jallcom.2019.153569
105. Wang J, Hu Q, Hu W, et al. Preparation of Hollow Core–Shell Fe3O4/Nitrogen-Doped Carbon Nanocomposites for Lithium-Ion Batteries. Molecules. 2022; 27(2): 396. doi: 10.3390/molecules27020396
106. Guo X, Ding Y, Xue L, et al. A Self-Healing Room-Temperature Liquid-Metal Anode for Alkali-Ion Batteries. Advanced Functional Materials. 2018; 28(46). doi: 10.1002/adfm.201804649

107. Liu J, Zhao H, Zhu F, et al. Nitrogen-doped Porous Carbon Obtained from Silk Cocoon for High Performance Li-O2 Batteries. ChemistrySelect. 2019; 4(25): 7602-7608. doi: 10.1002/slct.201901524
108. Xu F, Ding B, Qiu Y, et al. Hollow Carbon Nanospheres with Developed Porous Structure and Retained N Doping for Facilitated Electrochemical Energy Storage. Langmuir. 2019; 35(40): 12889-12897. doi: 10.1021/acs.langmuir.8b03973
109. Shaker M, Ghazvini AAS, Shahalizade T, et al., A review of nitrogen-doped carbon materials for lithium-ion battery anodes. New Carbon Materials. 2023; 38(2): 247-282. doi: 10.1016/S1872-5805(23)60724-3
110. Zhang W, Wu J, Li Y, et al. High stability and high performance nitrogen doped carbon containers for lithium-ion batteries. Journal of Colloid and Interface Science. 2022; 625: 692-699. doi: 10.1016/j.jcis.2022.06.062

EnPress Publisher, LLC

Add: 9650 Telstar Avenue, Unit A, Suite 121, El Monte, CA 91731, USA.
Email: contact@enpress-publisher.com
Web: https://systems.enpress-publisher.com